Master thesis : Thermal design of the OUFTI-Next mission

Auteur : Kellens, Anthony
Promoteur(s) : Kerschen, Gaetan
Faculté : Faculté des Sciences appliquées
Diplôme : Master en ingénieur civil en aérospatiale, à finalité spécialisée en "aerospace engineering"
Année académique : 2017-2018
URI/URL : http://hdl.handle.net/2268.2/5480

University of Liège

Faculty of Applied Sciences

Centre Spatial de Liège

Thermal Design of the OUFTI-Next mission

Graduation Studies conducted for obtaining the Master's degree in Aerospace Engineering
by Anthony Kellens

Academic advisor Prof. Gaëtan Kerschen

Co-advisor Prof. Jerôme Loicq

Academic year 2017-2018

Abstract

OUFTI-Next is a CubeSat developed by the University of Liège aiming to improve irrigation strategies. Thermal infrared imaging is used to measure the temperature of crops and to assess their level of hydric stress. OUFTI-Next is a technology demonstrator for an ambitious project. The final objective is to launch a constellation of satellites to achieve daily revisits over a particular location.

This Master's Thesis focuses on the thermal modelling and design of the satellite. Because of the early phase of the mission, several spacecraft's shapes and orbits have been considered throughout this study. The goal was to determine the feasibility form the thermal point of view and to guarantee that all the components operate within their allowed thermal range. Various models of increasing complexity have been implemented to analyze the thermal behaviour of the satellite. The computation has mainly been done with the ESATAN software and the results have been heavily post-processed by MATLAB routines.

The thermal models highlighted the fact that some components were not compliant with their permitted temperature range. To solve this problem, several solutions have been implemented. Special care has also been taken to maintain the payload as cold as possible. Indeed, this critical element requires low temperatures to operate properly.

Because the mission was only at its beginning, the different thermal properties have not been fixed yet. Hence their influence on the results has been determined and discussed at several stages of the work thanks to sensitivity and uncertainty analyses.

Keywords: OUFTI-Next, CubeSat, Thermal design, ESATAN

Acknowledgements

First of all, I sincerely thank Lionel Jacques for all his advises and feedback during the project as well as for taking the time to answer my numerous questions. I also thank him for sharing his knowledge about thermal design and the lessons learned from OUFTI-1.

I wish to express my gratitude to my advisor, Prof. Gaëtan Kerschen as well as to Prof. Jerôme Loicq, Prof. Serge Habraken and Xavier Werner for their feedback and suggestions during the different meetings. I also thank all the people working at Centre Spatial de Liège for welcoming me during my internship.

I am also grateful to the other students, Anna, Lidiia, Colin, Pierre, Donatien and Victor working on the OUFTI-Next project.

Last but not least, I wish to thank my family for encouraging me during this thesis and supporting me during my studies.

Contents

List of Figures

List of Tables

Acronyms

ADCS	Attitude Determination and Control Subsystem
BOL	Beginning Of Life
CCD	Charged Coupled Device
CNES	Centre National d'Etudes Spatiales
COOL	Subsystem of the OUFTI-Next mission dedicated to the study of the detector's cooling, conducted by Pierre Remacle
ECSS	European Cooperation for Space Standardization
EOL	Endo Of Life
EPS	Electrical Power Supply
ESA	European Space Agency
FEM	Finite Element Method
GMM	Geometric Mathematical Model
GPS	Global Positioning System
GSD	Groud Sampling Distance
IR	Infrared
ISS	International Space Station
LEO	Low Earth Orbit
LTAN	Local Time of Ascending Node
MCRT	Monte Carlo Ray Tracing
MLI	Multi Layer Insulation
MWIR	Mid-Wavelength Infrared
NASA	National Aeronautic and Space Administration
OBC	On Board Computer
OFL	Subsystem of the OUFTI-Next mission dedicated to the optical Fresnel lens design, conducted by Lidiia Suleimanova
ORL	Subsystem of the OUFTI-Next mission dedicated to the optical reflective design, conducted by Donatien Calozet
ORR	Subsystem of the OUFTI-Next mission dedicated to the optical refractive design, conducted by Anna Riera Salvà
OUFTI	Orbital Utility For Thermal Imaging
P-POD	Poly Picosatellite Orbital Deployer
PCB	Printed Circuit Board
RAAN	Right Ascension of Ascending Node
REF	Radiative Exchange Factor
SSO	Sun Synchronous Orbit
SYSE	Subsystem of the OUFTI-Next mission dedicated to system engineering part, conducted by Colin Dandumont
TMM	Thermal Mathematical Model
UHF	Ultra High Frequency

UV Ultraviolet
VHF Very High Frequency

Introduction

This Master's Thesis is dedicated to the thermal study of the OUFTI-Next (Orbital Utility For Thermal Imaging) CubeSat, developed at the University of Liège. The main objective of this work is to model the satellite and to develop solutions to ensure that all its elements stay in their allowable temperature range.

The first chapter presents the scientific mission of the spacecraft. It introduces essential subjects related to the satellite like the orbit and the components constituting OUFTI-Next, as well as their thermal requirements. It also exposes the three satellite's shapes that are studied throughout this document.

Next, the basic principles of heat transfer in space are reminded and the three environmental loads (solar, albedo and Earth IR fluxes) acting on the spacecraft are described. Then, the means to mitigate their impact are discussed. Finally, the strategies adopted by thermal designers of other CubeSat missions are presented through a state of the art.

The third chapter focuses on the modelling of the orbital environmental fluxes. Analytic tools are developed in MATLAB and the results are compared to the standard European space thermal analysis software, ESATAN. Next, the first temperature computation is made on a simple 1-node model. It allows to illustrate the benefits of cyclic transient calculations over static computations.

Then, basic models of the three spacecraft's shapes are developed. As they are composed of a few nodes only, their purpose is to extract qualitative information like the influence of the orbit or the effect of the satellite's shape on the temperatures. These computations require the introduction of concepts related to thermal analysis like the worst thermal case approach, the geometric mathematical model (GMM) and the thermal mathematical model (TMM).

The core of this thesis starts with Chapter 5, where a detailed model of the satellite is presented. Each element composing the spacecraft is associated to a node. It allows the determination of their individual temperature. The modelling procedure is divided in two steps. The first one is dedicated to the GMM, where the thermo-optical surface properties are looked at. Then, the radiative exchange factors are computed. The second one (TMM) focuses on the conductive network, the bulk properties (material composition of the components and capacitance) and the electrical dissipation.

The next chapter exposes the results of the detailed models. The discussion mainly focuses on the *Body Mounted* spacecraft's shape as this one will most probably be selected for OUFTI-Next. Then, the effect of changing the attitude of the satellite for the imaging and communication phases is examined. Because of the early stage of the mission, the input parameters (thermo-optical properties, capacitances, ...) are subject to various assumptions. To asses their effect on the temperature results, an uncertainty analysis is conducted. The last part of the chapter is dedicated to the thermal design. Based on the results previously obtained, the initial model is modified to ensure that the components stay in their permitted temperature range.

Finally, a conclusion completes this thesis by summarizing the main results and proposing future developments.

1 | Mission description

The first chapter is dedicated to the presentation of OUFTI-Next. After briefly explaining the scientific goal of the mission, the different spacecraft's configurations are defined. They mainly differ from each other by the amount of solar cells and by their arrangement. Then, the components forming the satellite as well as their thermal requirements will be presented. Finally, the orbits chosen to conduct the thermal analysis and the spacecraft's attitude will be exposed.

1.1 The scientific goal

Around the globe, one quarter of farmlands are irrigated, producing one third of the food. It has been estimated that irrigated fields are 3.5 times more efficient than non-irrigated ones. Watering is thus essential to obtain high yields in arid areas. On a planet scale, 70% of the freshwater is used by agriculture and experts say that the irrigation efficiency does not exceed 40%, meaning that 28% of this valuable resource is wasted. The objective of OUFTI-Next is to improve irrigation strategies.

The mission's goal is to detect hydric stress in plants to determine their need in water. When crops suffer from a water shortage, they close their stomas, which are small pores at the leaf's surface responsible for transpiration. This leads to a temperature increase. Hence, the plants' stress level is determined by measuring the temperature difference between the ground and the leaves, which can be as large as 10°C. This task is achieved by mid-wavelength infrared (MWIR) measurements (3-5 μm).

To be effective in detecting the lack of water, a ground sampling distance (GSD) of 50 m is necessary, as well as a high revisit rate. In fact, farmers would need at least one picture of their fields per day to implement good irrigation strategies. As a low altitude orbit is needed for the GSD, a constellation is required to achieve the desired revisit rate. It has been established by D. Schklar in [1] that at least 8 satellites are necessary.

Before launching a complete constellation, a technology demonstrator is required to ensure the good implementation of the MWIR detector and the scientific usability of the measures taken. It is the purpose of the OUFTI-Next 3U CubeSat. Because of the smaller platform size of the demonstrator, the spatial resolution is doubled (100 m).

1.2 OUFTI-Next's configurations

The OUFTI-Next demonstrator is a 3U CubeSat ($10 \times 10 \times 34$ cm, see Appendix A) with 1.5U dedicated to the payload composed of the optics, the detector and its cooling system. Because of the early stage of the mission, the shape of the satellite is not fixed and several configurations are studied.

The first configuration to be considered is the standard 3U shape (Fig. 1.1a and Fig. 1.2). Solar panels are placed on faces $+X$, $+Y$ and $+Z$, covering them entirely. This configuration

will be referred to as *Body Mounted* in the rest of this work.

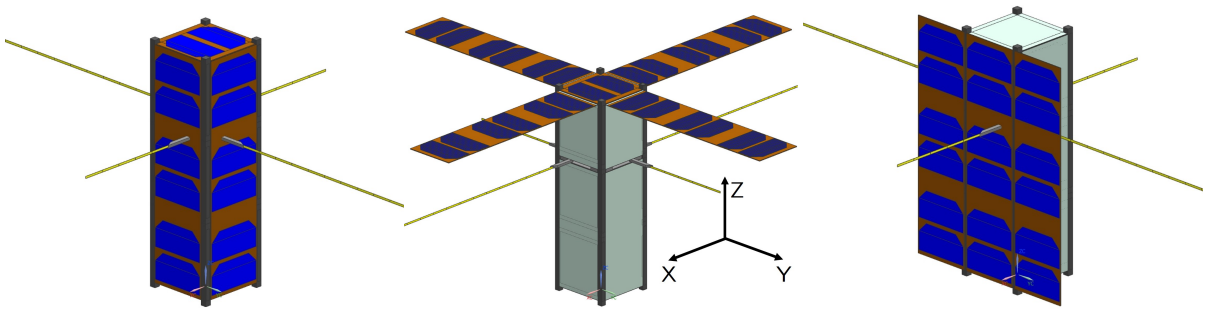

(a) Body Mounted (b) Cross (c) Table

Fig. 1.1: OUFTI-Next's configurations.

It has been established in [2] by the System Engineering (SYSE) subsystem that a classical *Body Mounted* configuration might not produce enough power depending on the cooling strategy adopted for the detector. In this case, deployable solar panels are needed. In particular, the project team has decided to investigate two deployable configurations. The first one consists in four 3U solar panels attached to the top of the spacecraft, in $+Z$. The 10×10 cm face is also covered by solar cells to maximize the power generation. This option is presented in Fig. 1.1b and Fig. 1.3 and is referred as the *Cross* configuration.

The second option consists in using only two 3U deployable solar panels. This time, they are attached to the large face in $+X$, which is also covered by solar cells. This configuration, called *Table*, is depicted in Fig. 1.1c and Fig. 1.4 and has a total of 18 cells. In all cases the payload fills the bottom side of the spacecraft and the aperture is located on the $-Z$ face.

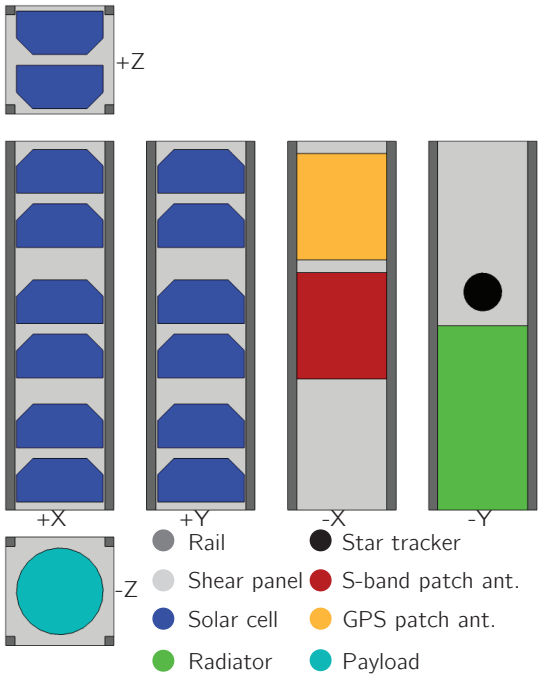

Fig. 1.2: Surface layout for the *Body Mounted* configuration.

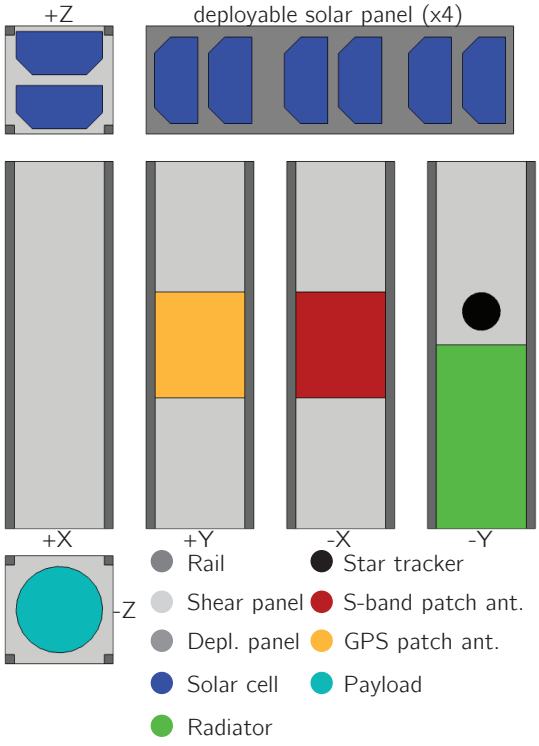

Fig. 1.3: Surface layout for the *Cross* configuration.

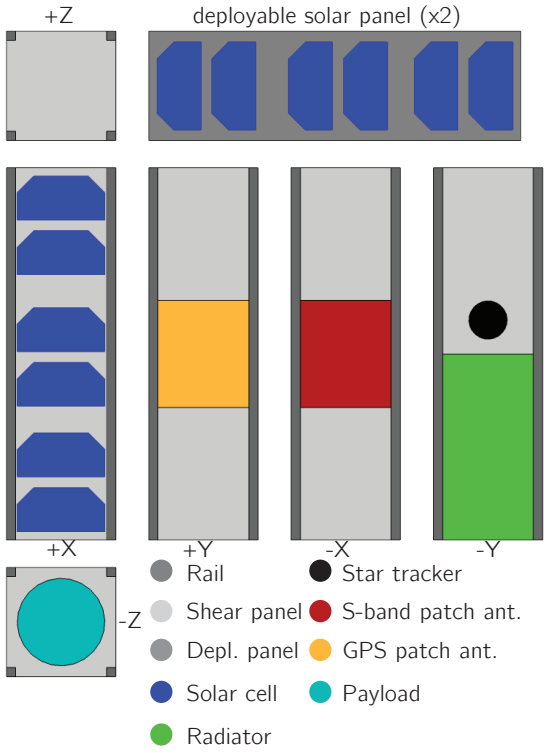

Fig. 1.4: Surface layout for the *Table* configuration.

1.3 Satellite's components and thermal requirements

This section presents the different components of OUFTI-Next. They have been selected in cooperation with the SYSE subsystem. However, because of the early stage of the mission, they will be used as reference parts to give an idea of their properties (mass, volume, thermal requirements, ...). The choice is also guided by the amount of information provided by the manufacturer.

Exterior

As stated previously, three configurations are considered for the satellite and two of them need 3U deployable solar panels. ISIS provides such modules (see [3]). However, they lack information concerning the material supporting the cells and the PCB thickness. These data are thus extrapolated from another deployable panel mechanism presented by EXA ([4]). Detailed information about the solar cells themselves are taken from Spectrolab datasheet [5] where *Ultra Triple Junction* cells with 28% efficiency are used.

The selected structure, coming from ISIS [6], is highly modular, allows an easy implementation of the PCB stack and an easy access to the spacecraft's components during the assembly phase. It also comes with aluminum shear panels covering the faces. A 3D model is presented in Fig. 1.5, where the green parts correspond to the ribs and the blue ones to the frames (composed of four rails).

OUFTI-Next has two patch antennas. The first one is a GPS antenna from SkyFox Labs [7] and the other one is dedicated to communication via S-band [8]. They are both presented in Fig. 1.6. Unfortunately, the Clyde Space S-band antenna lacks technical information. For the thermal analysis, it will thus be considered that it has the same properties as the GPS antenna.

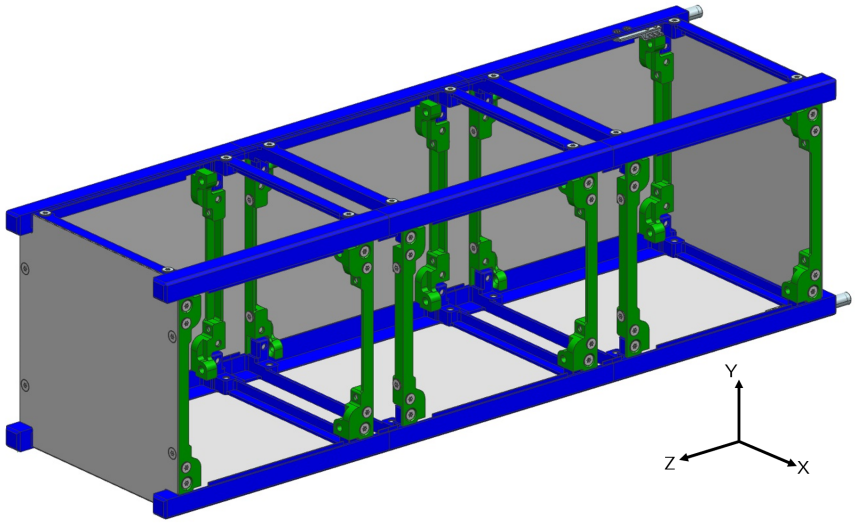

Fig. 1.5: ISIS 3U structure.

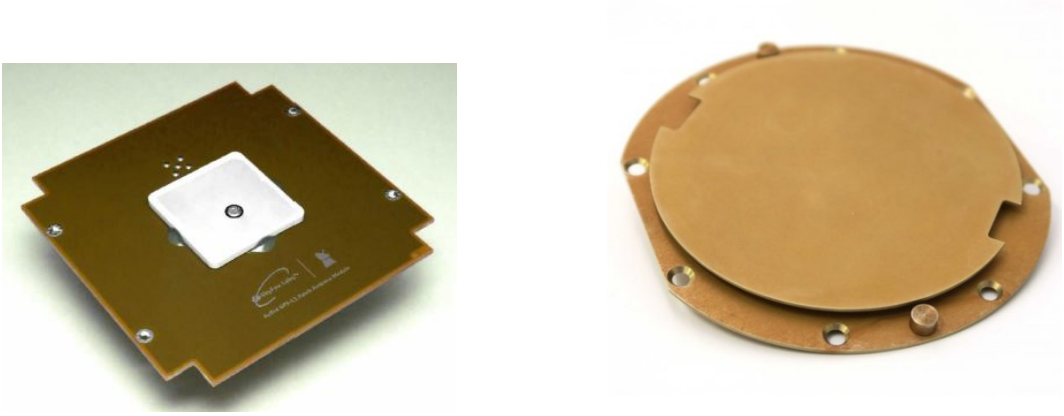

(a) GPS patch antenna from SkyFox Labs [7]. (b) S-band patch antenna from Clyde Space [8].

Fig. 1.6: OUFTI-Next's patch antennas.

Interior

The interior of the spacecraft is presented in Fig. 1.7. The top unit is occupied by the PCB stack, which is composed of all the circuit boards needed for the satellite's bus.

The upper most layer corresponds to the power subsystem. It has been decided to use an EPS-battery bundle from Clyde Space [9] (see Fig. 1.8). This system has the advantage of being more compact than a classical one where the two components are separated. Moreover, the battery integrates heaters to prevent too low temperatures. However, this feature will not be taken into account for the thermal analysis because this specific battery model might be replaced by another one in the final satellite. The battery cells are based on a lithium polymer technology, which has superior discharge characteristics compared to classical lithium ion cells. Unfortunately, Clyde Space does not provide thermal data for the batteries (heat capacity, conductivity, operating thermal range). These information are thus taken from lithium ion space qualified batteries proposed by GOMSpace [10].

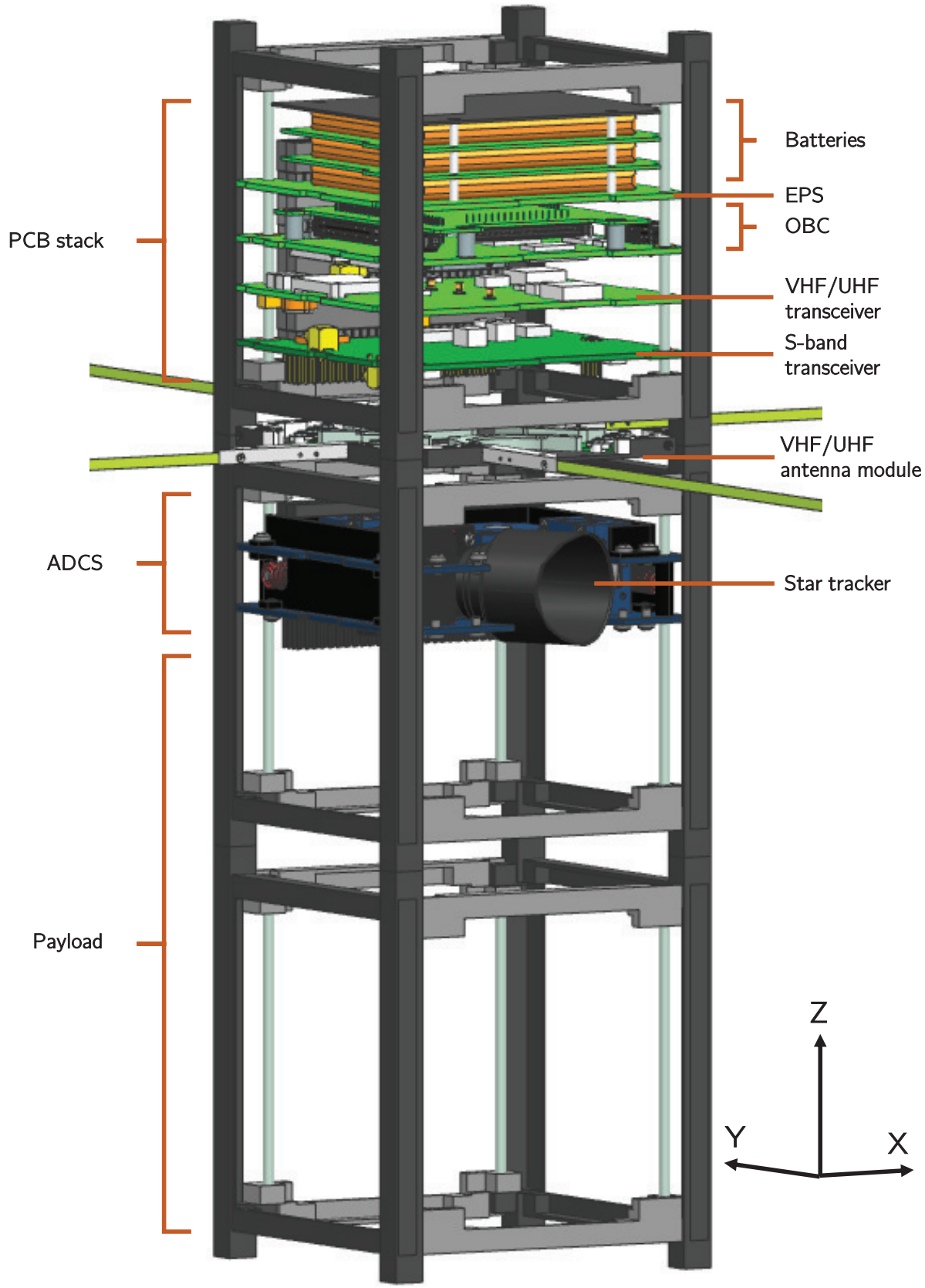

Fig. 1.7: OUFTI-Next's interior.

The next PCB in the stack is the on-board computer (OBC). This component, from ISIS, is represented in Fig. 1.9. The company provides it with an optional daughter board. The need for this component has not yet been studied but it will be taken into account as an additional mass in the OBC board. The last two circuit boards, the transceivers for the S-band and VHF/UHF antennas [11] [12], are also supplied by ISIS.

Fig. 1.8: EPS-battery bundle from Clyde Space [9].

Fig. 1.9: OBC and its daughter board from ISIS [13].

The VHF/UHF dipole antenna module (see Fig. 1.10) [14] is placed under the PCB stack. The four antennas will not be modeled in the thermal analysis because they have a negligible mass and a small surface extension. It is thus assumed that they have a marginal impact on the thermal behaviour of the spacecraft. However, the circuit board containing the deployment mechanism and the electronics is considered.

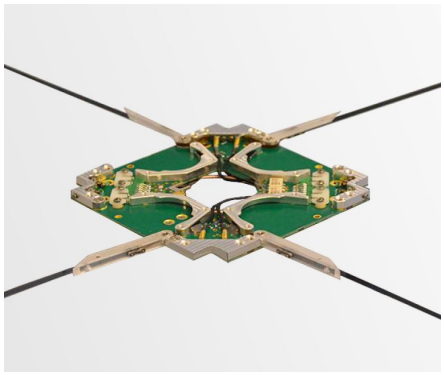

Fig. 1.10: VHF/UHF dipole antenna module from ISIS [14].

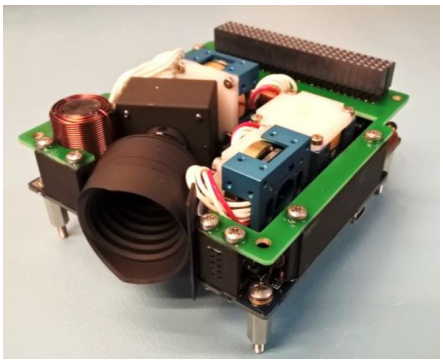

Fig. 1.11: ADCS from Hyperion Technologies [15].

The last component of the satellite's platform is the ADCS module [15]. This element, from Hyperion Technologies, is composed of three orthogonal reaction wheels and a star tracker.

The bottom 1.5U of the spacecraft is dedicated to the payload. This part is the most undefined one since it is currently studied by other team members. The different choices which are considered are a refractive optical system ORR [16], a reflective assembly ORL [17] and a system using Fresnel lenses OFL [18]. The payload is also composed of the MWIR detector and its cooling system studied by COOL in [19].

Finally, the thermal requirements of the different elements of OUFTI-Next are listed in Tab. 1.1. It can be seen that the batteries have the narrowest operational temperature range, especially if they are charging. The payload does not appear in the table because it does not have an explicit thermal range. However, one could say that the requirement is to maintain it *as cool as possible* using passive techniques. By doing so, the work of the COOL subsystem (detector cooling) will be greatly facilitated.

Component	**Thermal range [°C]**	**Source**
Structure	-40 to 80	[6]
Shear panels	-40 to 80	[6]
Solar cells	-55 to 125	[20] [21]
Batteries (charge)	0 to 45	[10]
Batteries (discharge)	-20 to 60	
EPS PCB	-20 to 60	[22] [23]
OBC PCB	-25 to 65	[13]
VHF/UHF transceiver PCB	-20 to 60	[12]
S-band transceiver PCB	-40 to 60	[11]
ADCS	-45 to 85	[15]
GPS patch antenna	-40 to 45	[7]
S-band patch antenna	-25 to 45	[8]
VHF/UHF antenna module[1]	-20 to 60	[14]

Table 1.1: Thermal requirements.

1.4 Orbits

The orbit choice results from a trade-off between the scientific requirements, the availability and the cost. Ideally, an orbit should fulfill perfectly the requirements of the mission regarding the altitude (to achieve a good ground sampling distance) and the illumination condition on ground in order to obtain scientifically exploitable data from the measurements. Nevertheless, due to the financial limitation for the project, a dedicated launch is not possible. The satellite will have to be launched as a piggyback of a bigger mission, and it will therefore be dependant on the orbit and launch schedule of the primary satellite. Another option is to deploy it directly from the International Space Station (ISS) or from its cargo vessel, Cygnus. These two spacecraft have very close orbits. Hence, it is chosen to use the ISS for the thermal study.

An interesting orbit is the Sun synchronous orbit (SSO). This one makes a constant angle with the Sun rays all over the year. From the scientific mission point of view, it ensures that the pictures of a given crop field, taken several days apart, have the same illumination conditions. It has been established that most appropriate time range to take these IR images is between 12h and 14h. This two hours-range corresponds to the peak of plants' transpiration and will allow a better contrast between well irrigated fields and dry ones. For these reasons, the team has selected a 13h30 local time of ascending node (LTAN) for the orbit. An additional constraint comes from the revisit period which must be as short as possible. This topic is covered in details by the SYSE subsystem in [2].

The last parameter needed to fix the SSO is the altitude. Its value is a compromise between the spacecraft's lifetime and the desired GSD. A low altitude provides a better ground resolution

[1]The thermal range specified here is only valid for the antenna's module (i.e. the circuit board) an not the antennas them selves (i.e. the four thin metal strips).

but suffers from an increased drag due to the atmosphere, reducing the lifetime of the satellite. On the other hand, if the altitude is higher, the satellite will stay longer in orbit but it will be more difficult to obtain a good resolution. The project team members studying the optical subsystems (ORR, OFL and ORL) have shown that the threshold for a good resolution is 650 km. However, I decided to conduct the thermal study by considering two different altitudes: 400 km and 800 km. This ensures to cover any potential changes coming from the optical designers. Nevertheless, it can be seen in Fig. 1.12 that the temperature results obtained for the 650 km SSO are very close to those of the 800 km altitude. The process leading to these curves will be deeply explained in the rest of this work. It is important to stress that the 800 km altitude is only used for thermal computation purposes. Its role is only to provide an upper bound on the altitude for the thermal analysis. Therefore, this altitude must not be seen as a possible orbit choice for OUFTI-Next. Indeed, this altitude induces a mission lifetime larger than the 25 years allowed by the ESA guidelines [24][1].

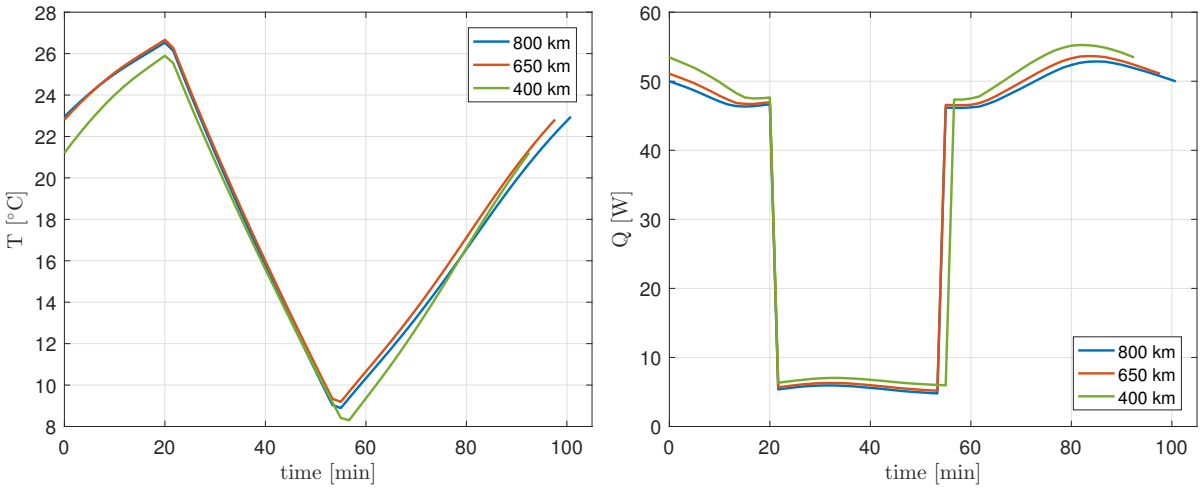

(a) Temperature

(b) Total absorbed power

Fig. 1.12: Influence of the SSO altitude on thermal results.
Body Mounted configuration, 1 node model, cold case.

Finally, the three orbits selected for the thermal study are summarized in Tab. 1.2.

Parameter	ISS	800 km SSO 13h30	400 km SSO 13h30
altitude of perigee [km]	400.6	800	400
altitude of apogee [km]	416.9	800	400
inclination [°]	51.71	98.58	97.01
RAAN [°]	167.35	13h30 LTAN	13h30 LTAN
orbital period [min]	92.66	100.79	92.48

Table 1.2: Orbits considered for the thermal study.

1.5 Satellite's attitude

The attitude of the satellite depends on the task to be performed. Three modes are considered. The first one is the *imaging/acquisition mode*. It corresponds to the acquisition of scientific data

[1]For more details on OUFTI-Next's lifetime, see Table 2.1.4 of [2].

by the detector. In this case, the small face located in $-Z$ (in the satellite's axes) points nadir. This situation lasts approximately 5 minutes.

Once the IR pictures have been taken, it is necessary to download them to the ground station. It is done by the S-band patch antenna during the *transfer/communication mode*. This situation lasts about 7 minutes and needs the antenna to face the Earth.

The last one is the *idle mode*, during which the satellite points to the Sun to charge its batteries. In this orientation, the spacecraft can also communicate with the ground station thanks to the VHF and UHF antennas. It is also the default mode, when the satellite is neither imaging nor communicating via S-band. It corresponds to 90% to 95% of the orbital period.

Since the purpose of the Sun pointing mode is to charge the batteries, the spacecraft's attitude has to maximize the power produced by the solar cells. For the *Cross* and *Table* configurations, it is simply obtained by giving the satellite an orientation where the Sun rays are perpendicular to the solar panels. For the *Body Mounted* configuration, the situation is more complex because the solar cells are not all on the same plane. Since the panels located on faces $+X$ and $+Y$ have the same size, the optimal orientation will be achieved if the azimuth angle θ (from the x axis and positive towards y axis, see Fig. 1.13) is 45°. The maximum power generation is thus achieved with an elevation angle γ (from the xy plane and positive towards z axis) maximizing the following equation developed in Appendix B:

$$Q = 2A_{3U}C_S\eta\cos\Omega + A_{1U}C_S\eta\sin\gamma\,, \qquad \text{with } \cos\Omega = \sqrt{\frac{1-\sin^2\gamma}{2}}\,.$$

In this relation, C_S is the solar constant, η is the solar cells' efficiency, A_{3U} and A_{1U} are respectively the surface area covered by the solar cells for a 3U and a 1U face. Ω is the angle between the normal of the 3U face and the Sun rays.

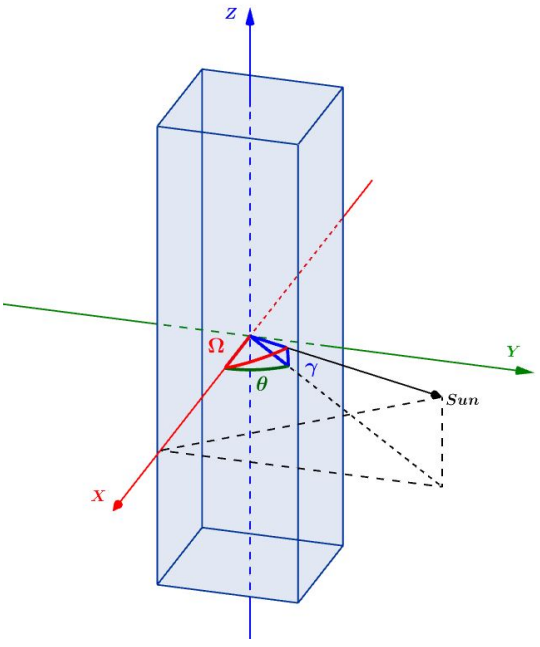

Fig. 1.13: Optimal sun pointing of the *Body Mounted* configuration.
Faces $+X$, $+Y$ and $+Z$ are covered by solar cells.

Finally, the elevation angle γ maximizing the power production is $\gamma = \arctan\left(\sqrt{2}/6\right)$. It corresponds to the case where the Sun is located in the direction [1, 1, 1/3], in the satellite's axes presented in Fig. 1.13.

2 | Thermal control subsystem

This chapter presents the thermal control subsystem of satellites from a theoretical point of view. First, the equations governing heat transfer are reminded. Next, the thermal loads due to the environment acting on the spacecraft are presented as well as means to mitigate their impact. Finally, the thermal control strategies of some CubeSats are discussed.

2.1 Heat transfer in space

Heat can be exchanged between bodies by four different ways: radiation, conduction, convection and ablation. Each of them is briefly described here below.

2.1.1 Radiation

Radiation is the only heat transfer mechanism that does not require a medium to operate. To explain this process, the concept of *blackbody* must be introduced. A blackbody is a perfect diffuse emitter and absorber. It can absorb all the incident radiation, regardless of the wavelength and direction. Moreover, for a given temperature and wavelength, no surface can emit more energy. The blackbody is thus an ideal entity against which the radiative properties of real bodies can be compared [25].

The emissive power of a blackbody follows the Stefan-Boltzmann's law written hereafter and expresses the fourth power dependence with the temperature.

$$E_{bb}(T) = \int_0^\infty E_{bb}(\lambda, T) d\lambda = \sigma T^4$$

In this relation, σ is the Stefan-Boltzmann's constant ($\sigma = 5.67 \cdot 10^{-8}$ W/m^{2}K^4) and E_{bb} is the hemispherical spectral emissive power which follows the Planck's law:

$$E_{bb}(\lambda, T) = \frac{2hc^2}{\lambda^5} \frac{1}{e^{hc/(\lambda k_B T)} - 1},$$

with h, c and k_B, the Planck's constant ($6.63 \cdot 10^{-34}$ Js), the speed of light in vacuum (299 792 458 m/s) and the Boltzmann's constant ($1.38 \cdot 10^{-23}$ m^{2}kg s^{-2}K^{-1}) respectively. The Planck's law describes the way a body emits radiation at a non zero temperature. It can be seen in Fig. 2.1 that radiation is emitted on a broad range of wavelengths and that the maximum intensity depends on the temperature. This maximum wavelength (in μm) obeys the Wien's displacement law:

$$\lambda_{max} = \frac{2897}{T}.$$

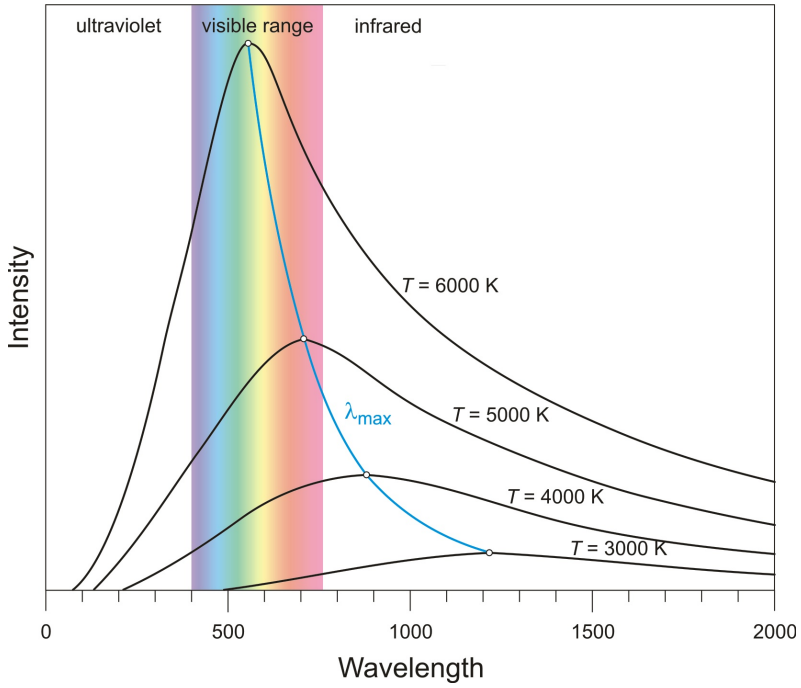

Fig. 2.1: Planck and Wien laws for blackbody radiation.
SOURCE: `https://glossary.periodni.com`

The emissivity (ϵ) corresponds to the ratio of the energy emitted by a real surface to the energy emitted by a blackbody and is thus always lower than one. This surface property is linked to the absorptivity (α) by the Kirchhoff's law of thermal radiation:

$$\epsilon_{\lambda,\theta} = \alpha_{\lambda,\theta} \, .$$

This equality is true for spectral and directional properties. But for thermal modeling ease, it has been assumed by space thermal engineers that the emissivity and absorptivity are constant in two distinct wavelength domains:

- Visible (0.3 μm to 0.7 μm): $\alpha \coloneqq \alpha_{vis} = \epsilon_{vis}$,
- Infrared (0.7 μm to 5 μm): $\epsilon \coloneqq \alpha_{IR} = \epsilon_{IR}$.

It means that for the rest of this document, the word *emissivity* will refer to the infrared emissivities and absorptivities ($\alpha_{IR} = \epsilon_{IR}$), while *absorptivity* will designate the visible (or solar) emissivities and absorptivities ($\alpha_{vis} = \epsilon_{vis}$). This is called the *semi-gray* assumption.

Since radiation exchange is a surface phenomenon, a way to know if two surfaces see each other is needed. This is accomplished with the view factor $F_{i,j}$ between surfaces A_i and A_j. It represents the proportion of diffuse radiation leaving A_i that reaches A_j directly, without any intermediate reflection. It depends only on geometric parameters and is given by:

$$F_{i,j} = \frac{1}{A_i} \int_{A_i} \int_{A_j} \frac{\cos\theta_i \cos\theta_j}{\pi R^2} dA_i dA_j$$

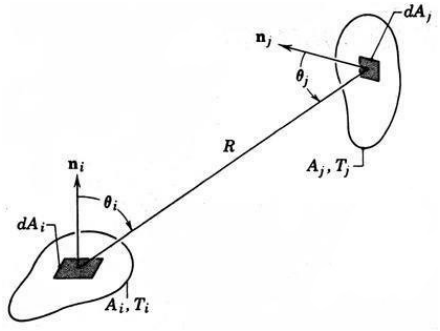

Fig. 2.2: View factor between two surfaces.
SOURCE: `https://www.physicsforums.com/`

This integral is often difficult to evaluate and a ray tracing software is preferred when complex geometries are involved. Nevertheless, view factors follow two easy algebraic rules: *closure* and *reciprocity*. The first one states that the sum of all the view factors leaving a surface is 1 ($\sum_j F_{i,j} = 1$). The other one is simply $A_i F_{i,j} = A_j F_{j,i}$.

On the other hand, Gebhart factors [25] account for the surface properties and allows several reflections of the rays before reaching the target. They are computed by the iterative formula:

$$B_{i,j} = F_{i,j}\epsilon_j + \sum_k F_{i,k}(1-\epsilon_k)B_{k,j} \,.$$

Once again this expression is complicated to evaluate analytically and ray tracing is used for practical applications.

Finally, the radiative power $Q_{i,j}$ going from A_i to A_j is given by:

$$Q_{i,j} = \sigma G R_{i,j} \left(T_i^4 - T_j^4\right) \,,$$

where $GR_{i,j}$ is the radiative exchange factor between the two surfaces such that

$$GR_{i,j} = \epsilon_i A_i B_{i,j} \,.$$

2.1.2 Conduction

Unlike radiation, heat transfer by conduction needs a medium to happen. It is a volume-dependant phenomenon principally linked to solids[1]. This heat exchange phenomenon is involved in spacecraft when thermal power is transferred between the satellite's different elements.

The conductive thermal power flowing between two isothermal surfaces at temperatures T_i and T_j is computed thanks to the simplified 1D version of the Fourier's law:

$$Q_{i,j} = k\frac{A}{L}\left(T_i - T_j\right) = GL_{i,j}\left(T_i - T_j\right) \,,$$

where k is the thermal conductivity of the material (in W/mK), A is the cross section of the heat path, L is its length and GL is the thermal conductance.

A convenient way to represent a thermal network is the electrical analogy. The association rules of electric circuits are thus transposed to thermal resistances and conductances. The most commonly used rules are the *series* and *parallel* associations:

[1] Conduction can also occur in fluids at rest but is less effective than in solids because the atoms and molecules are less compact.

- Series: $\frac{1}{GL_{tot}} = R_{tot} = \sum_i \frac{1}{GL_i}$,
- Parallel: $GL_{tot} = \frac{1}{R_{tot}} = \sum_i GL_i$.

2.1.3 Convection and ablation

Convection is a process occurring when heat is transferred inside a moving fluid or between a moving fluid and a solid. It results from the combination of two elementary mechanisms: *diffusion* (random motion of the fluid's molecules) and *advection* (bulk macroscopic motion of the fluid). This heat transfer mode is encountered in space for manned mission or in cooling fluid loops but it will be ignored in this work since it is not applicable to OUFTI-Next.

On the other hand ablation is a sacrificial method of heat protection. This process combines radiation, convection and chemical reactions. It is based on the destruction of a solid material which stays in the surroundings of the thermal shield and serves as a protective layer. This mechanism is used to protect capsules and the Space Shuttle from the extreme heat (more than 1200°C at the nose of the Shuttle) during atmosphere reentry. As for convection, this mechanism is not relevant here.

2.2 Thermal environment

A spacecraft orbiting a planet is subjected to several heat loads coming from the environment. Those are pictured in Fig. 2.3.

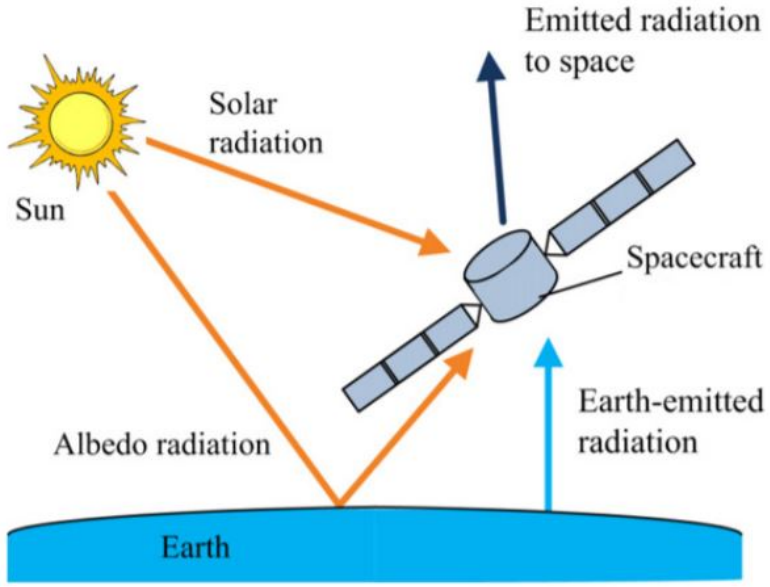

Fig. 2.3: Representation of thermal environment in LEO [26].

The most obvious one is the solar radiation. This effect is measured with the solar constant, C_S. It represents the flux coming from the star and depends on the distance between the Earth and the Sun[1]. Since the Earth has an elliptical orbit, this distance varies over the year. When the

[1]It is assumed that the Sun-Earth and Sun-satellite distances are the same.

Earth is at the closest point (boreal winter solstice), the solar flux is 1414 W/m^2 and 1322 W/m^2 when it is the furthest away (summer solstice). A mean value of 1367 W/m^2 can also be used [27].

Some of the Sun rays are reflected by the Earth's atmosphere or ground before reaching the satellite. This is called albedo radiation. This phenomenon depends on the capacity of the planet to reflect sunlight. The mean albedo coefficient proposed by the European Cooperation for Space Standardization (ECSS) is 0.3 but it is highly variable and depends on both the position on Earth and time. For instance, a value of 0.05 corresponds to oceans while ice caps or high clouds have an albedo coefficient of 0.6 [28].

The Earth-emitted radiation comes from the planet's surface and the atmospheric gases. This radiation is diffuse and from the infrared part of the electromagnetic spectrum. It is also location and time-dependant but varies less than the albedo coefficient. For modeling purposes, the Earth is assumed to be a blackbody in this wavelength domain. A mean equivalent blackbody temperature of 255 K can be used to characterize the energy emitted by the Earth [29]. It corresponds to the mean temperature of the top atmospheric layers (the ground is warmer because of green house effect). It means that the IR radiation of the planet is equivalent to a blackbody emitting at this temperature.

Another environmental load is the aerothermal flux. This one is due to the friction between the atmosphere molecules and the satellite. It is significant only for very low orbits or launch and reentry phases and will thus be discarded in this work.

The last heat load comes from the satellite itself and corresponds to the dissipation of electric power by Joule effect.

Since convection is impossible in space, the only way for the satellite to evacuate its heat is by radiative exchanges with its environment, called Deep Space. This heat sink corresponds to the Cosmic Microwave Background resulting from the Big Bang and is present everywhere in space. It has the spectrum of a blackbody emitting at 3 K.

2.3 Thermal control methods

In order to maintain the different components of the spacecraft within their allowable ranges of temperature, thermal control must be implemented. There are two categories of thermal controls: *passive* and *active*. The first one does not require any mechanical moving parts or moving fluids and thus no power is needed. The main advantages of this method are its easy implementation, reliability, low cost and low mass. On the other hand, those systems cannot achieve a precise temperature and are limited to dissipate low amounts of power. In those conditions, active methods are used since they allow larger dissipation of energy. They can be mandatory for cryogenic applications. The drawbacks of active means are their power consumption and bulkiness.

Tab. 2.1 gives some thermal control methods used in space. The easiest one is to modify the surface properties by applying coatings. Their goal is to change the surface properties and they can be encountered in many forms like paints, plastic film, glass sheets or enhance surface finishes (e.g. polishing, anodizing metals, ...). They can be applied to nearly any surface if a good bonding between the substrate and the coating is used. However, low solar absorptivity coatings (white paint, polished metals, ...) are very sensitive to surface contamination and degrade due to UV radiation and atomic oxygen present is space. The consequence is an increase in the absorptivity coefficient (ϵ remains almost constant) of the surface, making it less effective [30]. It leads to the definition of Beginning Of Life (BOL) and Endo Of Life (EOL) concepts that differentiate between a fresh new coating and one that has been used for a while.

Another way to decrease the effect of the thermal environment on spacecraft's components is

Passive	**Radiation** - coating - MLI blanket - radiator **Latent heat & Ablation** - Thermal protection system - Phase change materials	**Conduction** - structural materials - doubler, filler, adhesive - washer, strap, bolt, stand-off
Active	**Heaters** - thermostat control - electronic control - ground control **Peltier element**	**Heat pipes & fluid loops** - fixed/ variable conductance - loop heat pipes - mono/ diphasic fluid **Louvers**

Table 2.1: Spacecraft thermal control methods [31].

to use Multi Layer Insulation (MLI) blankets. They are made of several layers of aluminized plastics (Mylar or Kapton) separated with very low conductivity materials. The blankets are composed of 10 to 20 layers, each of them being a few micrometers thick.

While those two first methods act directly on the amount of energy received by the satellite from the environment, it is also possible to transfer thermal power from one point of the spacecraft to another. For instance, a specific structural material with a high conductivity could be used to decrease thermal gradients between cold and hot spots. Fillers or adhesives can also be used to increase the heat flow between two contact surfaces. Reversely, it is possible to isolate some parts from each other by using washers or stand-off made of isolating materials like Nylon. Fluid loops are more efficient at transferring heat than passive means. Nevertheless, they are heavier, bulkier and require power to operate the pump which circulates the liquid in the loop.

If transferring heat from one point to another is not sufficient to achieve the desired temperature in a precise area of the spacecraft, localized heaters or Peltier elements can be a solution. The first one is simply based on the Joule effect. When electric current is dissipated in a resistor, heat is produced. The second one uses the thermoelectric (or Peltier) effect. Flowing direct current in an electric junction between two different conductors makes one side of the device heating up and the other one cooling down. Peltier elements cannot achieve large temperature gradients between their two sides but the effect is enhanced by using several of them in series.

Now being able to transfer thermal power from one point to another inside the spacecraft, one wants to evacuate heat to space. The only way to do it is by using radiators. They are made of metal because they need a high thermal conductance between the core and the surface[1]. Moreover, they are covered with high IR emissivity and low solar absorptivity coatings. The high IR emissivity is mandatory because it ensures a better radiation of heat, while the low absorptivity reduces the heating of the radiator when exposed to solar flux (direct or albedo). Louvers or shutters placed in front of the radiators can also be used. When opened, these active mechanisms can reject a heat quantity as much as six times higher than they do when closed [27]. They are thus useful for components presenting a wide variation of internal power dissipation depending on their duty cycle.

[1]Radiation is a surface phenomenon.

2.4 State of the art

This section presents some thermal control systems implemented on CubeSats and the reasons which lead to those choices. Because of the lack of detailed information on this last point for commercial nanosatellites, the majority of the projects presented hereafter come from universities and master's theses.

MIST

MIST (MIniature Student saTellite) [32] is a 3U CubeSat from the Swedish KTH Royal Institute of Technology that should be launched in 2018. The goal of this student satellite is to test eight small payloads developed by KTH and by Swedish industries. Among them, the most demanding ones from a thermal point of view are a propulsive module for which the butane tank must be temperature controlled to avoid freeze up or overheating, an experiment aiming to measure the in-orbit radiation environment that allows a very tight temperature range and an experiment consisting in resuscitating micro-organisms which have been frozen before launch and monitor their growth in orbit. The constraint on this one is to maintain the module's temperature within range suitable for the bacteria's development.

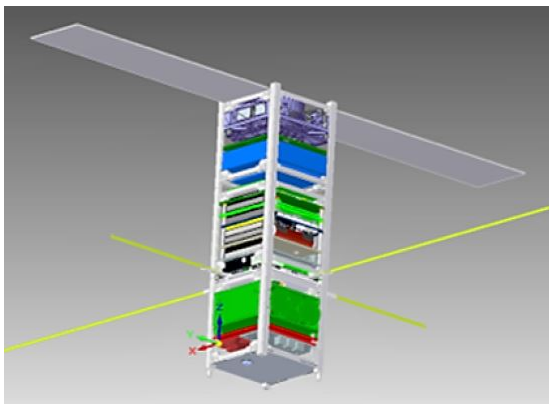

Fig. 2.4: MIST satellite [32].

The satellite has two deployable solar panels (3U each) attached to its small face as well as body mounted ones. Attitude control, consisting in nadir pointing, is achieved by magnetorquers.

The thermal analysis showed that some of the payloads and the batteries were outside their allowable temperature range. To overcome this problem, active and passive methods have been used. A heater is turned on when the batteries are below the threshold temperature. The butane tank of the propulsion module is covered by a plate coated with Teflon and silver to reduce the absorption of environmental fluxes and thus reduce its temperature. On the other hand, this module requires large heaters (6.5 W) during the non-operating cold phase. Additional heaters for the visible camera, for the micro-biology experiment and for some payloads consisting in electronics on PCB were also implemented.

PICSAT

PICSAT is a nanosatellite developed to measure the transit of the exoplanet Beta Pictoris b in front of its star Beta Pictoris. Its goal is to achieve a nearly continuous photometric monitoring of the planet to observe a transit between July 2017 and March 2018. The mission also aimed to study the gas cloud surrounding the young star. The satellite was launched on January 12, 2018 by the PSLV Indian launcher. Unfortunately, the ground station stopped receiving telemetry on March 20,

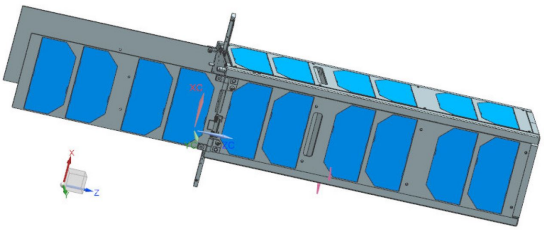

Fig. 2.5: PICSAT satellite [33].

due to an unknown cause[34].

The CubeSat has a 3U form factor with two 2U deployable solar panes attached to one of its small faces, making a 180° angle between them and the body. Moreover, the 4 large faces of the body are also covered with solar cells.

The thermal study depicted in [33] is related to the Phase B of the project. It presents several operational cases (hot and cold) as well as failure scenarios. For the nominal hot and cold cases the simulations showed that the temperatures were compatible with the requirements for nearly all of the satellite's elements. Only the batteries and the solar cells were out of limits. The first one was 2°C too cold in the cold case while the solar cells exceeded the lower barrier by 10°C in the same case. It was suggested by the author to overcome these problems by using a heater for the batteries and a highly conductive material between the solar cells and their deployable or body panels to rise up their temperature.

The first failure scenario assumed the malfunction of the ADCS, leading to one of the small faces of the satellite constantly pointing to the Sun. In this case, every temperature's lower bounds were exceeded, with some of them dropping by 40°C as compared to the normal cold case. A solution proposed was to adjust the surface finishes and to implement a thermal safe mode that would couple the ADCS to a temperature sensor to modify the attitude such that one of the deployable solar panel could face the Sun. On the other hand, the two other failures scenarios assumed the non-deployment of one or two solar panels but it had not much influence on the temperatures of the components.

CIRCUS

Along with the PICSAT study, the thermal analysis of CIRCUS (Characterization of the Ionosphere using a Radio receiver on a CUbeSat) was also conducted but this one is related to a Phase A0, meaning that all the components and the overall configuration of the satellite were not yet clearly defined. As suggested by the name, its primary goal is to study the ionospheric plasma. A secondary payload called STAR (STacked Adcs Receiver) is also embedded in the satellite. The aim of the mission is thus to space-qualify this new digital receiver and increase its technology readiness level.

Fig. 2.6: CIRCUS satellite [33].

One of the tested configurations is a simple 3U design with body mounted solar cells. This one showed temperatures that were 20°C under the lowest bound of the allowable range. This problem was solved by implementing ADCS in order to point one of the large faces of the satellite to the Sun and to increase its temperature. A second configuration consisted in making the satellite spin at a rate of 5 revolutions per hour. This one resulted in a decrease of the external surface temperature outside the accepted range. In the last configuration, two deployable solar panels were used, like PICSAT, and the simulations showed temperatures compatible with the requirements.

NEMO-AM

NEMO (Nanosatllite for Earth Monitoring and Observation - Aerosol Monitor) [35] is a large CubeSat with a volume of 24U (8U exclusively dedicated to the payload) and a large solar panel array. This satellite has been designed for the Indian Space Research Organization (ISRO) by

the Space Flight Laboratory of the Toronto University Institute of Aerospace Studies. The goal of the mission is to observe the Earth to detect the presence of industry-emitted aerosols over India and to target the source of this pollution. The payload is composed of optical instruments and four CCD imagers.

The thermal control system consists in appropriate thermo-optical coatings, adequate materials inside the spacecraft to ensure good conduction and reorganization of the subsystems. For instance, the temperatures were too low and it was deduced that this problem came from the too high emissivity of the exterior body panels of the satellite. It was thus decided to move one of the solar string from the body to the separate solar array tray. In a configuration where the bus was hidden from the Sun by the solar array, the interior of the platform was also too cold. A high emissivity black paint applied to all the inner faces helped rising up the temperature.

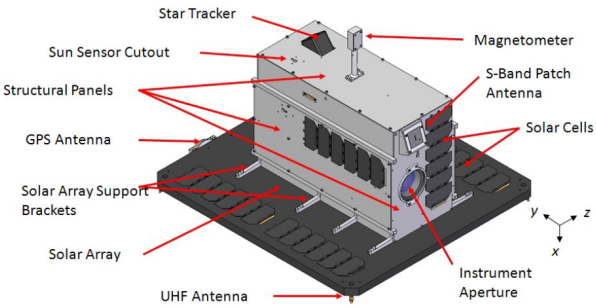

Fig. 2.7: NEMO satellite [35].

In addition to the classical temperature range of the batteries, another constraint had to be considered. The battery pack (composed of 6 individual batteries) must have a uniform temperature. If there is a difference of more than 5°C between the batteries, their electrical resistance are no more the same. This could cause a cross charge phenomenon where one battery charges another one. This effect was avoided by using a thermal gap filler between the cells. Moreover, thermal resistances were also implemented to keep the batteries warm during cold phases. The last thermal strategy implemented for the bus was a thermal strap between the structure and the PCBs to keep them cool by evacuating heat power.

On the other hand, the payload had some special requirements too. The entire optical instrument must have a thermal gradient lower than 5°C between its extremities, the CCDs must be as cool as possible when imaging and their temperature had to be stable. Those constraints have been respected by increasing the overall conductivity of the payload by using silicon aluminum for the structure and by implementing heaters to regulate the CCD's temperature on the go while imaging.

CANX-4/-5

The CANX-4/-5 satellites (Canadian Advanced Nanospace eXperiment 4 and 5) have been studied at the same time as NEMO-AM. The mission consists in two 8U satellites intended to demonstrate autonomous formation flying. Hence, their payload is a cold gas propulsion system [35].

The environment fluxes are regulated thanks to appropriate thermo-optical coatings. Inside the satellites, the heat is transferred from the PCBs to the structure with high conductivity spacers as well as thermal filler and the batteries are kept in their temperature range by heaters. Another concern comes from the propellant valves linking the fuel tank to the active part of the engine. When passing

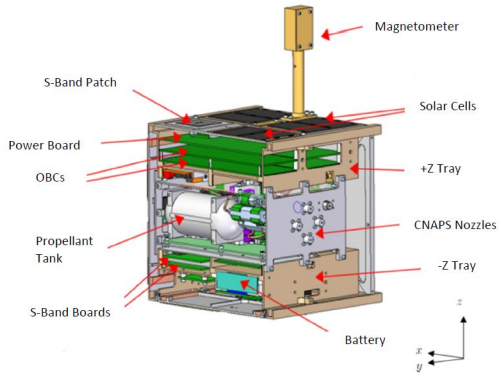

Fig. 2.8: CANX satellite [35].

through the valve, the fuel expends and turns from liquid to gaseous state. This phase change is accompanied by heat absorption which finally reduces the temperature of the valves. It was thus chosen to couple the valves with the structure of the satellite by using a high conductivity thermal strap. With this method, the valves benefited from the larger capacitance of the spacecraft and remained warm enough.

It was initially planned that the two satellites would stay attached to each other just after the launch, for a duration of several orbits. The goal was to calibrate and verify their ADCS modules before they start drifting apart to begin the formation flying phase. In this configuration, one of the spacecraft was partially in the shadow of the other one and suffered from temperatures 35°C lower, meaning that some of the elements were out of their allowable range. Two solutions were tested: on the one hand, enhancing the radiative exchange between the two satellites with optical coatings and on the other hand, increasing the conduction between the two spacecraft by reducing the contact resistance with some filler material. Those solutions did not manage to give acceptable temperatures. Anyway, it is stated in [35] that the idea of joining the satellites has been abandoned for other reasons.

OUFTI-1

OUFTI-1 (Orbital Utility For Telecommunication Innovation) is the first CubeSat developed by the University of Liège. The objectives of this 1U CubeSat were to test a new amateur radio digital technology called D-STAR protocol, use new high efficiency (30%) solar cells from Azur Space and to test a new type of EPS digitally controlled and based on PIC microcontroller. The thermal design was carried out by Lionel Jacques in [36].

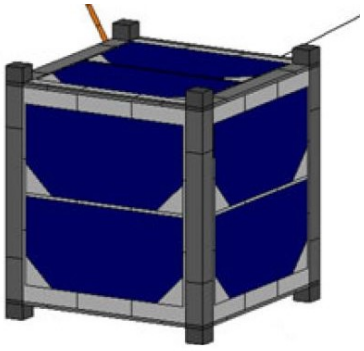

Fig. 2.9: OUFTI-1 satellite [36].

A detailed analysis showed that the temperature of the batteries was too low in the cold case, when the satellites came out of eclipse. Two 250 mW heaters were thus designed, along with three temperature sensors. It was decided by the author that the heaters should turn on when the batteries are 5°C above their lower bound. In addition, in order to increase the efficiency and reduces the thermal loses, the batteries were wrapped in low emissivity aluminum thermal tape. The PCB supporting them was also isolated from the rest of the structure by low conductivity Nylon washers and titanium spacers.

In the hot case, the high dissipation of the transistor on the EPS board induced too high temperatures for the batteries and EPS. This problem was overcome by using a thermal strap encircling the transistor and linking it to one of the satellite's faces. It induced a 10°C drop for the batteries and 20°C for the transistor. Another problem came from the low efficiency of the communication amplifier, thus dissipating too much heat. However, because of the lack of information on this subsystem at that time, no concrete measures were taken except changing its location on the PCB.

NAOS

The NAOS satellite (Nanosatellite for Astronomical Observation of Stars) is a project developed at Centre Spatial de Liège, with the objective of studying massive stars with a UV photometer (250 nm to 350 nm). The thermal design presented in [37], by Nicolas Berckmans

from the University of Liège, is part of the feasibility study of the satellite. The spacecraft will be in LEO and pointing is ensured by a star tracker and reaction wheels.

During the first analysis, it was pointed out that the batteries were extremely hot (over 100°C). The alodine surface finish of the satellite was thus replaced by MAP-PCBE white paint. This resulted in a massive 45°C to 66°C drop. The internal dissipation was also improved by increasing the number of copper layers in the PCBs. Moreover, the inter-subsystem thermal conduction was enhanced with specially designed spacers and filler material. The detector assembly was also modified to reduce the parasitic heat fluxes received from the adjacent subsystems. Moreover, the radiator area was increased.

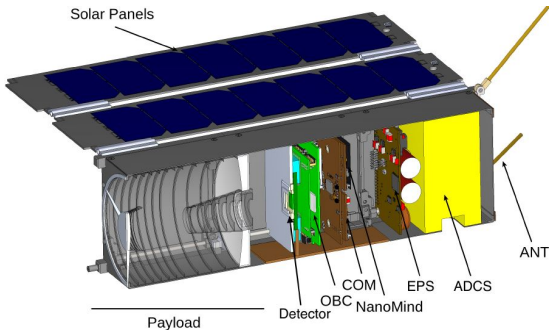

Fig. 2.10: NAOS satellite [37].

Finally, some problems still have to be addressed like the too low temperature of the batteries in cold case, the out of limit temperature of the ADCS in both hot and cold cases as well as the thermal requirements of the detector.

Arkyd-6

The last satellite to be presented in this section is Arkyd-6. This 6U nanosatellite is designed by Planetary Resources, whose ultimate goal is to prospect and mine valuable resources found on asteroids. Nevertheless, the company is only at the beginning of this dream. In fact, the goal of Arkid-6 is to demonstrate some of the technologies which will be used in the larger 12U Arkid-100 satellite, to be normally launched in 2019 [38]. Those two satellites are dedicated to Earth observation. Only the next two models (Arkyd-200 and Arkyd-300) will be dedicated to asteroid prospection to identify valuable resources. At this date, no plan on a future mining spacecraft has been released [39] [40].

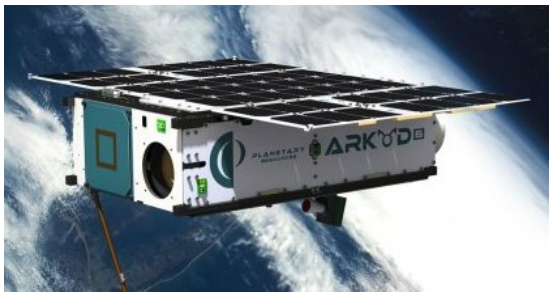

Fig. 2.11: Arkyd-6 satellite [38].

Similarly to OUFTI-Next, the main instrument of Arkyd-6 is a MWIR detector used to measure temperature differences. It is active in the 3.4 to 5.1 μm spectral range and is cooled by a stirling cryocooler at 77 K.

Conclusion

Out of all the CubeSats thermal systems exposed here, some conclusions can be drawn. First, the impact of environmental fluxes is controlled by coatings. It was also observed that the internal faces are sometimes covered with black paint to increase their emisivity. Conduction can be enhanced between different elements by thermal straps, carefully-designed spacers and filler materials. The too cold temperature of the batteries is a recurrent problem. This is solved by electrical heaters, which represent the only active control method used for the satellite's buses.

On the other hand, the payload can be controlled with either passive active methods if the target temperatures are too extreme or if they must stay stable over time. The active systems used for the payloads presented in this section consist heaters and stirling cryocoolers.

3 | Elementary considerations

The present chapter is intended to present the computation of the orbital fluxes. The procedure to obtain them is explained and the results are compared to ESATAN, the standard European space thermal analysis software. Next, the lumped parameter method is implemented and the difference between a static and a cyclic transient approach is exposed. These two methods are then applied to the 1-node *Body Mounted* satellite and the most suitable one is selected for the rest of the study.

3.1 External thermal loads

3.1.1 Solar flux

The solar flux (in W/m^2) received by a face having a normal $\mathbf{n}_i$ is simply given by:

$$q_{S,i} = C_S \left(\mathbf{n}_i \cdot \hat{\mathbf{r}}_S\right) S \,,$$

where $\hat{\mathbf{r}}_S$ is the Sun's unit position vector, C_S is the solar constant and S is a boolean value equal to 1 if the satellite is in the Sun and 0 otherwise.

Because of the very large distance separating the Earth from the Sun and the low altitude of the orbits chosen for the satellite, the penumbra zones are negligible compared to the umbra. The computation of the eclipses is based on the assumption of parallel rays coming from the Sun. The shadow terminator points are determined by a method derived from [41].

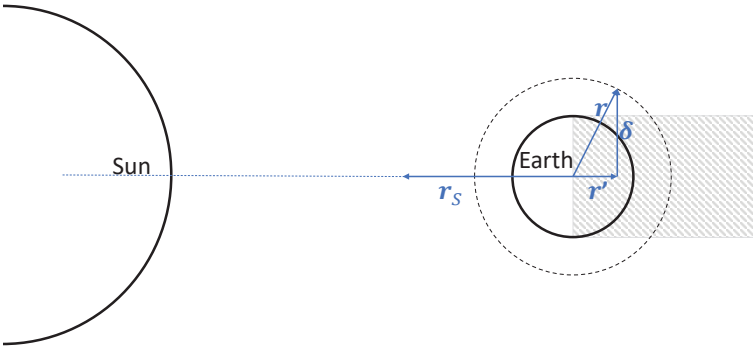

Fig. 3.1: Eclipse terminator points computation.

As seen in Fig. 3.1, the satellite is in the Earth's shadow only if $\mathbf{r} \cdot \mathbf{r}_S < 0$ and $||\delta|| < R_E$.

3.1.2 Albedo flux

To compute the albedo flux, the view factor between the satellite's face and the Earth is required. However, no simple analytic formula gives accurate results for this parameter. Indeed,

the view factor depends on many parameters like the satellite's orientation, its altitude, the angle between its position and the subsolar point[1] (θ) and the minimum angle between the orbital plane and the solar vector (β). A correlation between all those parameters has been made in [27] and is displayed hereafter.

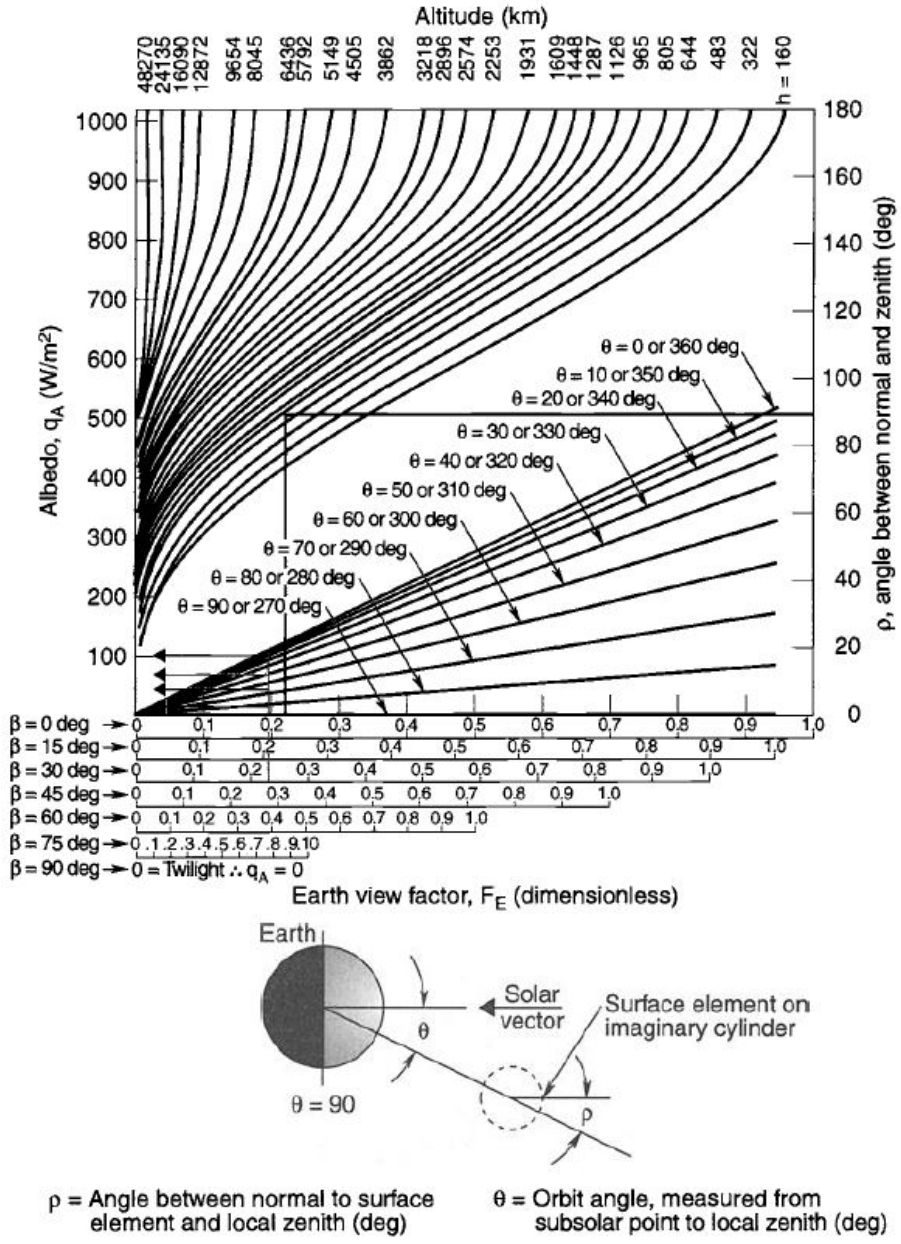

Fig. 3.2: Correlation between the albedo flux and the view factor [27].

Nevertheless, this abacus is not suited for automatic computer calculation. This is why the interpolation derived in [36] will be used instead. It has been shown that the view factor follows the formula:

$$F_{E,i} = r^{2.1} \sin^e \frac{\rho_i}{2} \,,$$

[1]The subsolar point is defined as the point on Earth such that the Sun is exactly overhead (zenith).

where $r = \frac{R_E}{R_E+h}$ and e depends on the orbit altitude such that:

$$e = -160.31r^6 + 723.36r^5 - 1380r^4 + 1394.6r^3 - 780.65r^2 + 226.81r - 21.232\,.$$

Now that the view factors are known, the albedo flux incident to face i can be determined by [42] [43]:

$$q_{A,i} = C_S a \cos^{1.5}(0.9\theta)\, F_{E,i}\,,$$

where a is the albedo coefficient. In this relation, the angle form the subsolar point (θ) is multiplied by 0.9 in order to represent the reality more accurately. When the satellite has passed the terminator line ($\theta > 90°$), it still receives albedo flux from the bright side of the Earth. The albedo flux stops reaching the spacecraft only when $\theta > 100°$. This concept is illustrated in Fig. 3.3.

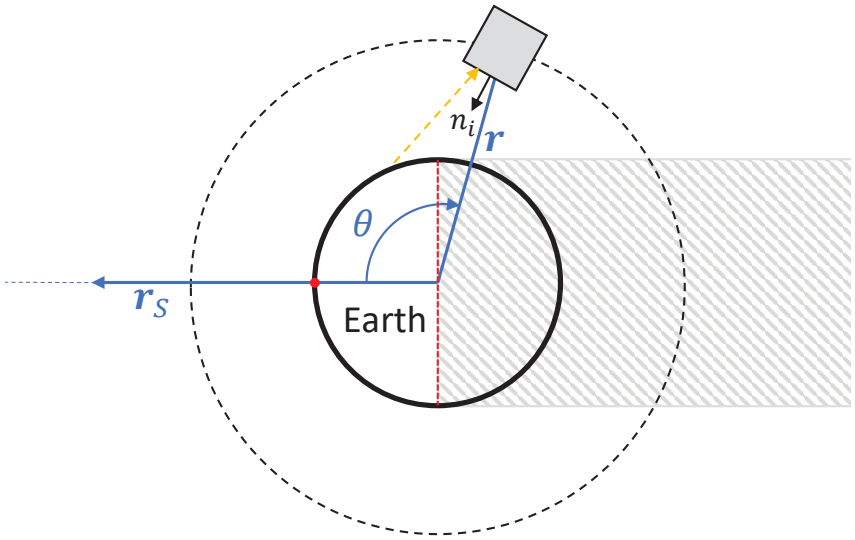

Fig. 3.3: Representation of the albedo flux beyond the terminator line.
Red point: subsolar point, red line: terminator line, yellow arrow: albedo flux.

3.1.3 Earth IR flux

The last environmental load also depends on the view factor between the satellite and the Earth. The formula developed in the previous section is thus reused here.

For the computation of the Earth IR flux, the planet is assimilated to a blackbody at the temperature $T_{E,bb}$ such that the flux is given by:

$$q_{E,i} = E_{bb} F_{E,i} = \sigma T_{E,bb}^4 F_{E,i}\,.$$

3.1.4 Results

The numerical results of the environmental thermal loads presented in this section are illustrated on a 3U CubeSat which has one of its small (10×10 cm) faces constantly pointing nadir and is idealized as a blackbody ($\epsilon = 1$, $\alpha = 1$). Nevertheless, the conclusions remain general and can easily be applied to other satellite's geometries, attitudes and surface coatings. The thermal case chosen here is characterized as *average*[1] and the parameters are summarized in Tab. 3.1.

[1] By opposition to *hot* and *cold* cases that will be introduced later.

Moreover, a 800 km Sun synchronous orbit with a LTAN of 13h30 is used.

Parameter	Value
Solar constant	1367 W/m^2
Albedo reflection coefficient	0.3
Earth blackbody temperature	255 K

Table 3.1: Average environmental parameters.

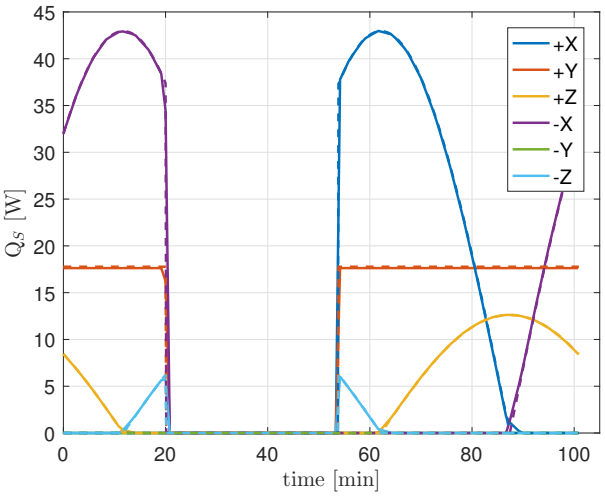

Fig. 3.4: Solar absorbed power.
Solid lines: ESATAN, dashed: MATLAB.

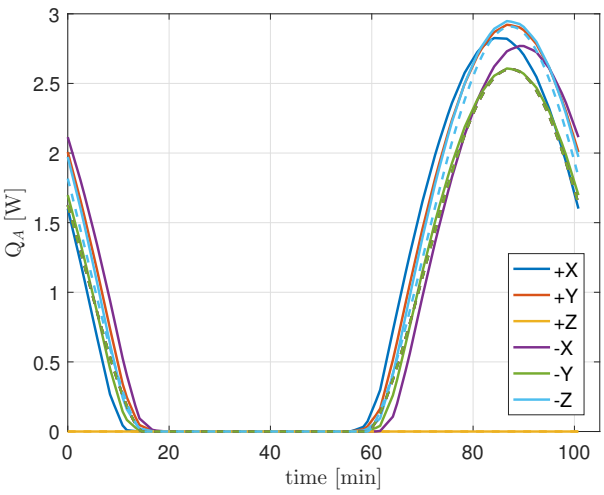

Fig. 3.5: Albedo absorbed power.
Solid lines: ESATAN, dashed: MATLAB

The results are displayed in Fig. 3.4 to Fig. 3.7 for one orbit. The continuous curves have been obtained with ESATAN[1], while the dashed ones are from a personal MATLAB code.

It can be seen in Fig. 3.4 that the absorbed solar power is nearly exactly the same for the two programs. This figure shows that the orbit is subject to eclipses with a duration of approximately 33 minutes. The $-Z$ face is constantly pointing the Earth and thus receives the lowest amount of solar flux. In fact, this amount is above zero only when the satellite is between $\theta = 90°$ and the eclipse entry/exit points. Complementary behaviours between opposite faces of the satellite can also be observed. Such two faces do not receive flux at the same time. For instance, the leading face of the satellite (the face which has its normal parallel to the velocity vector), $+X$ sees the Sun only from the exit point of the eclipse to the subsolar point. While the $-X$ face receives flux from the subsolar point to the eclipse entry point. On the other hand, $+Y$ is subjected to a constant solar load since the angle between this face and the Sun rays is constant during the entire orbit.

The albedo power absorbed by the CubeSat is represented in Fig. 3.5. In this figure, the curves corresponding to the MATLAB computation of faces $+X$, $+Y$, $-X$ and $-Y$ are superimposed. Logically, the $+Z$ face is constantly pointing away from the Earth and thus does not receive albedo flux. There is a small discrepancy between the MATLAB and ESATAN results that can be explained by the following reasons.

The MATLAB implementation is based on what was explained in Section 3.1.2. With this method, for a fixed position of the satellite, the view factor between the spacecraft and the Earth

[1]The modelling process with ESATAN will be detailed later.

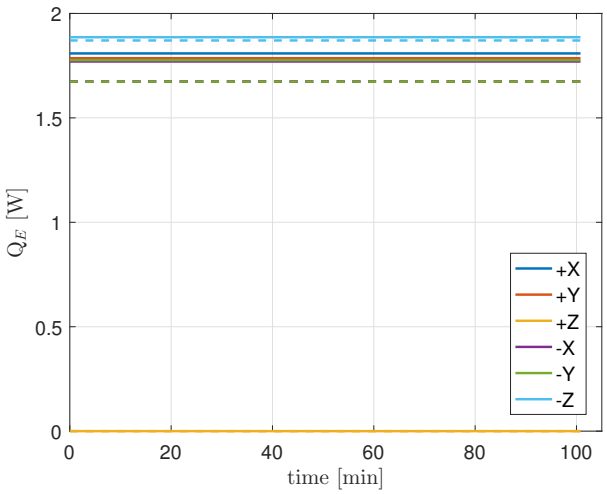

Fig. 3.6: Earth IR absorbed power.
Solid lines: ESATAN, dashed: MATLAB

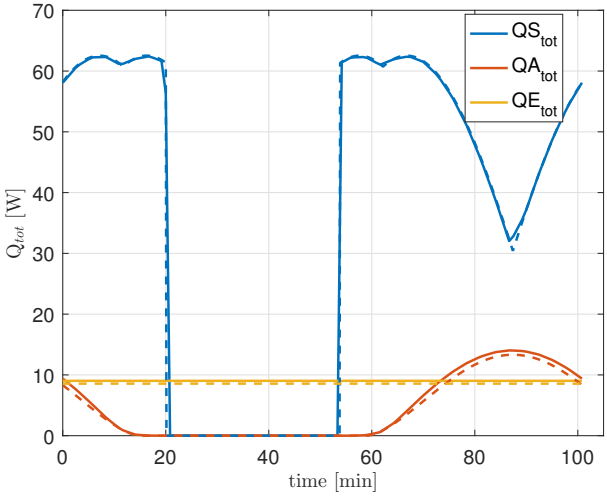

Fig. 3.7: Total absorbed power.
Solid lines: ESATAN, dashed: MATLAB

only depends on ρ (angle between the normal to the face and the local zenith). Since the satellite is pointing nadir, this angle is the same ($\rho = 90°$) for the faces $+X$, $+Y$, $-X$ and $-Y$. Hence, the view factor and the albedo flux are the same.

However, it does not represent accurately the reality. As shown in Fig. 3.8, for a same ρ angle, the faces do not see the same portion of illuminated Earth. The left side of the figure corresponds to the side view of the orbit and shows that the $+X$ face of the satellite sees a smaller illuminated zone of the Earth than the $-X$ face. This behaviour is observed when the spacecraft moves away from the subsolar point. The opposite occurs when the satellite moves closer to this point. The right side of Fig. 3.8 displays the orbit seen from the top. In this case, the $+Y$ face is subject to a larger portion of illuminated Earth than $-Y$ face[1]. These phenomenona are taken into account by ESATAN in Fig. 3.5 (continuous curves), making this software more accurate that the MATLAB implementation.

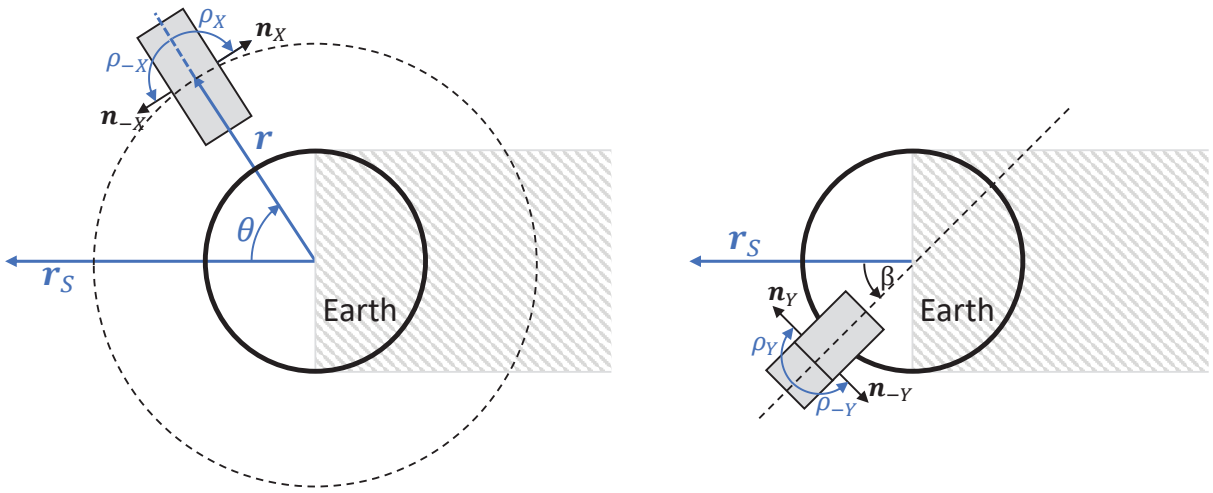

Fig. 3.8: Angle between normal to satellite's faces and local zenith.
Left: side view, Right: top view.

[1]These two faces would receive the same amount of albedo flux only if $\beta = 0°$.

On the other hand, the $-Z$ face does not suffer from this kind of problem concerning the ρ angle. Nevertheless, a very small difference is observed between the two software. This is due to fact that the MATLAB code is based on the abacus presented in Fig. 3.2 which is itself an approximation of the reality. Since the ESATAN results are obtained by ray tracing, they are subject to approximation errors as well.

Fig. 3.6 displays the Earth IR power absorbed by the different faces of the satellite. Since this thermal load does not depend on the illumination conditions, the eclipse has no effect on the results. Moreover, the values are constant because the orbit is circular and the attitude of the satellite is also constant with respect to the Earth. In this graph, the MATLAB curves (dashed ones) corresponding to the sides $+X$, $+Y$, $-X$ and $-Y$ are superimposed. It reflects the reality since those four sides have the same view factor with the Earth when the satellite is pointing nadir. On the other hand, the ESATAN results for those faces are a little bit apart from each other but remain close (they are in an interval of 39 mW). This dispersion comes from the approximations of ray tracing.

Finally, Fig. 3.7 shows the total power absorbed for the three environmental thermal loads. It can be seen that MATLAB and ESATAN give approximately the same results. Hence, the MATLAB algorithm will be used for this first elementary thermal model.

3.2 Static vs cyclic transient thermal models

With the orbital fluxes incident to each face of the satellite determined, it is now time to get a first estimation of its temperature. In this case, the spacecraft is assumed to be isothermal (represented by one node). A *static* and a *cyclic transient* models will be used to compute the temperature. They are both based on the lumped parameter method.

3.2.1 Lumped parameter method

The goal of the lumped parameter method is to simplify continuous systems in a finite number of discrete elements (nodes) forming a network. In the context of thermal modeling, each node is considered isothermal. It is thus characterized by a temperature and a capacitance. The different nodes of the network are joined together by conductive links ($GL_{i,j}$) and radiative links ($GR_{i,j}$).

The governing equation representing the heat balance at node i is:

$$Q_{int,i} + Q_{ext,i} + \sum_j GL_{i,j}(T_i - T_j) + \sigma \sum_j GR_{i,j}(T_i^4 - T_j^4) = C_i \frac{dT_i}{dt} \,. \tag{3.1}$$

In this relation, $Q_{int,i}$ represents the internal power dissipated by node i, $Q_{ext,i}$ is the external power absorbed by the node (solar, albedo and Earth IR fluxes) and C_i is the thermal capacitance (in J/K) of node i. They represent the time dependency of the problem. The right hand side of the equation is the thermal inertia of the node and illustrates how quickly its temperature changes when $Q_{int,i}$ and $Q_{ext,i}$ vary.

When only one node is used to represent the spacecraft (s), the equation simplifies to:

$$Q_{int,s} + Q_{ext,s} + \sigma GR_{s,DS}(T_s^4 - T_{DS}^4) = C_s \frac{dT_s}{dt} \,, \tag{3.2}$$

where DS is the Deep Space ($T_{DS} = 3$K). The radiative exchange factor is given by:

$$GR_{s,DS} = A_{tot}\epsilon_{eq} = A_{tot} \sum_{i}^{faces} \frac{\epsilon_i}{A_i} \,.$$

If the right hand side of Eq. 3.2 is ignored, the equation is independent of time and the problem is characterized as *static*. On the other hand, a *transient* problem is solved if this term is kept in the equation. For space thermal analysis, we speak about *cyclic transient* model. It assumes that the conditions encountered at the end of the orbit are the same as at the beginning of this orbit. This hypothesis is especially justified for low Earth orbits (LEO) since the orbital period (τ_{orb}) is short compared to external variables like the variation of the Sun's position with respect to the Earth. This is why the majority of the thermal results presented in this thesis are shown for only one orbit.

To mathematically enforce the cyclic condition on Eq. 3.2, two criteria have to be respected:

- The temperatures at the end and beginning of the orbit must be the same:

$$|T(t + \tau_{orb}) - T(t)| < tol_1$$

- The temperature slopes at the end and beginning of the orbit must be the same:

$$\left| \frac{dT}{dt}\Big|_{t+\tau_{orb}} - \frac{dT}{dt}\Big|_{t} \right| < tol_2$$

In the MATLAB algorithm, those conditions are checked at the end of each orbit. If they are not met, the initial value of the temperature for the next orbit is set equal to the last temperature value of the previous orbit. This is repeated until convergence is reached. The process is shown in Fig. 3.9

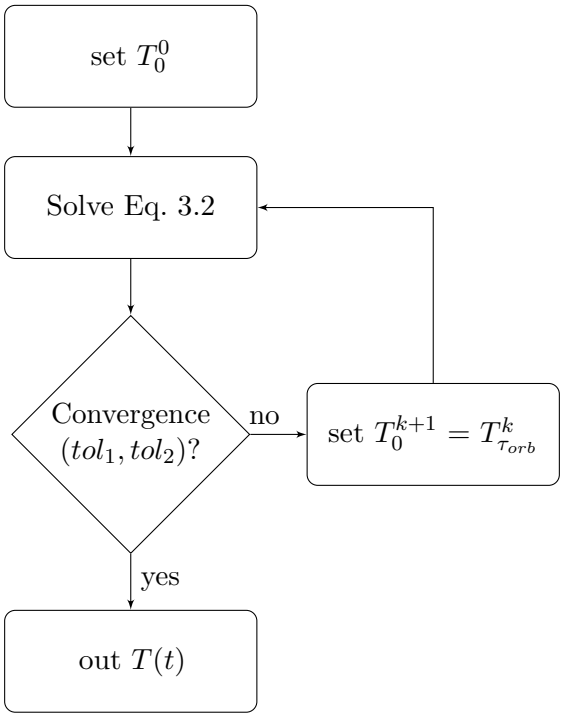

Fig. 3.9: Convergence process of the cyclic transient model.

3.2.2 Implementation and comparison

The comparison between the static and the cyclic transient solvers is conducted on the 3U *Body Mounted* configuration, with the same orbital parameters as in Tab. 3.1. Unlike the previous section, the real surface properties and face layout are used here (see Fig. 1.2). Tab. 3.2 gives the corresponding surface finishes.

Since the project is still in the feasibility phase, the different modules of the spacecraft are not yet fully determined. Thus, the materials listed in Tab. 3.2 have to be considered as assumptions based on manufacturer data sheets and on other CubeSats. Hence, they might change in the future.

The aluminum rails are the only parts allowed to touch the P-POD. According to the CubeSat Design Specification [44], they shall be made of hard anodized aluminum to prevent cold welding between the rails and the orbital deployer. The thermo-optical coating of the radiator has been determined by the COOL subsystem. The coarsest assumptions concern the star tracker and the payload opening holes. Since the role of those two components consists in letting light enter the satellite, their reflection coefficient must be small. It is thus chosen to represent them by blackbodies. Nevertheless, their surface area remains relatively small compared to the whole satellite, meaning that their influence is marginal.

Component	**Material**	α	ϵ	**Reference**
Rails	Al 7075, hard anodized	0.83	0.87	[45]
Shear panels	Al 6061, alodined	0.44	0.14	[45]
Solar cell	CMG anti-reflective coating	0.92	0.85	[5]
Radiator	MAP PCBE white paint	0.27	0.88	[46]
Star tracker	blackbody	1	1	
S-band patch antenna	Kapton foil	0.11	0.33	[27]
GPS patch antenna	Kapton foil	0.11	0.33	[27]
Payload	blackbody	1	1	

Table 3.2: Surface properties for the basic *Body Mounted* configuration.

Static solver

The static results are obtained by solving Eq. 3.2 with the right hand side equal to zero. The 800 km SSO 13h30 LTAN orbit with nadir pointing is used. Since the computation is static, several choices arise for the value of Q_{ext}. One computation is done for the satellite in eclipse and another one when it is in sunlight. The latter is decomposed in two situations. For the first one, one considers the average power received by the spacecraft during the entire sunlight period, while the second scenario is based on the maximum external power (see Fig. 3.10).

The temperature of the satellite for the static solver is given in Tab. 3.3.

Case	**Temperature [°C]**
Eclipse	-96.2
Sunlight (mean Q_{ext})	9.1
Sunlight (max Q_{ext})	51.7

Table 3.3: Static temperatures of the body mounted configuration.

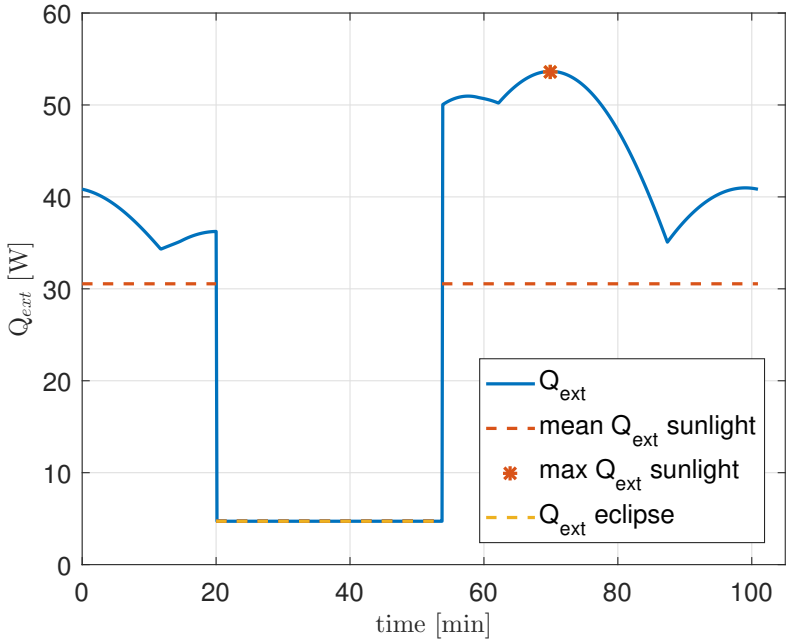

Fig. 3.10: External power (solar + albedo + Earth IR) for static computation. 800 km SSO 13h30 LTAN, average thermal case.

Cyclic transient solver

The cyclic transient solver requires the thermal capacitance (C) of the satellite. An estimation of the mass (m) and specific heat (C_p) of the components is presented in Tab. 3.4. These values will be refined in the next chapters.

Component	m [kg]	C_p [J/Kkg]	C [J/K]	Source
Structure (Al 7075)	0.3	961.2	288.4	[27]
Shear panels (Al 6061)	0.4	961.2	384.5	[27]
Solar cells (140μm thick, GaAs)	0.05	334.8	16.7	[27] [5]
PCB stack (4 boards)	0.3	1300	390	[47]
Batteries (Li-Po)	0.35	1350[1]	472.5	[36]
ADCS	0.4	1000	400	-
Antennas (Al)	0.1	961.2	96.1	[27]
Radiator (Cu)	0.120	385.2	46.2	[27]
Payload	1	1000	1000	[1]
Total	3.02		3096.2	

Table 3.4: Mass, specific heat and capacitance of the body mounted configuration.

Before discussing the results, a convergence analysis has to be done to determine the two tolerance values of the MATLAB algorithm. For this purpose, one observes the asymptotic behaviour of the maximum temperature reached by the spacecraft when the tolerances are reduced (Fig. 3.11). A value of 0.1 is finally chosen for both parameters.

[1]This value corresponds to the value measured by Lionel JACQUES for Lithium-Polymer batteries for the OUFTI-1 CubeSat.

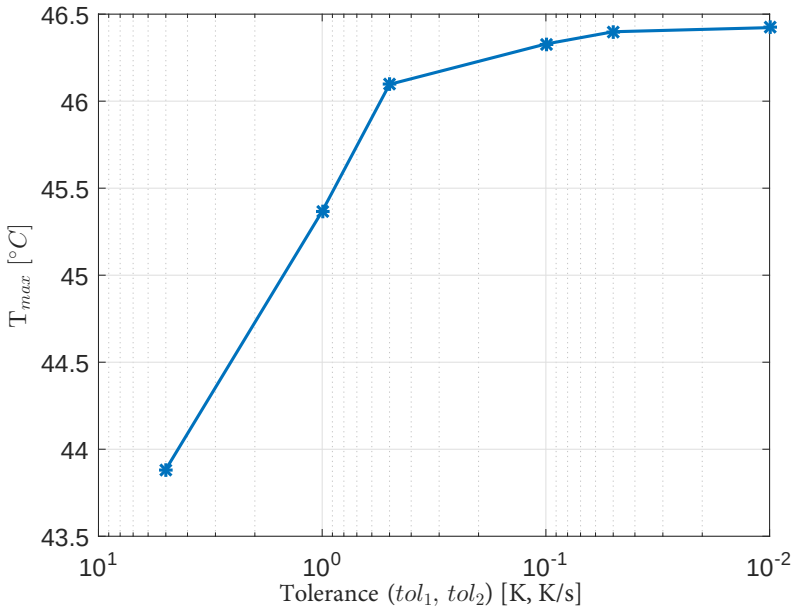

Fig. 3.11: Convergence of the MATLAB cyclic transient model ($tol_1 = tol_2$).

The evolution of the spacecraft's temperature along the orbit is represented in Fig. 3.12. This graph also presents a sensitivity analysis regarding the capacitance[1]. These values are changed by approximately 15% in both directions. One sees that the capacitance of the spacecraft has a limited influence on its temperature. For a total variation of 900 J/K, the temperature changes by only maximum 3°C. When the capacitance increases, the temperature curve flattens, which illustrates the larger thermal inertia of the CubeSat.

A comparison between Tab. 3.3 and Fig. 3.12 shows that the results given by the cyclic transient model are between the boundaries obtained by the static model. Nevertheless, the static temperatures are too far from those obtained by the transient model and it would be too restrictive to design the mission around them. For instance, the lowest temperature in the static case is -96.2°C whereas it is only 30.4°C for the cyclic transient solver. These results were expected since the static case represents the asymptotic behaviour if the eclipse time was infinitely long. For these reasons, the cyclic transient approach will be used for the rest of this work.

[1] A sensitivity analysis regarding the optical properties is conducted in Section 4.6 on the *Body Mounted* 1-node model.

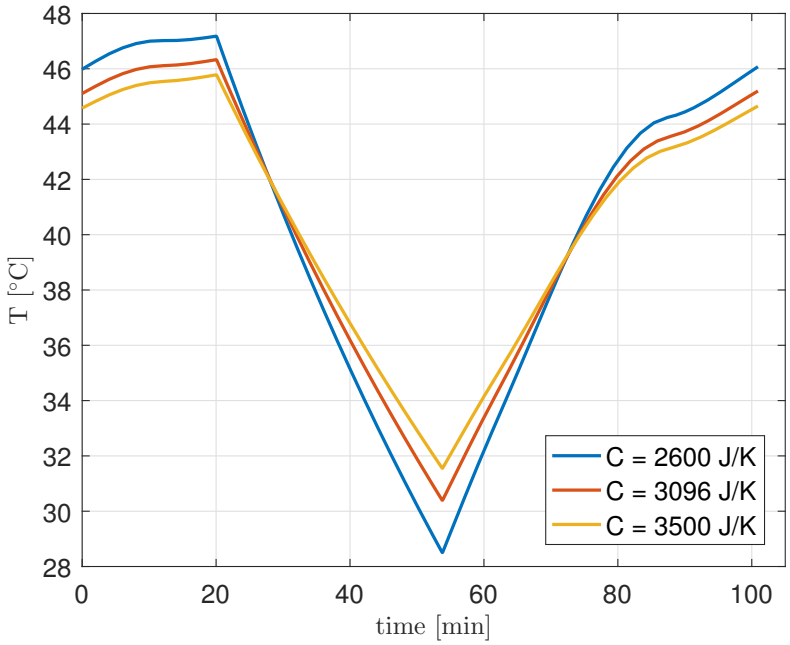

Fig. 3.12: Cyclic transient temperature for the basic body mounted model and sensitivity analysis for the capacitance.
800 km SSO 13h30 LTAN, average thermal case.

4 | Basic thermal model

This chapter presents the concepts of *hot* and *cold* thermal cases, applies them to OUFTI-Next and introduces the modeling procedure with the ESATAN software. The temperatures are computed for different orbits and thermal cases. The spacecraft is modeled by one node for the *Body Mounted* configuration and by three nodes for the *Cross* and *Table* ones. For these last two configurations, a first node represents the body of the satellite, another one models the deployable solar panels and the last one is associated to the solar panel fixed to the body. With this amount of nodes, it is expected to observe the benefits and disadvantages of deployable solar panels.

4.1 Worst cases definition

On one hand, the thermal study of a spacecraft depends on many parameters like the environmental fluxes, the internal dissipation, the orbit, the material properties, ... On the other hand, the role of the thermal engineer is to be sure that the spacecraft remains in its allowable temperature range in all the conditions encountered during its mission. Since analyzing each possible choices of parameters to get the temperature would be too cumbersome, the thermal analysis is based on the worst cases approach. The goal is to study only a few cases that represent the most extreme conditions that the satellite will be subjected to. If the temperatures are compliant with the thermal requirements for the worst cases, they will also be for the intermediate cases.

The *hot* case is thus defined as the case for which all the parameters (satellite and environment related) are chosen such that they lead to the highest spacecraft's temperature. The *cold* case is the opposite, where all the parameters contribute to the lowest satellite's temperature.

The typical variables which are modified in the worst case definition are the eclipse time, the solar constant, the albedo coefficient, the equivalent Earth blackbody temperature, the internal dissipation and the surface properties (BOL vs EOL). However, because of the early phase of the mission, the surface properties are not fixed yet. Thus the difference between BOL and EOL is not taken into account.

4.1.1 Cold case

For the cold case, the solar constant is the lowest and corresponds to the value at the boreal summer solstice ($C_S = 1322$ W/m^2). The Earth blackbody temperature and the albedo coefficient have respective values of 250K and 0.25. Additionally, the eclipse period is considered as the longest. Fig 4.1 and Fig. 4.2 (different y-scales), show the time spent in the Earth shadow for the different orbits studied[1]. One sees that the eclipse varies from 0 to 36 minutes for the ISS orbit while it remains relatively stable for the two Sun synchronous orbits. It also shows that the solstices (dashed lines) do not correspond to the maximum or minimum eclipse duration. It

[1]Those graphs are obtained by the CELESTLAB (SCILAB) software from CNES.

means that in reality, for the ISS orbit for instance, the satellite will not encounter an eclipse of 36 min and a solar constant of 1322 W/m^2 at the same time. Nevertheless, it is chosen to consider these two values simultaneously. By doing so, the worst cold case possible is achieved.

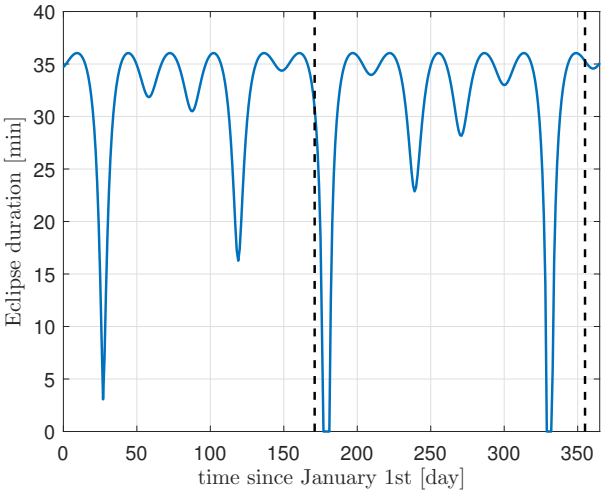

Fig. 4.1: Eclipse duration for ISS orbit.

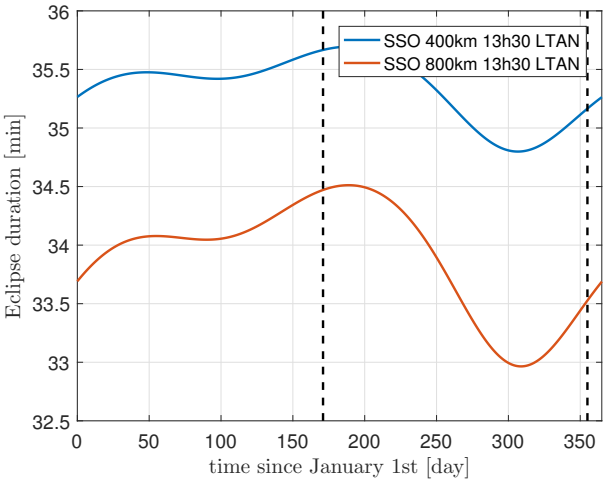

Fig. 4.2: Eclipse duration for SSO.

Moreover, in order to get the lowest temperature, it is assumed that there is no internal dissipation in the spacecraft. It is an ideal situation where the whole power collected by the solar cells is consumed. It is carried without losses to the different modules of the satellite and the components are assumed to operate without dissipation of thermal energy.

4.1.2 Hot case

In the hot case, the eclipse time is minimum (no eclipse for the ISS orbit) and the solar constant is maximum at 1414 W/m^2 (winter solstice), which corresponds to the moment when the Earth is at the closest distance from the Sun. The albedo reflection coefficient and the Earth equivalent blackbody temperatures are respectively 0.35 and 260 K.

Additionally to these external parameters, the internal dissipation of the satellite is considered maximum. It is assumed that all the electric power generated by the solar cells is dissipated in heat. Once again, this is an idealization of the reality. In practice, all the power cannot be dissipated because a part is used to operate the component.

For the basic thermal model, only the idle mode is studied. In this situation, the spacecraft is oriented in such a way that it produces a maximum of electrical power (Sun pointing). This case is the most representative one because it lasts the major part of the orbit. The two operational cases (imaging and communication) will be studied later, with the advanced thermal model.

Outside eclipses, the power produced by the satellite when it points the Sun is given by:

$$Q_{prod} = nA_{cell}C_S\eta\cos\gamma\,,$$

where n is the number of solar cells, A_{cell} is their surface area (28 cm^2), η is the cell's efficiency (28%) and γ is the angle between the Sun rays and the normal to the solar cells. This angle is zero for the *Cross* and *Table* configuration but not for the *Body Mounted* one (cf. Section 1.5). On the other hand, it has been established by the SYSE subsystem in [2] that the satellite consumes 5.18 W ($=Q_{cons}$) in Sun pointing mode[1]. For the thermal hot case, this power is

[1]This value includes a 20% security margin.

dissipated by the body node of the satellite.

The question of where to dissipate the remaining $Q_{prod} - Q_{cons}$ arises. For the OUFTI-1 CubeSat [36], the choice was made to design a dedicated transistor whose role was to dissipate the remaining power. Unfortunately, it was the cause of nearly all the problems in the hot case. Indeed, the dissipation system was placed on the EPS circuit board but lead to a local hot spot of 115°C. The high temperature caused the EPS PCB to get out of its allowable thermal rage. It was also the case for the batteries which were directly above the hot spot. To solve these issues, it was decided to relocate some of the power from the EPS to the antenna deployment panel by using two resistances in series with the dissipative transistor. To increase the transfer of thermal power between the two parts, a copper strap was also designed. One end of the strap encircled the transistor while the other was strongly bolted to the antenna deployment panel. Those drastic measures lead to a decrease of the temperature of the batteries, the EPS and the transistor. For OUFTI-Next, it is chosen not to use this dissipatvie transistor technique because of the hassle caused by this system in OUFTI-1. Instead, the remaining power will be dissipated at the solar cells' level. This method should reduce the risk of hot spots for both the payload and the satellite's platform.

There are two possibilities to model the power dissipated by the solar cells during the orbit. In the first case, the extra power received in sunlight is directly dissipated, meaning that nothing is dissipated at the solar cells' level during eclipse. On the other hand, one could imagine a mechanism allowing a constant dissipation during the entire orbit. In this case, the cells dissipate an average power given by $(Q_{prod} - Q_{cons})\tau_{sunlight}/\tau_{orb}$. The two possibilities are presented in Fig. 4.3.

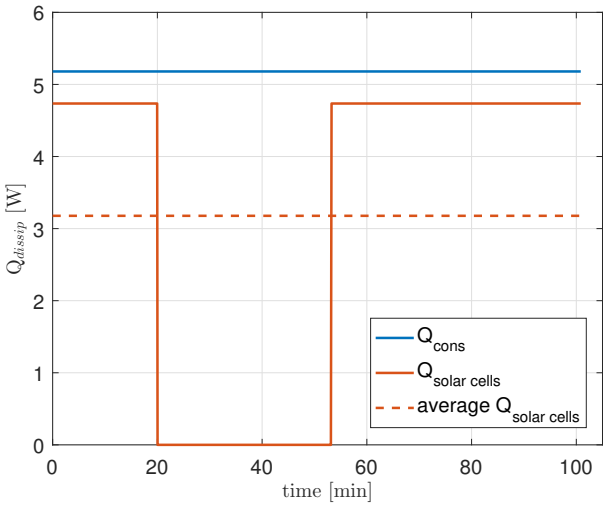

Fig. 4.3: Dissipation schemes for the *Body Mounted* configuration.

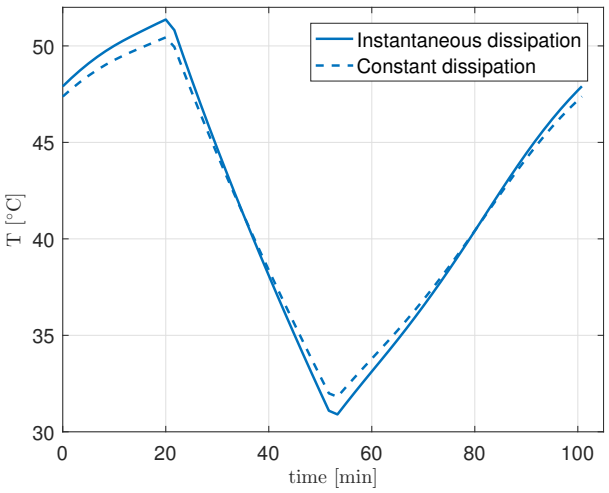

Fig. 4.4: Comparison of the temperature profiles for the *Body Mounted* configuration and different internal dissipation schemes.

The dissipation scheme selected for the thermal hot case of the satellite is the one leading to the highest temperatures. For that purpose, Fig. 4.4 displays the temperature of the *Body Mounted* configuration for the two choices. It can be seen that the instantaneous dissipation leads to the largest thermal load. It will thus be considered for the rest of the study[1].

Finally, the parameters chosen for the cold and hot cases are summarized in the following

[1]The conclusion is the same for the *Cross* and *Table* configuration but the graphs are not shown here for brevity sake.

table. In the hot case, for the dissipation at the solar cells' level, the three values are respectively for the *Body Mounted*, *Cross* and *Table* configurations. Moreover, these numbers correspond to the dissipation when the spacecraft is in sunlight only.

Parameter	Cold case	Hot case
Solar constant [W/m^2]	1322	1414
Albedo reflection coefficient [-]	0.25	0.35
Earth equivalent blackbody temperature [K]	250	260
Internal dissipation (satellite's body) [W]	none	5.18
Internal dissipation (solar cells) [W]	none	4.73 ; 23.64 ; 14.77

Table 4.1: Hot and cold cases parameters for the basic thermal model.

4.2 Thermal modeling with Esatan

ESATAN-TMS (for Thermal Modeling Suite) is the standard ESA's software for thermal analysis. It divides the analysis process in two parts: the Geometric Mathematical Model (GMM) and the Thermal Mathematical Model (TMM).

The first one is dedicated to the determination of the external orbital fluxes as well as the computation of the radiative exchange factors between the satellite's surfaces. This last point requires the knowledge of the view factors which are determined by ray tracing. For a perfect accuracy, one should fire an infinite amount of rays, having each their own initial direction. Obviously, it cannot be done in practice and a stochastic approach called Monte Carlo Ray Tracing (MCRT) is used instead. The method fires a fixed amount of rays from the different faces of the spacecraft and registers their path form the point of emission to the absorption point, including the emission direction and the ray/face interactions. The view factors are then computed by averaging the results of the different rays. The process is thus governed by two parameters: the number of rays and the seed. The seed is a value that initializes the pseudo-random number generator used for the stochastic method. As seen in Fig.4.5, two different seeds will produce different results. However, their statistical property states that the evolution of the resulting view factor stays within a band whose width is inversely proportional to the square root of the number of rays fired. On the other hand, because of the intrinsic deterministic behaviour of computer software, two identical seeds will produce exactly the same results [48].

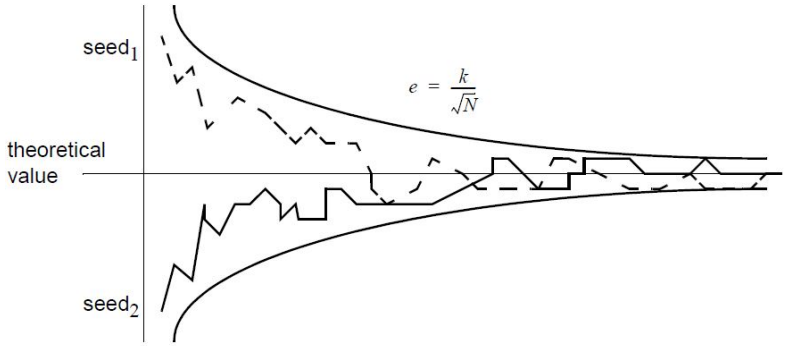

Fig. 4.5: Evolution of MCRT-calculated entities according to ESATAN user manual [48].

The main drawback of the method is the time needed for the computation. Moreover, this time increases when the surfaces have low emissivities, since the number of reflections before

absorption of the ray is greatly increased too. This is why a convergence analysis is required to determine the best compromise between the computation time and the accuracy.

On the other hand, the Thermal Mathematical Model uses as inputs the results of the GMM to determine the temperatures. They are obtained by the lumped parameter method which assumes that the nodes are isothermal.

Because of the low parametrization capabilities of ESATAN and the various orbits and configurations that are considered for OUFTI-Next, the preprocessing is done with MATLAB scripts. It includes the determination of the orbital parameters, the nodes' capacitances, the dissipation profiles of the spacecraft's components and the conductive links between the parts. These inputs are then introduced in ESATAN which computes the temperatures. Finally, the results are postprocessed by a MATLAB code provided by Lionel JACQUES and adapted by myself.

4.3 Geometric Mathematical Model

The face layouts of the different configurations used for the basic thermal model are presented in Fig. 1.2, Fig. 1.3 and Fig. 1.4, while Tab. 4.2 lists the surface properties needed to compute the radiative exchange factors.

Component	Material	α	ϵ	Reference
Rails	Al 7075, hard anodized	0.83	0.87	[45]
Shear panels	Al 6061, alodined	0.44	0.14	[45]
Solar cell	-	0.72	0.85	[5]
Radiator	MAP PCBE white paint	0.27	0.88	[46]
Star tracker	blackbody	1	1	
S-band patch antenna	Kapton foil	0.11	0.33	[27]
GPS patch antenna	Kapton foil	0.11	0.33	[27]
Payload aperture	blackbody	1	1	
Deployable panel	Titanium	0.4	0.55	[27]

Table 4.2: Thermo-optical properties of the basic models.

The power balance at the solar cells' level is depicted in Fig. 4.6 if the circuit is closed (i.e. they produce electricity).

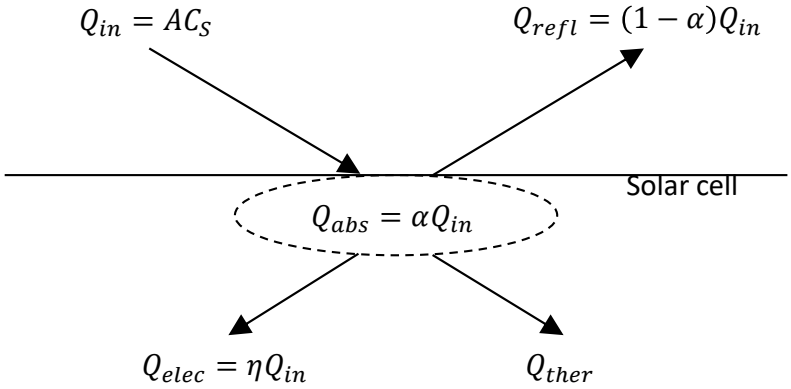

Fig. 4.6: Power balance at the solar cells' level.

The power incident to the solar cells, Q_{in}, is simply the product of the projected surface area and the solar constant. Multiplying this quantity by the solar absorption coefficient gives

the absorbed power: Q_{abs}, a part of which being used to produce electricity (Q_{elec}) and the remaining $Q_{abs} - Q_{elec} = Q_{ther}$ being responsible for heating the solar cells.

The manufacturer specifies that the efficiency η corresponds to the AM0 value. Hence, it refers to the incident power and not to the absorbed one. Thus, the thermal power is given by:

$$Q_{ther} = Q_{abs} - Q_{elec} = (\alpha - \eta)\, Q_{in} = (\alpha - \eta)\, AC_S\,.$$

Because the absorption coefficient is large (> 0.9) and its precise value unknown (the exact solar cell's model is not selected yet), a value of 1 is retained. By doing so, the power heating the solar cells becomes $Q_{ther} \approx (1 - \eta)\, AC_S = \alpha_{eq} AC_S$. This assumption ensures a conservative approach by artificially increasing the part of the incident power which is converted in heat. Since the cell's efficiency is 28% [5], the equivalent absorption coefficient α_{eq} is 0.72. This explains the value written in Tab. 4.2.

According to the manufacturer [4], the deployable panels supporting the solar cells are made of 0.25 mm thick titanium. For this first thermal analysis, a bare metal surface, without any additional coating for the thermo-optical properties is considered. This aspect may change for the advanced model.

The last step concerning the GMM is the convergence analysis of the radiative exchange factor (REF) with the number of rays. It has been conducted on the REF between one of the deployable solar panels and one side of the satellite's body for the *Cross* configuration. Fig. 4.7 displays the results for different seeds and shows that the relative error is smaller than 1.5% if 10 000 rays (or more) are fired. This error is considered acceptable and this amount of ray is employed for the rest of the analysis.

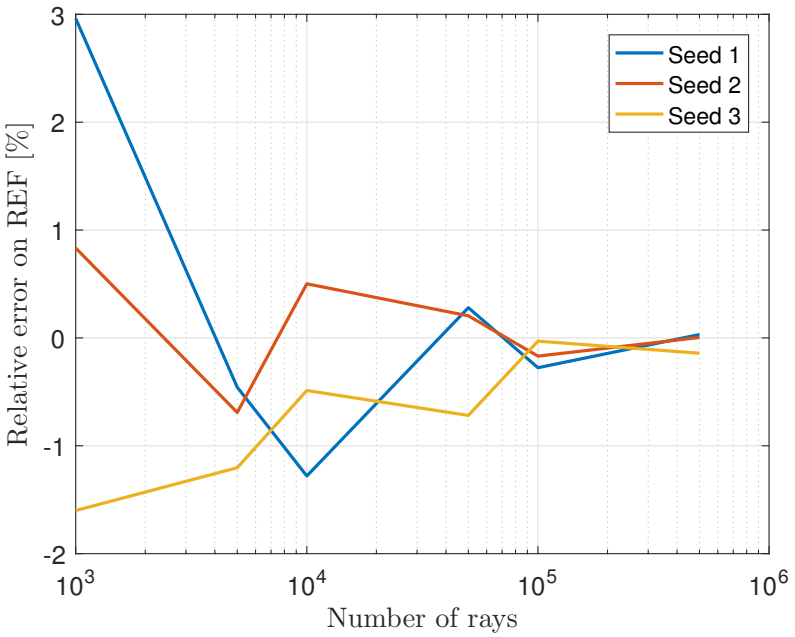

Fig. 4.7: Convergence analysis of radiative exchange factor.

4.4 Thermal Mathematical Model

The nodes' capacitances of the different configurations are listed in the following table. They are based on the values exposed in Tab. 3.4. Additionally, titanium panels ($C_p = 522$ J/Kkg) are considered for the deployable structures of the *Cross* and *Table* shapes.

Node	Body Mounted	Cross	Table
body	3200	3000	2700
deployable solar panels	n/a	400	200
fixed solar panel	n/a	50	150

Table 4.3: Nodes' capacitances of the basic thermal models [J/K].

For the two 3-nodes models, linear conductances must be evaluated. In first estimation, it is assumed that the deployable panels are conductively isolated from the rest of the spacecraft. This simplification is motivated by the fact that the hinge mechanism linking the solar panels to the structure is unknown at this stage of the design. Moreover, in practice, this kind of mechanism has a very low thermal conductance. Indeed, for CubeSats, they can be of two types: classical hinge or flexible bent strap. The first one is composed of male and female parts (see Fig. 4.8) and is usually spring loaded. The conductive heat path from the solar panel to the structure crosses the contact surface between the pin and the female part. Since the hinge is designed to rotate freely, one deduces that the contact is not tight and the heat resistance is high.

On the other hand, bent strap hinges (see Fig. 4.9) operate like a metal measuring tape and are composed of only one piece, meaning that there is no contact resistance. Nevertheless, the cross section over length ratio is small (thickness below 1 mm), resulting in a high thermal resistance.

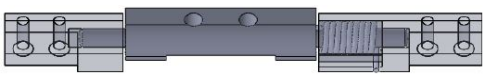

Fig. 4.8: Classical hinge [37].

Fig. 4.9: Longitudinal bent strap hinge [49].

In contrast to the deployable solar array, conductive links have to be considered for the fixed solar panels because they are directly mounted on the spacecraft's body. One has to compute the thermal resistance from the solar panel to the node representing the satellite's body. The latter is placed at the center of the spacecraft. The heat path is different for the two configuration and is detailed hereafter.

Cross configuration

The ISIS structure as well as the panel supporting the body mounted solar cells (orange) are represented in Fig. 4.10. Starting from the panel, the conductive path crosses a contact resistance represented by the purple screw linking it to the rib of the structure. Then, the heat runs in the rib, before going through the vertical blue rail via another contact resistance (red screw), until reaching the center of the body.

While the conductances through the bars (rail and rib) can easily be computed, the contact resistances cannot. In practice, they are difficult to evaluate and no analytic formula exists to characterize them. In fact, they depend on the bolt size, the thickness and material of the plate that it fastens as well as the surface finish. Their thermal resistance is estimated by empirical

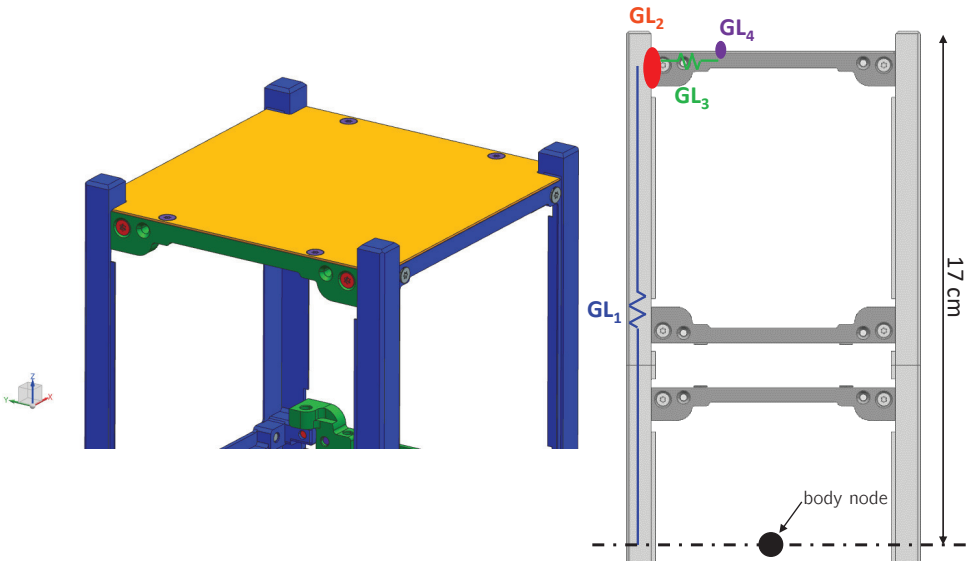

Fig. 4.10: Conductive link between the fixed solar panel and the ISIS structure - *Cross*. Left: 3D model of the structure; Right: equivalent conductive network.

observations. In this case, Tab. 8.5 of *Spacecraft Thermal Control Handbook* by D. Gilmore is used [27]. The closest match between the data available in the table and the ISIS structure gives a thermal resistance of 12.6 K/W ($GL_2 = GL_4 = 0.0794$ W/K).

Finally, the total conductance between the fixed solar panel and the structure is given by the following equation, where a factor 4 is used to represent the heat conduction through the four rails in parallel.

$$GL_{struct,fixed\ sp} = 4\left(\frac{1}{GL_1} + \frac{2}{GL_2} + \frac{1}{GL_3}\right)^{-1} = 0.0395\text{W/K}$$

If the contact was assumed perfect (no thermal resistance), a conductance of 0.0527 W/K would have been obtained, a value 25% larger than the one computed before. It shows that contact resistances play a major role and cannot be neglected when computing the conductive path from the body mounted solar panel to the structure.

In addition to the conductive link, a radiative one can also be considered between the fixed solar panel and the body node. Since the body of the satellite is entirely under the solar panel and since both have the same footprint, the radiative coupling only happens inside the spacecraft, between the underside of the panel and the body node. The upper part of the satellite's body is occupied by the PCB stack. Because the last circuit board is close to the top panel and has approximately the same size, it is reasonable to guess that the view factor between the two parts is 1. With an emissivity of 0.86 for the PCB ([50]) and 0.81 for the underside of the panel, the radiative exchange factor is $GR_{fixed\ sp,PCB} = 0.0072$ m^2.

For a temperature difference between the two components under 100°C, the ratio of the power exchanged by conduction on the one exchanged by radiation varies between 0.9 and 1.5, if the hottest part is at 300 K. It shows that both phenomena are equally important.

Table configuration

In the *Table* configuration, the fixed solar panel is mounted on one of the large faces. The structure as well as the equivalent conductive network are presented in Fig. 4.11. Because the

two contact resistances are very close to each other, they are considered at the same place and the rib is ignored. The heat path from the solar panel to the body node is thus simply composed of the two screws resistances, followed by a 5 cm travel along the structure of the spacecraft.

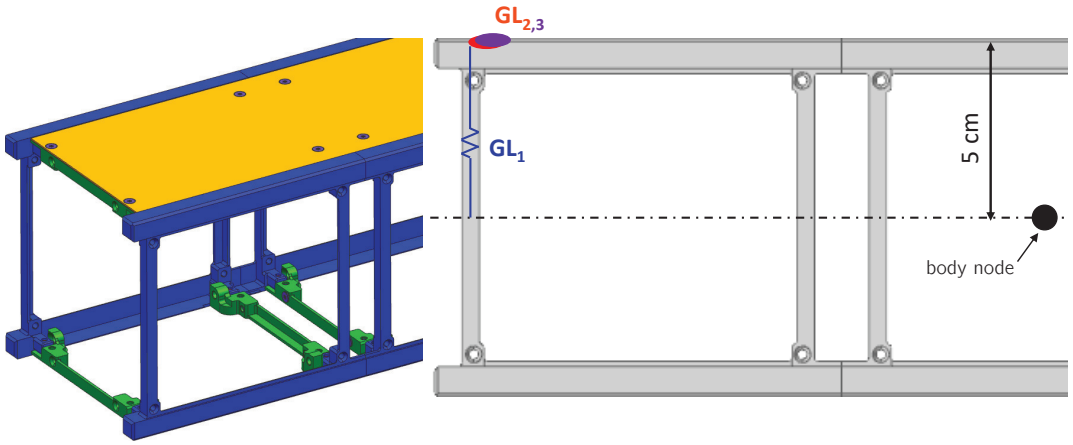

Fig. 4.11: Conductive link between the fixed solar panel and the ISIS structure - *Table*. Left: 3D model of the structure; Right: equivalent conductive network.

The total conductance is computed in the same way as for the *Cross* configuration except that there are 12 identical paths in parallel:

$$GL_{struct,fixed\ sp} = 12\left(\frac{1}{GL_1} + \frac{2}{GL_2}\right)^{-1} = 0.2171\text{W/K}\,.$$

Because of the smaller distance travelled through the structure and the higher number of paths, the conductance is five times larger for the *Table* configuration than for the *Cross*. Once again, the contact resistances cannot be neglected. Otherwise, a conductance of 0.4 W/K would be obtained, which is 45% larger.

Summary of the TMM

Fig. 4.12 summarizes the thermal mathematical models of the three basic satellites by displaying the equivalent thermal network composed of nodes and radiative/conductive links.

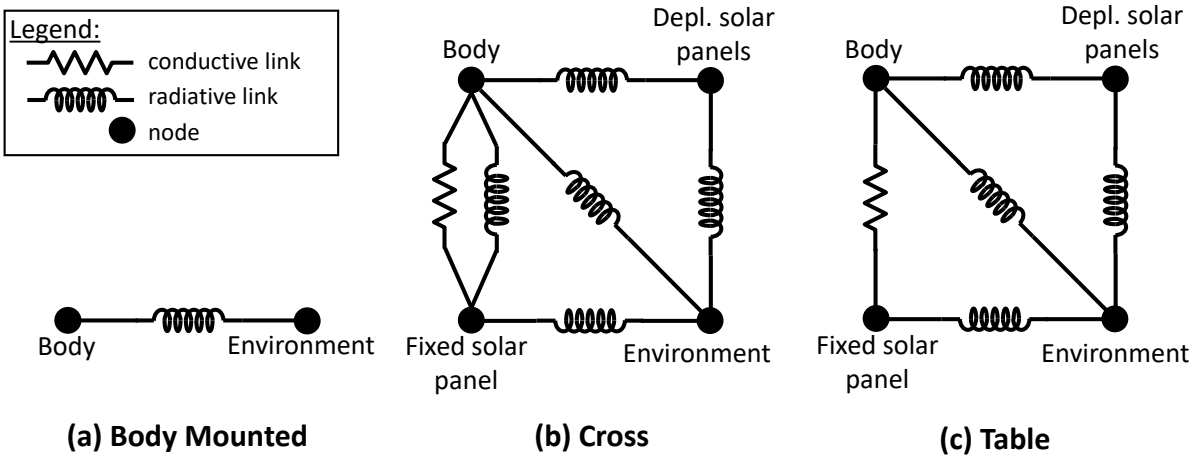

Fig. 4.12: Equivalent thermal network of the three basic satellite's models.

4.5 Results

Fig. 4.13 displays the temperature results of the basic thermal model for the three spacecraft's nodes (body, deployable solar panel and fixed solar panel) in both hot and cold cases. The blue bars refer to the *Body Mounted* satellite's shape, the green colors represent the *Cross* configuration and the red ones are associated to the *Table*.

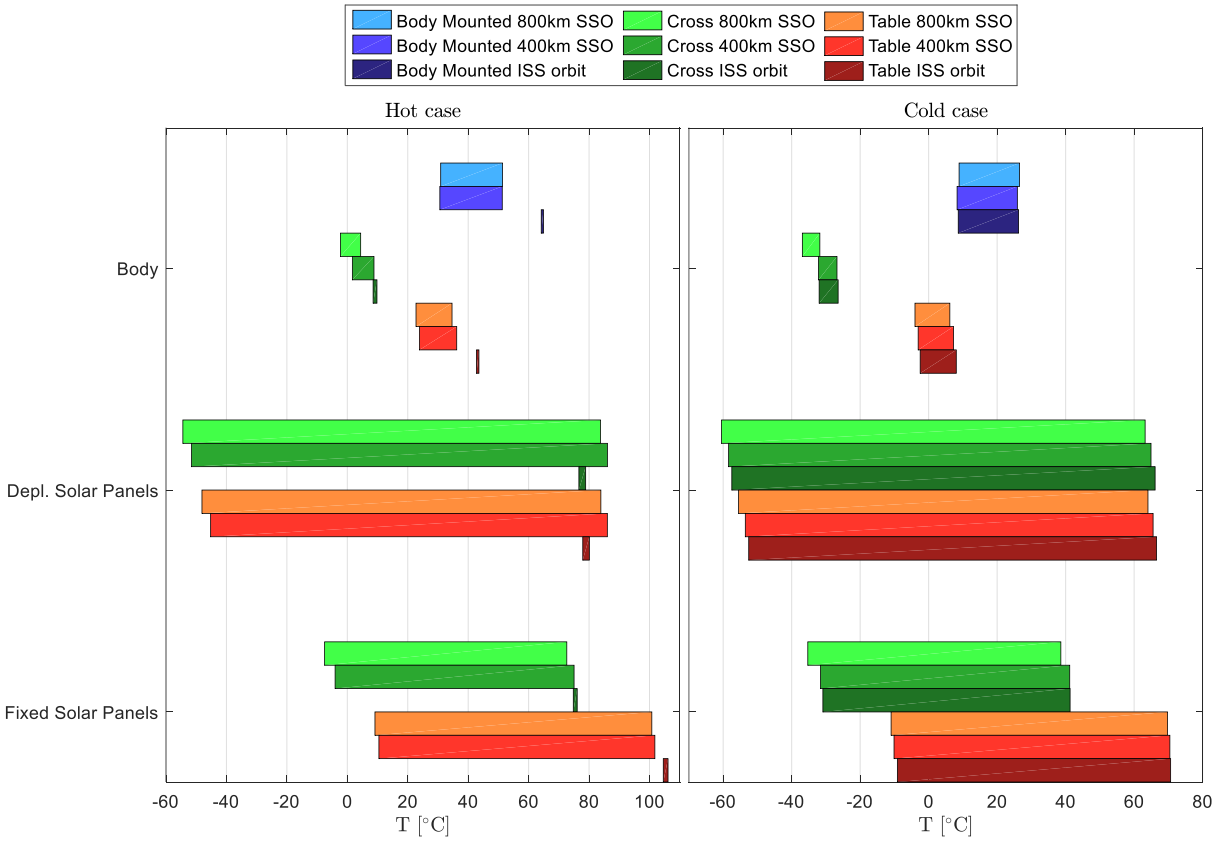

Fig. 4.13: Temperatures of the basic models for different orbits, configurations and thermal cases.

While this figure allows a global view of all the results and eases the comparison between the different cases, it lacks the time-dependence of the temperatures. Indeed, it is not possible to know how long a component stays at a given temperature by looking only at this figure. For this reason, two representative orbits are shown in Fig. 4.14 and Fig. 4.15. The first one corresponds to the cold 800 km SSO, the grey zone representing the eclipse period. It is seen that the temperature starts to decrease at the beginning of the eclipse and the components are the coldest at the end of this period. Then, the temperature rises until the end of the orbit. Because of the larger capacitance of the body node, its temperature variation is small compared to the other nodes. The same curves' shapes are obtained for all the orbits except for the hot ISS. The latter is represented in Fig. 4.15 which shows that there is no eclipse. Hence, the temperatures are stable along the entire orbit period.

Fig. 4.13 shows that the deployable solar panels undergo the largest temperature variation. It illustrates their lower capacitance and the fact that they are conductively isolated from the rest of the spacecraft. On the other hand, the fixed solar panels benefit from the larger thermal inertia of the structure on which they are attached.

It can be seen in all cases, that the largest body node's temperature is obtained for the *Body Mounted* configuration while the smallest one is for the *Cross*. This is explained by the

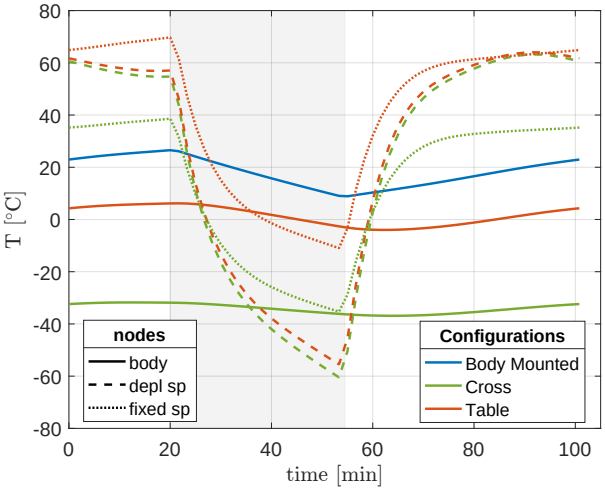

Fig. 4.14: Temperatures of the basic models Cold case, SSO 800 km 13h30 LTAN.

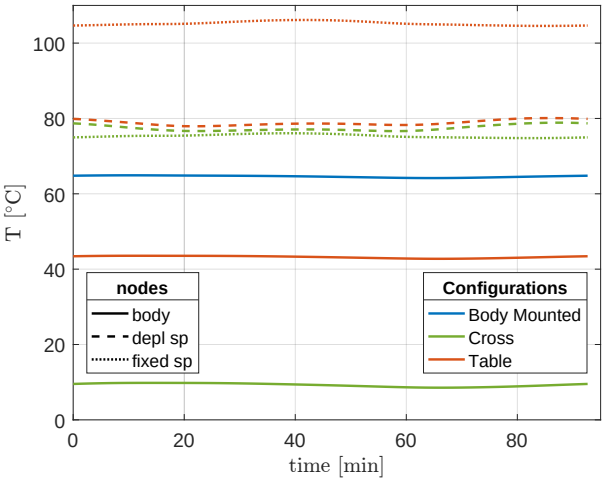

Fig. 4.15: Temperatures of the basic models Hot case, ISS orbit.

fact that the body of the deployed configurations is located in the shadow of the solar panels. Since these solar arrays are constantly pointing the Sun, the spacecraft's core does not receive direct solar flux. Moreover, the *Table*'s temperature is larger than the *Cross* because the solar panel attached to the structure is larger and its conductive link to the body is more important. It is thus expected that the coldest payload's temperature will be encountered for the *Cross* configuration.

A comparison between the different orbits shows that the coldest orbit is the high altitude SSO in both hot and cold cases. It is explained by the lower albedo and Earth IR fluxes induced by the higher altitude. On the other hand, the solar constant does not change for these low Earth orbits.

Because of the lack of eclipse in the hot ISS orbit, the components show the lowest temperature variations in this thermal case. However, the variation is not strictly null. Indeed, the albedo and Earth IR fluxes vary because of the eccentricity of the orbit. Comparing the left and right sides of Fig. 4.13, it is observed that the ISS orbit leads to the largest thermal gradient between hot and cold cases. The temperature difference can be as large as 40°C if the body node is considered.

One sees that this orbit leads to the hottest temperatures for the body node and the fixed solar panels. It is thus expected that the internal components subjected to this orbit will be the hottest. However, these simple 1 or 3 nodes models do not allow to determine the temperature of the individual spacecraft's elements. Hence a more detailed model is needed.

4.6 Sensitivity analysis regarding the optical properties

The sensitivity analysis regarding the optical properties is shown in Tab. 4.4 and Tab. 4.5. They represent the temperature variation between the nominal case ($\epsilon \times 1$, $\alpha \times 1$) and the other cases. Tab. 4.4 illustrates the sensitivity on the maximum temperature reached by the 1-node *Body Mounted* configuration, while Tab. 4.5 corresponds to the minimum temperature.

Both tables show that the largest variation occurs when the emittance and absorptance vary oppositely (along the diagonal linking the bottom left and top right corners). On the other hand, increasing or diminishing both α and ϵ at the same time has less influence on the temperatures.

The tables also show that if the emittance variation is less than the absorptance (upper

ΔT_{max}	$\epsilon \times 1.2$	$\epsilon \times 1.1$	$\epsilon \times 1.05$	$\epsilon \times 1$	$\epsilon \times 0.95$	$\epsilon \times 0.9$	$\epsilon \times 0.8$
$\alpha \times 1.2$	-0.8	5.1	8.3	11.7	15.4	19.3	28.2
$\alpha \times 1.1$	-6.2	-0.5	2.7	6.0	9.6	13.4	22.0
$\alpha \times 1.05$	-9.0	-3.4	-0.3	3.0	6.6	10.3	18.8
$\alpha \times 1$	-11.8	-6.3	-3.2	0.0	3.5	7.2	15.6
$\alpha \times 0.95$	-14.8	-9.3	-6.3	-3.1	0.3	4.0	12.3
$\alpha \times 0.9$	-17.7	-12.4	-9.4	-6.3	-2.9	0.7	8.8
$\alpha \times 0.8$	-23.9	-18.8	-15.9	-12.9	-9.6	-6.1	1.8

Table 4.4: Variation of the maximum temperature [°C] with respect to the nominal case ($\epsilon \times 1$, $\alpha \times 1$) for the 1-node *Body Mounted* configuration in hot 400 km SSO.

ΔT_{min}	$\epsilon \times 1.2$	$\epsilon \times 1.1$	$\epsilon \times 1.05$	$\epsilon \times 1$	$\epsilon \times 0.95$	$\epsilon \times 0.9$	$\epsilon \times 0.8$
$\alpha \times 1.2$	-4.3	1.5	4.6	8.0	11.7	15.6	24.3
$\alpha \times 1.1$	-7.9	-2.3	0.8	4.1	7.7	11.5	20.0
$\alpha \times 1.05$	-9.8	-4.2	-1.2	2.1	5.6	9.4	17.8
$\alpha \times 1$	-11.7	-6.2	-3.2	0.0	3.4	7.2	15.5
$\alpha \times 0.95$	-13.7	-8.3	-5.3	-2.2	1.2	4.9	13.1
$\alpha \times 0.9$	-15.8	-10.5	-7.5	-4.4	-1.1	2.5	10.6
$\alpha \times 0.8$	-20.1	-15.0	-12.1	-9.1	-5.9	-2.4	5.4

Table 4.5: Variation of the minimum temperature [°C] with respect to the nominal case ($\epsilon \times 1$, $\alpha \times 1$) for the 1-node *Body Mounted* configuration in hot 400 km SSO.

triangular part in the tables), the temperature variation is positive, meaning that the spacecraft heats up. This phenomenon results from an increase in the absorbed solar power (α increases) combined to a decrease of the evacuated thermal power induced by a lower ϵ value.

5 | Advanced thermal model

The previous analysis highlighted the influence of the orbit and spacecraft's configuration. However, because of the low number of nodes, it was unable to determine the temperature of the individual components.

The present chapter aims at solving this problem by implementing a more complex thermal model of the satellite, where the major components are represented by their own node. It will give a more representative idea on the temperature of the elements and will allow to take concrete measures if the thermal requirements are not met.

5.1 Geometric mathematical model

5.1.1 Nodal breakdown

The nodal breakdown of the three satellite configurations is presented in the following table. For this advanced thermal model, the lumped parameter method is still used, meaning that the nodes are isothermal. The links between them will be discussed in the TMM.

In this table, some components are referred as *normal to* or *aligned with* a given direction. The first qualifier is used for components attached to the spacecraft's body and the second one is employed for deployable components. For instance, the *Cross* configuration has one solar panel *normal to* $+Z$ and four *aligned with* the directions $+X$, $+Y$, $-X$ and $-Y$.

Component		**Cross**	**Table**	**Body Mounted**
Structure		1000	1000	1000
Shear panels	normal to $+X$	1010	1010	1010
	normal to $+Y$	1020	1020	1020
	normal to $+Z$	1030	1030	1030
	normal to $-X$	1040	1040	1040
	normal to $-Y$	1050	1050	1050
	normal to $-Z$	1060	1060	1060
Deployable panels	aligned with $+X$	2010	n/a	n/a
	aligned with $+Y$	2020	2020	n/a
	aligned with $-X$	2040	n/a	n/a
	aligned with $-Y$	2050	2050	n/a
Solar cells	aligned($^\bullet$)/normal(*) to $+X$	$3010^\bullet$	$3010^\star$	$3010^\star$
	aligned($^\bullet$)/normal(*) to $+Y$	$3020^\bullet$	$3020^\bullet$	$3020^\star$
	normal to $+Z$	3030	n/a	3030
	aligned with $-X$	3040	n/a	n/a
	aligned with $-Y$	3050	3050	n/a
S-band patch antenna		4000	4000	4000
GPS patch antenna		5000	5000	5000

Radiator		6000	6000	6000
PCB stack	EPS	10010	10010	10010
	Batteries	10020	10020	10020
	OBC	10030	10030	10030
	VHF/UHF transceiver	10040	10040	10040
	S-band transceiver	10050	10050	10050
VHF/UHF antenna module		20100	20100	20100
ADCS		30000	30000	30000
Payload		40000	40000	40000

Table 5.1: Nodal breakdown of the advanced thermal model.

5.1.2 Thermo-optical properties

The thermo-optical properties needed to perform the radiative analysis are based on Tab. 4.2. However, in this case, more nodes are considered and additional surface properties have to be defined.

Unlike the basic thermal model, the solar cells are no longer placed directly on their metal support. Instead, an aluminized Kapton film is inserted between the two components, with its aluminized face pointing away from the satellite. This material serves as electric insulation and reflects more solar flux than a bare metal surface. This thin film covers entirely the face supporting the solar cells. The other side is either alodined aluminum in the case of shear panel or bare titanium for deployable panels.

As a reminder, the rails of the structure shall be hard anodized aluminum to prevent cold welding with the P-POD. On the other hand, the shear panels are made of alodined aluminum. This surface finish is used for both the interior and exterior faces. A differentiation between the two sides will be made in the thermal design phase of the next Chapter.

The two patch antennas, the star tracker and the radiator have the same optical properties as the basic thermal model. These are respectively Kapton, blackbody and MAP PCBE white paint.

In the advanced model, the interior of the satellite is also represented. Because of the lack on information from the manufacturers, all the PCBs are assumed to have the same thermo-optical properties. These values are taken from a paper published by NASA in 2014 discussing the optical properties of nanosatellite hardware [50]. It is also guessed that the ADCS, the batteries and the VHF/UHF antenna module have the same surface properties as the PCB.

Finally, the thermo-optical properties are summarized in Tab. 5.2.

5.1.3 Radiative exchange factors

The computation of the radiative coupling is conducted by the MCRT method. Appendix C gives some details about the convergence analysis which was performed to ensure meaningful results.

The calculation made with ESATAN is carried out on a simplified geometry. Fig. 5.1 displays it for the exterior (*Body Mounted* configuration) and interior of the spacecraft. It is seen, for instance, that the batteries are represented by a single box shell. Moreover, some components like the threaded rods supporting the PCBs, the spacers and the cables are not taken into account

Component	Surface finish	α	ϵ	Reference
Solar cell	-	0.72	0.85	[5]
Rails	Al 7075, hard anodized	0.83	0.87	[45]
Shear panels (solar cell side)	1 mil aluminized Kapton	0.38	0.67	[27]
Shear panels (other)	Al 6061, alodined	0.44	0.14	[27]
Deployable panel (solar cell side)	1 mil aluminized Kapton	0.38	0.67	[27]
Deployable panel (other)	Titanium	0.4	0.55	[27]
Radiator	MAP PCBE white paint	0.27	0.88	[46]
Star tracker	blackbody	1	1	
S-band patch antenna	1 mil aluminized Kapton	0.38	0.67	[27]
GPS patch antenna	1 mil aluminized Kapton	0.38	0.67	[27]
PCBs	-	0.65	0.86	[50]
Battery	-	0.65	0.86	[50]
VHF/UHF antenna module	-	0.65	0.86	[50]
ADCS	-	0.65	0.86	[50]
Payload	blackbody	1	1	

Table 5.2: Thermo-optical properties of the detailed model.

for the analysis. These elements would have a negligible impact on the model because of their small surface area. Furthermore, they are not considered as critical as the other ones.

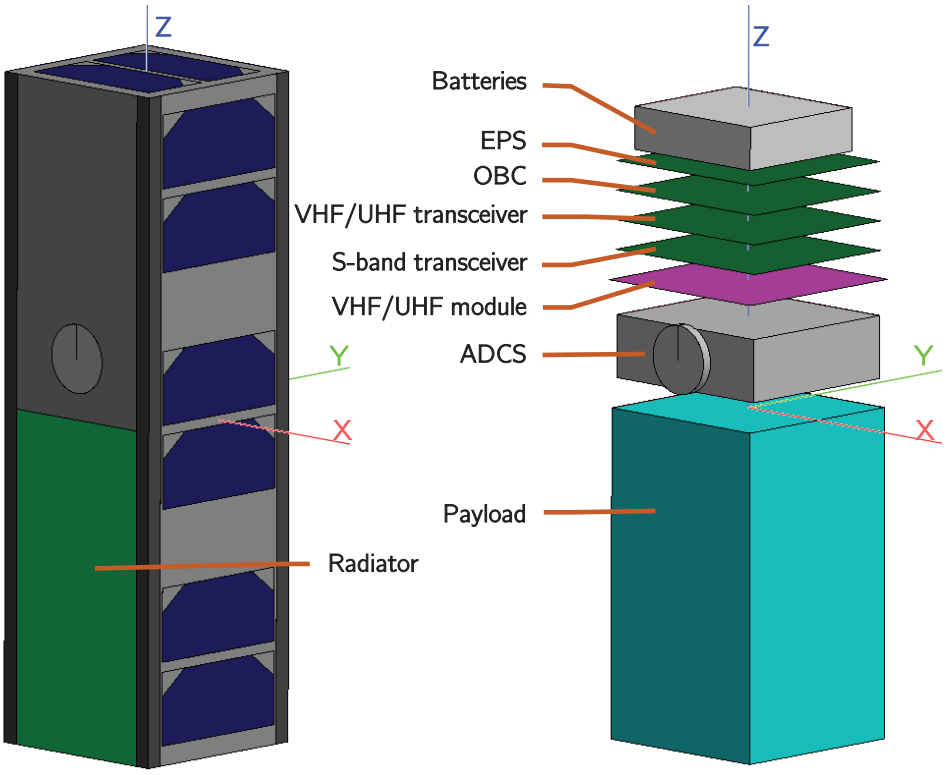

Fig. 5.1: ESATAN representation of the satellite for MCRT.

5.2 Thermal mathematical model

5.2.1 Conductive network

Solar cells to panels

Once again, not a single manufacturer gives all the information necessary to the representation the solar cells' assembly. Hence, data coming from several brands are combined to obtain a realistic solar panel model. The closest match to the 3U deployable panels requested for OUFTI-Next is developed by EXA (Ecuadorian Civilian Space Agency) [4]. They state that the solar cells are placed on a FR4-Tg 180 PCB, which is itself on a 0.25 mm thick titanium scaffold. A polyimide film is also used to cover the space between the cells. However, neither the thickness of the PCB nor reflective film is specified. Endurosat manufactures 3U solar panels [20] with the same PCB material. They specify that it has two internal copper layers 70 μm thick each. Yet another company, GOMSpace [51], says that their circuit board is 1.1 mm thick in total and their Kapton film has a thickness of 1 mil (25 μm).

If the solar cells are fixed to the satellite's body, the assembly is the same, except that the aluminum shear panel is used instead of the titanium one. In that case, it has a thickness of 0.65 mm.

For modeling purposes, all the solar cells on one face (6 for a 3U face and 2 for 1U) are associated to the same node. The rest of the assembly (Kapton, PCB and metal plate) is represented by another node referred as the shear or deployable panel node.

In reality, the conductive heat path from the solar cells to their support is complex to evaluate because the cross section of the two nodes are not identical ($A_{cells} \neq A_{support}$). However, because of the small thickness of the different layers compared to their surface area, the heat flow path can be assumed perpendicular to the interface. The equivalent conductive network is represented in Fig. 5.2.

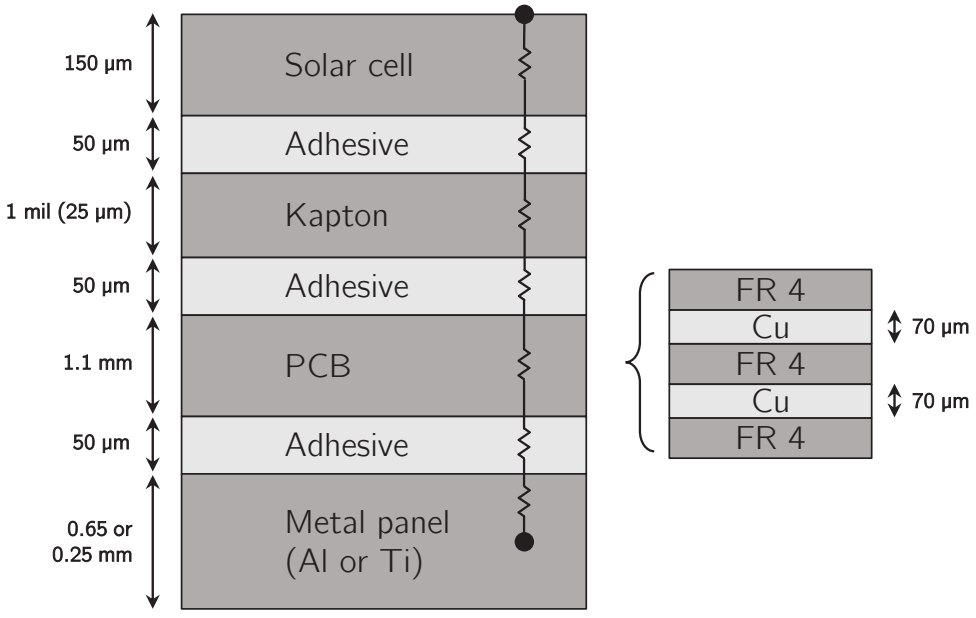

Fig. 5.2: Solar panel assembly and equivalent thermal network.

The adhesive is chosen from the ECSS related to product assurance [52]. This document specifies that non-structural adhesives are used for solar cells assemblies. The basic thermal

model has shown that this component can be very hot. The temperature range is thus a key driver for the selection. The most suited ones are listed in Tab. 5.3.

Name	Thermal range [°C]	Conductivity [W/mK]
D.C. 93500	-65 to 200	0.146
RTV S 691	-180 to 200	0.39
RTV S 695	-180 to 200	0.21
adhesive used	-	0.249

Table 5.3: Non structural adhesive properties for solar panel assembly [52].

Before computing the conductance between the solar cells and the metal panel's node, the through plane resistance of the PCB is needed. It is given by:

$$R_{PCB} = \frac{1}{GL_{PCB}} = \frac{1}{A}\left(2\frac{t_{Cu}}{k_{Cu}} + 3\frac{t_{FR4}}{k_{FR4}}\right),$$

where t_x represents the thickness of material x and k_x is its conductivity. The latter is 2.5 cal/h cm°C (or 0.3 W/mK) for FR4 [53] and 391.2 W/mK for a C10200 copper alloy [27].

Finally, the thermal resistance (or conductance) between the two nodes is computed by the following formula:

$$R_{solar\ cell,\ panel} = \frac{1}{GL_{solar\ cell,\ panel}} = \frac{1}{A}\left(\frac{t_{cell}}{k_{cell}} + 3\frac{t_{adh}}{k_{adh}} + \frac{t_{kapt}}{k_{kapt}} + \frac{0.5\,t_{panel}}{k_{panel}}\right) + R_{PCB}\,.$$

In this relation, the metal plate's thickness is divided by 2 because the node is placed in the middle of the panel. The conductivity values, coming from *Thermal Control Handbook* by D. Gilmore [27], are listed in the following table.

Material	Conductivity [W/mK]
Solar cell (GaAs)	32.9
1 mil Kapton	0.2
Panel (Ti)	7.8
Panel (Al 6061)	180

Table 5.4: Material's conductivity for the solar panels assembly [27].

Shear panels to structure

This link is used to model the interaction between the 6 shear panels attached to the satellite and the structure. The latter is represented by one node placed in the center of the spacecraft. The conductive heat paths are based on the basic thermal model (Fig. 4.10 and Fig. 4.11 for respectively a 1U and a 3U shear panels). This analysis had shown the importance of the contact resistances induced by the bolts ($R_{bolt} = 12.6$ K/W). The structural rails and the ribs are made of hard anodized aluminum alloy Al 7075, having a conductivity k of 121.2 W/mK [27]. They both have a L shape cross section with the same material thickness of 1.2 mm but the rail's width is larger (8.5×8.5 mm) than the rib's (5×5 mm). Their respective cross sections are thus $A_{rail} = 18.96$ mm^2 and $A_{rib} = 10.56$ mm^2. As shown in Fig. 4.10, for a 1U shear panel, the heat travels a length $L_{rib,1}$ in the rib and L_{rail} through the vertical rail. If a 3U panel is considered, only the length $L_{rib,2}$ is crossed (see Fig. 4.11).

Unlike in the basic thermal model, the side panels are no more uniform. They do not all have the same length because of the different inserts (patch antennas, radiator, ...), meaning that they are not bolted on the structure with the same amount of screws. For instance, the $+Y$ face of the *Cross* configuration has a GPS patch antenna attached to it. This module is fixed with 4 screws to the structure, meaning that only 8 are left for the shear panel. On the other hand, the 1U panels always use 4 bolts.

The conductance between the small panels' nodes (in $+Z$ and $-Z$) and the structure's node is computed by:

$$GL_{1U\ panel,struct} = 4\left(\frac{L_{rail}}{A_{rail}k} + \frac{L_{rib,1}}{A_{rib}k} + 2R_{bolt}\right)^{-1}.$$

On the other hand, the conduction for the four other panels follows the relation:

$$GL_{3U\ panel,struct} = n\left(\frac{L_{rib,2}}{A_{rib}k} + 2R_{bolt}\right)^{-1}.$$

In this expression, the parameter n represents the number of screws used to fasten the panels to the structure (i.e. the number of parallel paths for the heat to propagate through). Tab. 5.5 gives the values for the different configurations.

Shear panel		**Insert**	**number of screws for the panel (n)**
Body Mounted	$+X$	none	12
	$+Y$	none	12
	$-X$	S-band and GPS patch	4
	$-Y$	Radiator	6
Cross / Table	$+X$	none	12
	$+Y$	GPS path	8
	$-X$	S-band patch	8
	$-Y$	Radiator	6

Table 5.5: Number of parallel paths used for conduction between the 3U shear panels and the structure.

Inserts to structure

The inserts are the two patch antennas (S-band and GPS) as well as the radiator. They are fixed to the structure like the 3U shear panels and obey the same equation. The antennas are fastened by 4 screws while the radiator uses 6 of them.

Inter PCBs

The PCB stack is represented in Fig. 5.3. The circuit boards are fixed on stainless steel threaded rods and they are kept apart by aluminum spacers. Because of the low conductivity of stainless steel (ten times lower than aluminum) and the loose fit with the boards, the endless screws can be neglected for the conductive analysis.

Additionally to the spacers, the electrical connectors also contribute to the thermal link. According to the PC/104 Specification [54], the connection is ensured by 104 phosphor bronze pins. It is also stated that their plastic housing does not contribute to conduction since is does not touch the overhead PCB.

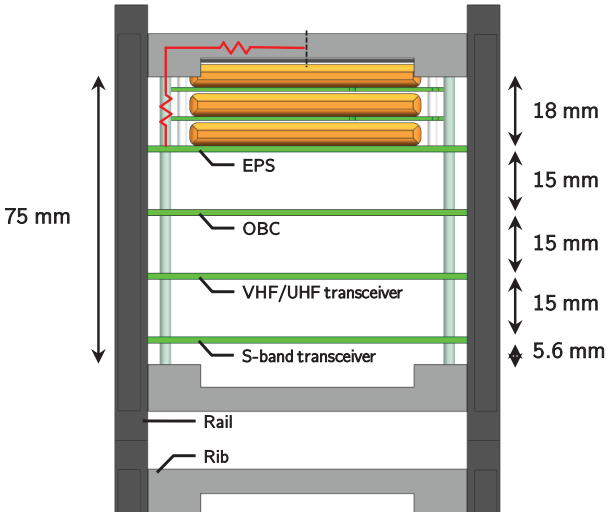

Fig. 5.3: PCB stack.

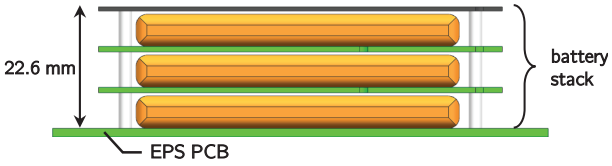

Fig. 5.4: Battery close-up.

The four spacers, made of Al 6061 ($k = 180$ W/mK [27]), have an inner diameter of 3.3 mm and an outer one of 4.3 mm. On the other hand, the phosphor bronze pins have a cross section of 0.5 mm^2 and a thermal conductivity k_{pin} of 75 W/mK [52]. Fig. 5.3 shows that the four circuit boards are 15 mm apart. The electrical connectors, not represented in this simplified drawing, have the same height.

Hence, the conductive link between two adjacent PCBs is given by:

$$GL_{PCB_1,PCB_2} = 4\frac{A_{spacer}k_{Al\,6061}}{L} + 104\frac{A_{pin}k_{pin}}{L}\,.$$

The ratio of the conduction ensured by the spacers over the one through the pins is 1.1. It shows that both elements are equally important.

The interaction between the battery stack and the EPS board is presented in Fig. 5.4. It can be seen that there are three cells and two intermediate PCBs. However, the entire battery stack is modeled by a single node, placed at its center. The link between the batteries' node and the EPS is thus ensured by four aluminum spacers having a height of 11.3 mm.

The problem of the contact resistance between the bottom battery and the EPS arises. Contact phenomena are difficult to evaluate because they depend on many uncertain parameters like the surface roughness of the two elements, the force pressing them together and the potential deformation under this load. None of these parameters are available at this stage of the study. However, because of the use of spacers between the PCB and the battery, it is imagined that the latter is not firmly pressed to the EPS. Indeed, the entire fixation load is carried by the rigid spacers, avoiding the batteries' deformation against the EPS. It results in a weak contact between the two elements and thus a low thermal conduction across the interface. Nonetheless, under vacuum conditions, batteries often expand. This dilation could increase the contact pressure with the EPS board and enhance the conductive heat flow between the two elements. This aspect can be measured during vacuum tests and will have to be carefully studied in future works.

For now, only the four spacers are assumed to contribute to the conductive link between the battery stack and the EPS PCB.

PCB stack to structure

The threaded rods which hold the PCB stack are fixed to the ribs of the structure. Fig. 5.3 shows the conductive heat path between the EPS board and the structure node in red. Because of the additional contact resistance between the rib and the rail, it is assumed that the heat will travel horizontally in the rib instead of going vertically through the rail, to reach the structure's node. A similar path is considered for the bottom S-band transceiver PCB. Before reaching the structure, the heat crosses aluminum spacers of length L (18 mm for the upper board and 5.6 mm for the lower one).

Because of the complicated shape of the rib, a finite element method (FEM) is used to determine its thermal conductivity. Moreover, this component plays a major role in the conductive network of the entire spacecraft since it links all the internal components (PCB stack, VHF/UHF dipole antenna, ADCS and payload) to the structure. Hence, a precise determination of its conductivity by FEM will improve the precision of the model. To do so, a temperature gradient is applied between the two isothermal surfaces of interest (highlighted in bright green in Fig. 5.5) and the power flowing between them is computed. The conductive link is then easily obtained by $GL_{Rib} = Q/\Delta T$. The analysis is conducted with the SamcefField software for a temperature gradient of 10°C.

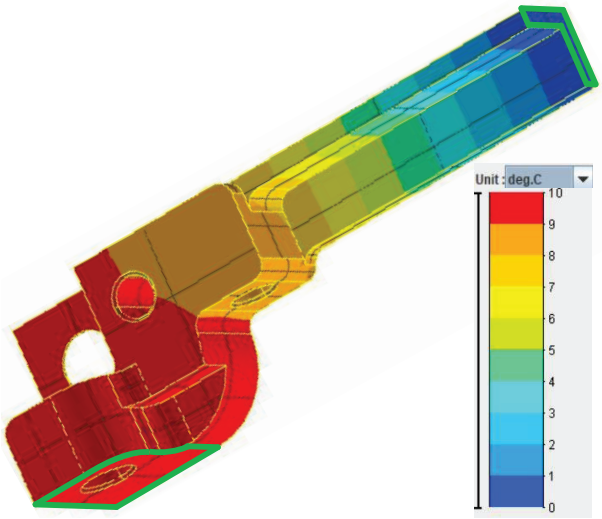

Fig. 5.5: Determination of the half rib's conductivity by FEM.

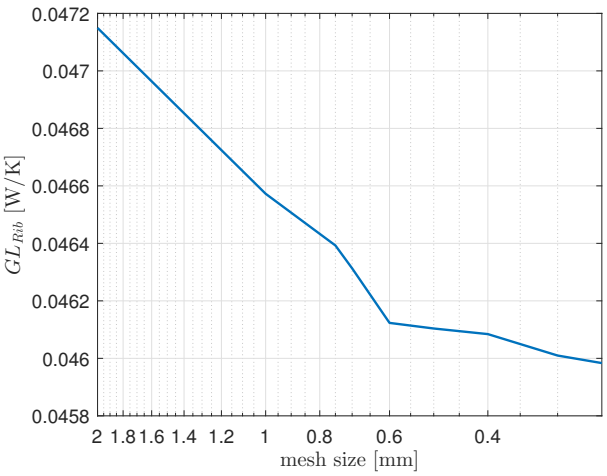

Fig. 5.6: Convergence of the half rib's conductivity with respect to the mesh size.

Because of the intrinsic nature of the process, the results are not exact and a convergence analysis is needed to determine the reliability of the values. Fig 5.6 shows that convergence is reached for a mesh size of 0.6 mm. Hence, the conductive link through the half rib is $GL_{Rib} = 0.0461$ W/K.

Finally, the conductive link from the PCB stack to the strucutre is computed by:

$$GL_{EPS\,or\,Sband,\,struct} = 4\left(\frac{L}{A_{spacer}k_{AL\,6061}} + \frac{1}{GL_{Rib}}\right)^{-1},$$

where the factor 4 represent the four available paths in parallel.

VHF/UHF antenna module and ADCS to structure

As seen in Fig. 1.7, these two components are fixed to the structure in a way similar to the PCB stack (spacers + half rib). The ADCS's spacers are 3 mm high while those of the antenna

module are 4 mm. Another difference comes from the number of fixations. The ADCS has four of them, located on the top. On the other hand, the other element has 8 fixations (4 on top and 4 below), meaning that the factor 4 of the previous formula must be replaced by 8.

Payload

The payload's node is linked to both the structure and the radiator. Several optical systems are considered, each of them having their own fixation mounts. However, none of them have been designed yet. To remain general, it is assumed that conduction occurs through 25 mm high spacers made of the same material as for the PCB stack. The payload is supposed to be fixed to the structure's rib at 8 places (four at the top and four at the bottom). The conductive link is thus:

$$GL_{Payload,\,struct} = 8\left(\frac{L}{A_{spacer}k_{AL\,6061}} + \frac{1}{GL_{Rib}}\right)^{-1}.$$

On the other hand, the link with the radiator has been estimated at 1.61 W/K by the COOL subsystem in [19].

Summary

The different values of the conductive links between the nodes are presented in the table hereafter for the three configurations.

Link	Body Mounted	Cross	Table
Solar cell - Deployable panel	n/a	4.25	4.25
Solar cell - $+X$ shear panel	4.27	n/a	4.27
Solar cell - $+Y$ shear panel	4.27	n/a	n/a
Solar cell - $+Z$ shear panel	1.42	1.42	n/a
Structure - $+X$ shear panel	0.19	0.19	0.19
Structure - $+Y$ shear panel	0.19	0.12	0.12
Structure - $+Z$ shear panel	0.04	0.04	0.04
Structure - $-X$ shear panel	0.06	0.12	0.12
Structure - $-Y$ shear panel	0.09	0.09	0.09
Structure - $-Z$ shear panel	0.04	0.04	0.04
S-band patch antenna - Structure	0.06		
GPS patch antenna - Structure	0.06		
Radiator - Structure	0.09		
EPS - Structure	0.1		
EPS - Batteries	0.38		
EPS - OBC	0.55		
OBC - VHF/UHF transceiver	0.55		
VHF/UHF trans. - S-band trans.	0.55		
S-band trans. - Structure	0.15		
VHF/UHF module - Structure	0.31		
ADCS - Structure	0.16		
Payload - Structure	0.18		
Payload - Radiator	1.61		

Table 5.6: Conductive links [W/K] between the nodes for the three configurations.

5.2.2 Bulk properties

This section reveals the bulk properties such as the mass and the thermal capacitance of the different nodes needed to establish the TMM. Some values are directly provided by the manufactures but other need more thoughts and hypotheses to be made.

The solar cells are made of GaAs for which the manufacturer [5] specifies a weight of 84 mg/cm^2. It results in a total weight of 2.4 g per cell. Their capacitance simply corresponds to the product of the mass and the specific heat of the material.

The 3U ISIS structure [6] is made of Al 7075 and has a total mass (rails, ribs and threaded rods) of 0.304 kg. Its specific heat is obtained from [27] and leads to a capacitance of 292.2 J/K.

The payload consists in the detector, its cooling system and the optical assembly (lenses/mirrors and their mounting supports). At this stage of the design, none of them are clearly defined, making their modelling difficult from a thermal point of view while remaining general. For this reason, the payload's node is assumed to have a mass of 1 kg and a specific heat of 1000 J/kgK.

The last straightforward component is the radiator. It is made of copper alloy C10200 and is 1 mm thick. It covers half of a large face of the satellite.

Shear panels and deployable panels

The metal panels supporting the solar cells are made of titanium if they are deployable and Al 6061 otherwise. The node encompasses all the elements displayed in Fig.5.2 except the solar cell. However, because of the very low thickness of the Kapton foil and of the adhesive layers, they are both neglected for the mass and capacitance computation. Finally, only the metal panel and the PCB remain.

The first step towards the nodal capacitance is the determination of the mass. The PCB is 1.1 mm thick and has two copper layers inside, each of them being 70 μm thick. The PCB's plastic substrate (FR4 fiberglass) has a density of 1850 kg/m^3 [47] while it is 8960 kg/m^3 for copper. The total mass of the PCB is thus

$$m_{PCB} = m_{FR4} + m_{Cu} = 0.96 \cdot 10^{-3} \rho_{FR4} S + 2 \cdot 0.07 \cdot 10^{-3} \rho_{Cu} S \,,$$

where S is its surface, which is the same as the supporting metal panel.

The PCB's specific heat depends on the mass fraction (x) of the two materials, which is given for a component y by $x_y = \frac{m_y}{m_{tot}}$. Its value is 41.4% for the copper and 58.6% for FR4. The general FR4 plastic datasheet provided by *Dielectric Corporation* [47] indicates a specific heat between 1200 and 1400 J/kgK. Without further considerations, the value 1300 J/kgK is retained. On the other hand, the copper's specific heat is 385.2 J/kgK [27]. Finally, the specific heat and capacitance of the solar cells' PCB are given by:

$$\begin{aligned} c_{p,PCB} &= x_{Cu} c_{p,Cu} + x_{FR4} c_{p,FR4} \,, \\ C_{PCB} &= m_{PCB} c_{p,PCB} \,. \end{aligned}$$

In a similar way, the equivalent node's capacitance (metal plate + PCB) is computed by:

$$\begin{aligned} c_{p,eq} &= x_{sup} c_{p,sup} + x_{PCB} c_{p,PCB} \,, \\ C_{eq} &= (m_{sup} + m_{PCB})\, c_{p,eq} \,, \end{aligned}$$

where m_{sup} and $c_{p,sup}$ are the mass and specific heat of the supporting metal plate. This one is made of 0.65 mm thick Al 6061 ($c_p = 961.2$ J/kgK) for fixed solar panels and 0.25 mm titanium ($c_p = 522$ J/kgK) for deployable ones.

In the case of bare shear panels (no solar cells on top), Al 6061 is considered and the capacitance simply corresponds to the product of their mass and specific heat. These panels are 0.65 mm thick and their surface area depends on the number of inserts (patch antennas, radiator, ...).

PCB stack and VHF/UHF antenna module

As a reminder, the circuit boards composing the PCB stack are the EPS, OBC, VHF/UHF transceiver and the S-band transceiver. While nearly all manufacturers provide the masses of these circuit boards, none of them give their specific heat. The masses of these PCBs and of the VHF/UHF antenna module are listed in Tab. 5.7.

Circuit board	Mass [kg]	Reference
EPS	0.086	[9]
OBC	0.076	[13]
VHF/UHF transceiver	0.085	[12]
S-band transceiver	0.09	estimated from [11]
VHF/UHF antenna module	0.085	[14]

Table 5.7: Masses of the PCBs.

Their internal composition is assumed to be 50% in mass of copper and 50% of FR4 fiberglass plastic substrate. This composition is different from the solar cells' PCB because they carry many more surface-mounted components (capacitors, resistors, chips, ...). Their specific heat is thus:

$$c_{p,PCB} = 0.5\, c_{p,Cu} + 0.5\, c_{p,FR4} = 842.6 \text{ J/kgK}\,.$$

On the other hand, the VHF/UHF antenna module encompasses the antenna deployment mechanism which is made in aluminum. Hence, the mass fraction of the components constituting this board is assumed to be 50% Al 6061, 25% Cu and 25% FR4. This results in a specific heat of 901.9 J/kgK.

The lithium-polymer batteries have a mass of 0.35 kg [9] but their thermal capacitance is not specified. It is thus chosen to consider the same value as for the OUFTI-1 nanosatellite [36]. This spacecraft used the same battery technology, for which a value of 1350 J/kgK has been obtained experimentally.

ADCS

According to the manufacturer [15], the ADCS weights 0.4 kg. Once again, the thermal properties are missing and have to be guessed. This component has three reaction wheels made of aluminum and Fig. 1.11 shows that their housing is also metallic. It is thus assumed that the ADCS is made of 70% aluminum in mass and the rest is FR4.

Patch antennas

Both the ClydeSpace S-band patch antenna and the SkyFox Labs GPS patch antenna are 50 g. Their internal composition is estimated to be half copper and half FR4 plastic.

Summary

Finally, the mass and the capacitance of each elements are listed in Tab. 5.8. The total values for the three satellite's configurations are also shown. They simply correspond to the sum of all the components presented in this section. It means that some small elements like the spacers or the cable linking the different systems together are not taken into account for the thermal analysis. Nonetheless, they have a negligible mass and capacitance.

Element	Mass [g]	Capacitance [J/K]
Structure	304	292.20
Shear panel - 3U, no insert	53.6	51.49
Shear panel - 3U, 1 patch antenna insert	38.1	36.65
Shear panel - 3U, 2 patch antennas insert	22.7	21.81
Shear panel - 3U, radiator + star tracker insert	25.3	24.29
Shear panel - 1U, no insert	17.9	17.16
Shear panel - 1U, payload aperture insert	8.9	8.54
Solar cells' supporting plate - 3U, Ti	141.9	115.74
Solar cells' supporting plate - 3U, Al	165.5	154.92
Solar cells' supporting plate - 1U, Al	48.7	45.57
Solar cells - 3U	14.1	4.72
Solar cells - 1U	4.7	1.57
Batteries	350	472.5
EPS	86	72.46
OBC	76	64.04
VHF/UHF transceiver	85	71.62
S-band transceiver	90	75.83
VHF/UHF antenna module	85	76.66
GPS patch antenna	50	42.13
S-band patch antenna	50	42.13
ADCS	400	425.14
Radiator	126.4	48.70
Payload	1000	1000
Body Mounted configuration	**3171.9**	**3104.5**
Cross configuration	**3544.0**	**3370.0**
Table configuration	**3322.4**	**3207.3**

Table 5.8: Masses and capacitances considered for the detailed thermal model.

5.2.3 Internal dissipation

The hot and cold cases definitions are the same as for the basic thermal model (Section 4.1.1 and 4.1.2). It is assumed that there is no internal dissipation during the cold case, while all the power generated by the solar cells is dissipated in the hot case.

Contrarily to the basic model, the interior of the spacecraft is represented. It allows a more realistic division of the heat dissipated by the different modules for the hot case. According to the SYSE subsystem in [2], the distribution follows Tab. 5.9. This table shows the consumption of the satellite for different situations. These numbers are independent of the spacecraft's configuration (*Body Mounted*, *Cross* or *Table*). The *idle* mode corresponds to a constant sun pointing with telemetry communication via UHF. During *acquisition*, scientific images are taken with the MWIR camera. It is thus characterized by a higher consumption of the cooling system needed

to keep the detector's temperature acceptable. In this case, the $-Z$ face of the satellite points nadir. The last situation is the *communication* phase, where VHF and S-band frequencies are extensively used to transmit scientific data to the ground station. It requires the S-band patch antenna to face the Earth.

These numbers include a 20% safety margin and are obtained under the assumption of a Peltier cooling system. It has been established by the COOL subsystem in [19] that this element must be turned on even outside the acquisition phase, consuming 2 W. When the satellite is imaging, the detector must be cooled further down and the Peltier has a consumption peak at 5 W. In the table, the payload line also takes into account the consumption of the visible and MWIR cameras.

	Idle	**Acquisition**	**Communication**
EPS	240 (5%)	240 (3%)	240 (2%)
OBC	480 (9%)	480 (5%)	480 (4%)
VHF/UHF transceiver	588 (11%)	588 (7%)	2628 (20%)
S-band transceiver	0	0	6000 (45%)
ADCS	1868 (36%)	1868 (21%)	1868 (14%)
Payload	2004.8 (39%)	5600 (64%)	2004.8 (15%)
Total consumption	5180.8	8776	13220.8

Table 5.9: Satellite's consumption [mW] in different situations.

In the hot case, the remaining power is dissipated at the solar cells' level. The amount depends on the satellite's electric production and thus on the configuration considered. The power generated during sun pointing, for the hot case ($C_S = 1414$ W/m^2) is listed in Tab. 5.10.

Body Mounted	**Cross**	**Table**
9.27	26.95	18.66

Table 5.10: Power generation [W] in the hot case.

6 | Results and thermal design

This chapter presents the results of the advanced thermal model. The simulations are conducted on the three satellite's configurations and for three different orbits. A distinction is made between the non-operational, acquisition and communication modes. However, the last two events have a short duration (about 5% of the orbit's period) and occur only a few times per day. For these reasons, the non-operational phase is the most representative one and its study will be more detailed. On the other hand, the acquisition and communication modes will be analyzed only for one spacecraft's configuration and orbit. Moreover, a sensitivity of the temperature with respect to the frequency of these events will be conducted.

After pointing the problems with the thermal requirements of the mission, a design optimization will be exposed. Its goal is to implement modifications to the satellite which are as simple as possible and the most effective to bring back the components in their allowable temperature range. A special attention will also be paid to keep the payload as cool as possible during the entire orbit.

6.1 Consistency analysis

Before jumping into the results' analysis of the detailed thermal model, a comparison is made with the basic model implemented in Chapter 4. For the sake of brevity, only one satellite configuration and one orbit are displayed in Fig. 6.1. The figure shows the temperatures of the three sub-assemblies forming the *Cross* configuration (body, deployable solar panels and fixed solar panel). The curves of the detailed model (solid lines) are obtained by averaging the temperatures of all the nodes forming a sub-assembly thanks to the following formula:

$$T_{avg} = \frac{\sum_i T_i C_i}{\sum_i C_i} ,$$

where the index i runs on all the nodes of the sub-assembly and C_i is the capacitance of node i.

It is seen that there is a close match between the two models (maximum temperature difference of 8°C). However, the results are not exactly the same. Some of the discrepancies can be explained by the difference in capacitance between the two models (see Tab. 4.3 and Tab. 5.8). For instance, the node representing the deployable solar panels has a value 17% larger in the detailed model. This results in a more important temperature variation of the basic model. Nonetheless, at the satellite's level, the capacitances are close to each other (3450 J/K for the basic model and 3370 J/K for the detailed one). The temperature differences are also due to changes in the modelling assumptions as the design gets refined. It is the case of the surface finish used between the solar cells. The bare metal surface (alodined aluminum or titanium) used in Chapter 4 has been replaced by a Kapton film. This material ensures a higher solar reflectivity, resulting in a decrease of the absorbed power and in colder solar panels. This modification is also felt on the

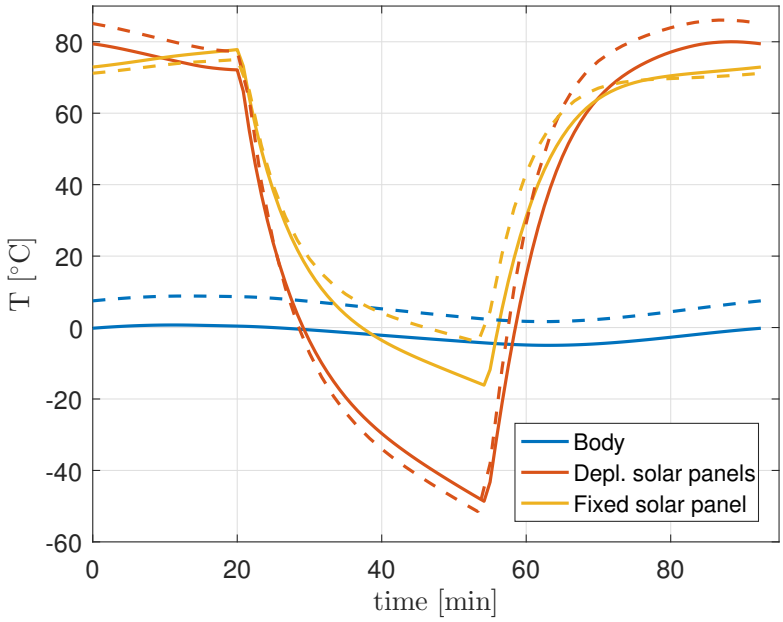

Fig. 6.1: Consistency between the basic model (dashed lines) and the advanced one (solid lines) for the hot case - *Cross* configuration, 400 km SSO.

satellite's body since it is linked radiatively and conductively to the other elements. This results in an overall colder satellite.

6.2 Results of the idle mode

At this stage of the mission, it has been decided by the project team that the *Body Mounted* configuration will most likely be selected for OUFTI-Next. This choice is motivated by its simpler shape. Without deployable mechanisms, their are less risks of failure and the overall cost of the spacecraft is reduced. Moreover, it has been shown by the SYSE subsystem in [2] that this satellite's shape produces enough power to operate safely, while keeping a batteries' depth of discharge below 20%. For those reasons, the *Body Mounted* results will be more detailed than the other ones. Nonetheless, the *Table* and *Cross*' most important results and conclusions will also be presented.

6.2.1 Body Mounted configuration

Solar cells

The solar cells' temperature of the *Body Mounted* configuration is displayed in Fig. 6.2 and Fig. 6.3 for the cold and the hot cases respectively. The solid lines are associated with the solar cells' average temperature, while the dotted and dashed ones correspond to the minimum and maximum temperatures respectively.

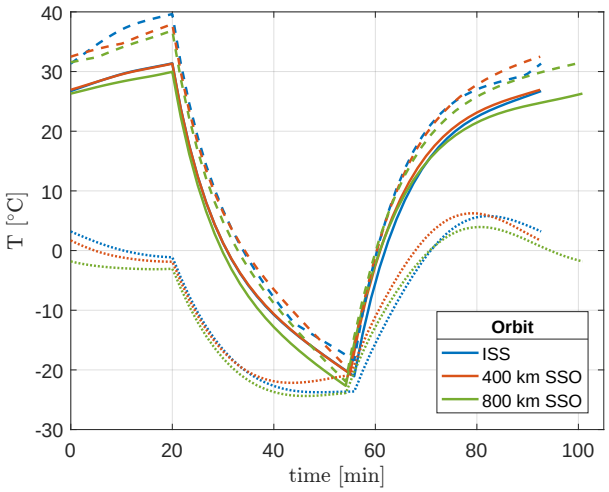

Fig. 6.2: Temperatures of the solar cells *Body Mounted* configuration, cold case.

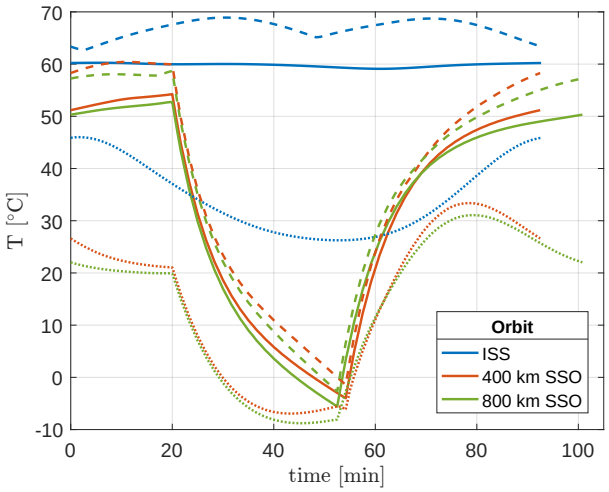

Fig. 6.3: Temperatures of the solar cells *Body Mounted* configuration, hot case.

In the cold case, it is seen that the different orbits give very similar results. It can be explained by the hypothesis that the solar constant does not depend on the altitude for low Earth orbits. The only varying environment parameters are thus the albedo and the Earth IR fluxes. They have two contributions: the direct flux absorbed by the solar cells on the one hand, and the power absorbed by the rest of the satellite and transferred to them by radiative and/or conductive coupling on the other hand. One observes that the higher altitude orbit (800 km SSO) gives the coldest temperatures while the two other ones produce similar results because of their close altitude and eclipse duration.

Fig. 6.3 corresponds to the hot case and show that the temperatures are 20°C to 25°C higher for the two SSO. This increase is the result of the higher environmental parameters and of the electrical dissipation. On the other hand, the ISS orbit results in solar cells 30°C hotter than the cold case. The temperature is also very stable because of the lack of eclipse.

In both thermal cases, the requirements of the solar cells (-55°C to 125°C) are well respected and one sees that there are still margins in case of uncertainties on the model.

Structure and shear panels

The temperature profiles of the structure and shear panels are presented in Fig. 6.4 and Fig. 6.5. The structure is associated with a single node and its temperature is represented by cross markers (+) on a solid line. On the other hand, there are 6 shear panels (and 6 nodes). Hence the graphs show the average, minimum and maximum temperatures following the same line style as the previous section.

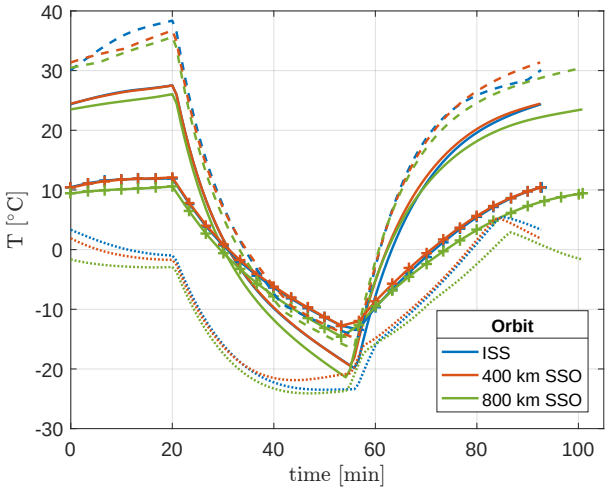

Fig. 6.4: Temperatures of the structure ('+' markers) and shear panels (other curves) *Body Mounted* configuration, cold case.[1]

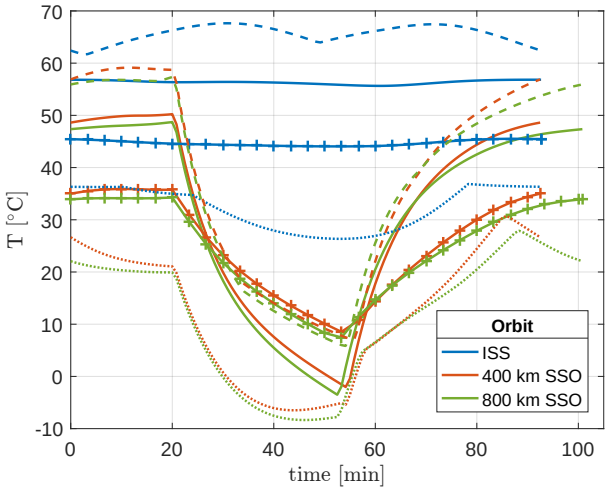

Fig. 6.5: Temperatures of the structure ('+' markers) and shear panels (other curves) *Body Mounted* configuration, hot case.

The two graphs show that the results are compliant with the thermal requirements (from -40°C to 80°C) for both the structure and the shear panels. It is observed that the maximum temperature curves (dashed lines) of the shear panels is very close to the maximum temperature curves of the solar cells. As expected, one concludes that the shear panels subjected the maximum temperature are those supporting the solar cells.

Patch antennas

The S-band and GPS patch antennas have their temperatures displayed in Fig. 6.6 and Fig. 6.7 respectively, where solid lines correspond to the hot case and dashed lines represent the cold one.

It is seen that the two patch antennas have very close temperatures. This result is not surprising since they are both fixed to the same face of the satellite. Moreover, they have the same capacitance. The very small difference (less than 0.1°C) between the two antennas is explained by the approximation of the view factors obtained by ray tracing.

Fig. 6.7 shows that the GPS patch antenna fits its thermal requirements (from -40°C to 45°C). On the other hand, the S-band antenna exceeds its lower allowable limit of -25°C for the two Sun synchronous orbits in the cold case. However, the minimal temperature reached is -27.6°C and it occurs only during a few minutes. For this component, the upper limit is also 45°C and does not cause any problem.

[1] In this figure, the ISS and 400 km SSO curves of the structure ('+' markers) are superimposed.

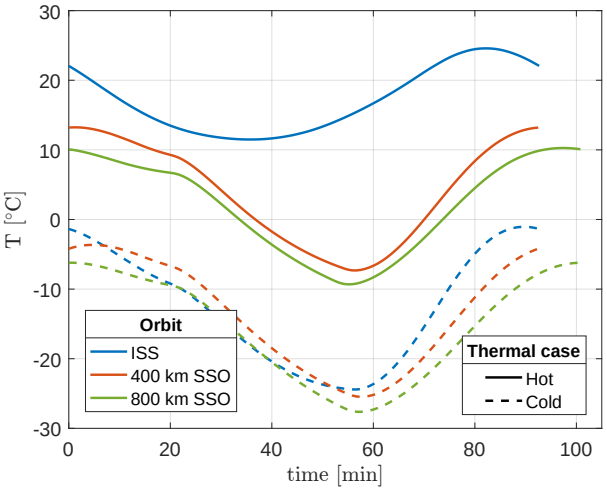

Fig. 6.6: Temperatures of the S-band patch antenna - *Body Mounted* configuration.

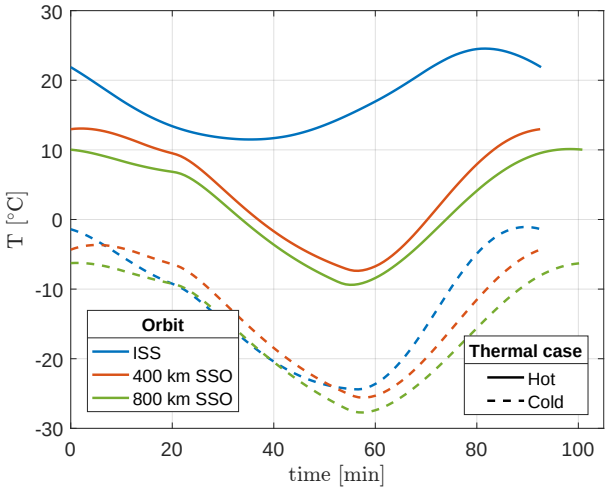

Fig. 6.7: Temperatures of the GPS patch antenna - *Body Mounted* configuration.

Batteries

The batteries' temperature is presented in Fig. 6.8 for the three orbits as well as for the hot and cold cases. Because of their large thermal capacitance, their temperature remains stable along the orbit. Indeed, the curve is flat for the hot ISS orbit while it has an amplitude of approximately 5°C for the other ones.

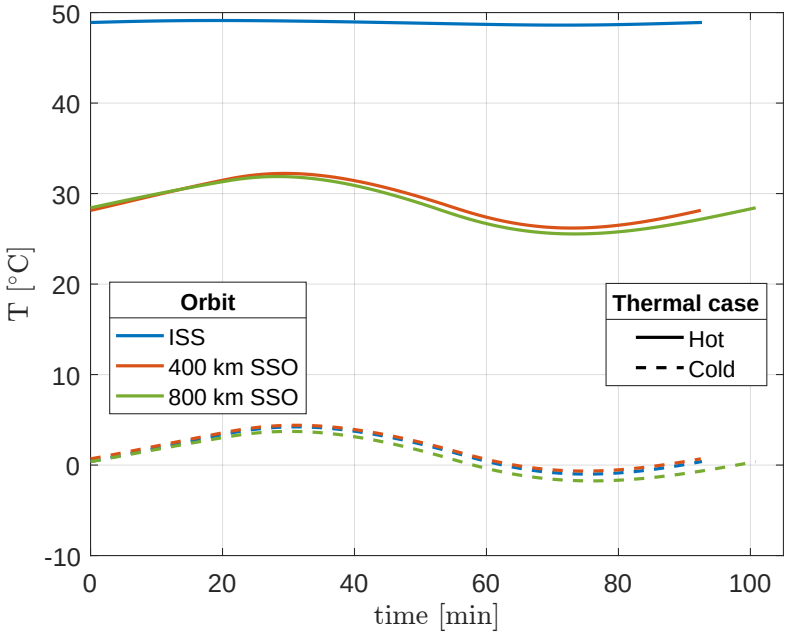

Fig. 6.8: Temperatures of the batteries - *Body Mounted* configuration.

The batteries fit perfectly their thermal requirements if they are discharging (from -20°C to 60°C). However, this is not the case when considering the charging phase (from 0°C to 45°C). For the hot ISS orbit, they are constantly 4°C too hot, while they can be 1.7°C too cold if the 800 km SSO is considered and they have a sub-zero temperature during 40 minutes. Moreover, this situation occurs just after the eclipse period, meaning that the batteries are most likely

charging.

PCB stack, ADCS and VHF/UHF dipole antenna module

For the *Body Mounted* configuration, all these electronic components fit perfectly their thermal requirements. The temperature curves are displayed in Appendix D.1.

Payload

The payload's temperature graph is shown in Fig. 6.9. Even if there is no clear thermal requirement on this component (except for the detector which is studied by the COOL subsystem in [19]), it has been concluded that the colder the payload, the better. This will reduce the additional cooling power needed to reach the working temperature of the detector.

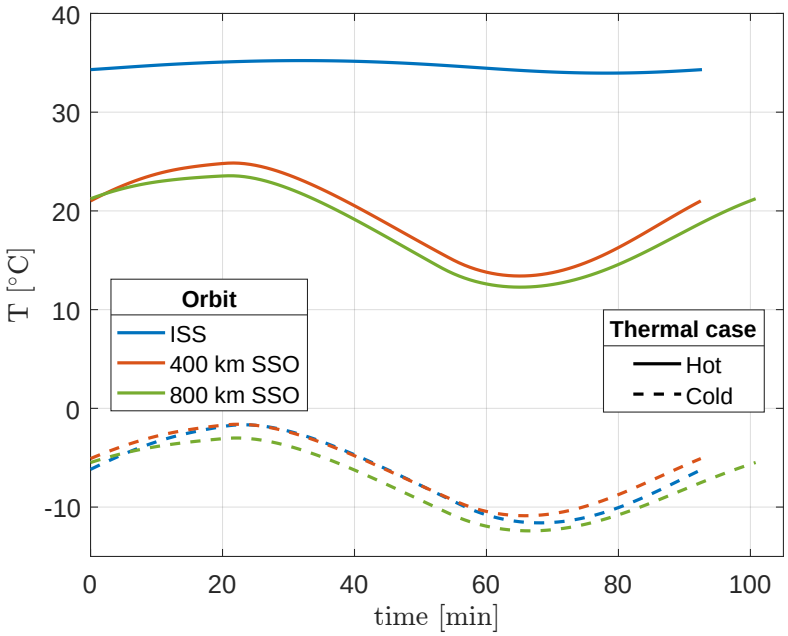

Fig. 6.9: Temperatures of the payload - *Body Mounted* configuration.

For the *Body Mounted* configuration, it is seen that the payload nearly reaches 35°C in the hot ISS orbit. On the other hand, it constantly stays at a sub-zero temperature for the clod cases, with a minimal value of -12.4°C for the 800 km SSO orbit. However, it will be seen later that this satellite's shape is far from being the best one from the payload's point of view.

Thermal interaction of the components

While the previous paragraphs discussed the thermal behaviour of each component individually, it is also interesting to have a more global point of view, on the whole satellite scale. The present analysis focuses on the thermal interaction between the different spacecraft's systems.

The study is conducted with heat flow maps representing the power exchanged between the components. Those maps are generated automatically by a custom MATLAB routine that post-processes the ESATAN results. Because of the cyclic transient nature of the computation, the power exchanged by the elements evolves with time. Hence, the maps can be seen as "snapshots" at a given point in time. To be representative and useful, this moment has to be carefully chosen.

Since the most critical components from the thermal point of view are the batteries and the payload, the heat flow maps are presented at the times leading to their hottest (25 minutes) and coldest (70 minutes) temperatures. Moreover, to remain conservative and concise, only the 800 km SSO and ISS orbits are used for the cold and hot maps respectively because they lead to the most extreme temperatures.

The two maps are displayed in Fig. 6.10 and Fig. 6.11. They represent the thermal balance of each satellite's elements. This concept is ruled by the energy conservation principle and follows Eq. 3.1. This formula expresses that:

$$\begin{aligned}(\textit{External power} + \textit{ Radiative power } + \textit{ Conductive power})_{received} + \textit{ Electrical dissipation} \\ - (\textit{Evacuated power } + \textit{ Radiative power } + \textit{ Conductive power})_{leaving} = \textit{ Stored power}\,.\end{aligned} \tag{6.1}$$

Because of the transient nature of the problem, the thermal power stored in the nodes (thermal inertia) has to be taken into account. This quantity depends on the node's capacitance such that $Q_{i,stored} = C_i \frac{dT_i}{dt}$. Since the computation made by ESATAN is numerical, it depends on a time step and the derivative must be evaluated by the finite difference method. Several schemes have been tested (forward, backward and centered difference) . The last one is second order accurate with respect to the time step and gives the best results. Finally, the temperature derivative at node i and for a time $t^\star$ is approximated by:

$$\frac{dT_i}{dt} \approx \frac{T_i\left(t^\star + h\right) - T_i\left(t^\star - h\right)}{2h}\,,$$

where h is the time step.

In Fig. 6.10 and Fig. 6.11, some boxes (solar cells and shear panels) have several underlying nodes. In this case, the mean temperature and the total stored power are displayed. The blue arrows are used to show power transmitted by conduction while red dashed ones show radiative exchanges. A green arrow is used to model the power evacuated by a component, an orange one represents the absorbed power coming from the environment and a black arrow is associated with the electrical dissipation. Some elements are grouped together in red boxes. Inside these aggregates, it is chosen not to represent the power exchanged by radiation because it is assumed that it cannot be changed by a simple design modification. For instance, the radiative exchanges between boards of the PCB stack will not be modified. Contrarily, the conductive power can be influenced by modifying the spacers' material.

Looking at the two figures, one sees that the thermal balance depicted in Eq. 6.1 is sometimes not strictly respected. Some nodes have a deficit or a surplus of a few milliwatts. This is explained by the computation of the stored power. If the temperature curve is not flat at the time when the derivative is evaluated, an approximation error is made. It explains why the error is larger for the 800 km SSO. Indeed, for the hot ISS orbit, it has been observed previously that the temperatures of the components are stable in time because of the lack of eclipse. In that case, the derivatives are more precise (nearly flat temperature curves) and the thermal balances of Fig. 6.10 are respected for all nodes with a maximum deficit/surplus of 1 mW. Moreover, because of the stable temperature of this orbit, the power stored by the elements is less than for the 800 km SSO. In fact, Fig. 6.10 could be approximated by a steady state analysis.

It must be stressed that the power values written in the figures only correspond to heat. In Fig. 6.10, it means that the external power received by the solar cells (orange dashed arrow) only corresponds to the environmental absorbed power (solar, Earth IR and albedo) that is transformed into heat and does not contain the part which is transformed into electricity by the solar cells (Q_{elec}). However, this Q_{elec} is taken into account for the components' electrical dissipation (black arrows). Indeed, a part of it corresponds to the power consumed by the

spacecraft ($Q_{cons} = 5.18$ W distributed between the EPS, OBC, VHF/UHF transceiver, ADCS and payload). The remaining $Q_{elec} - Q_{cons}$ is dissipated at the solar cells' level.

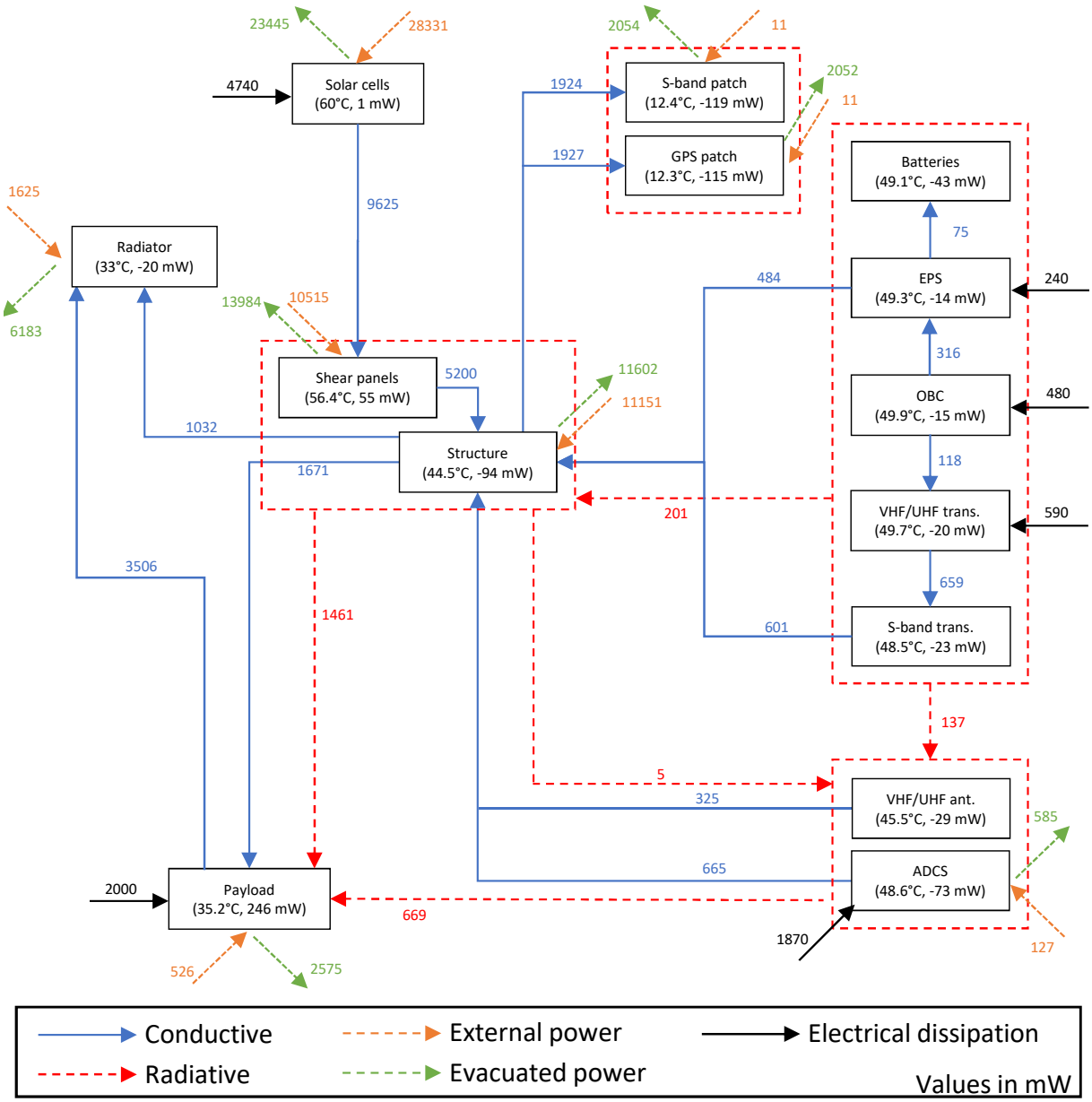

Fig. 6.10: Heat flow map of the *Body Mounted* configuration for the ISS hot case orbit at $t = 25$ min.

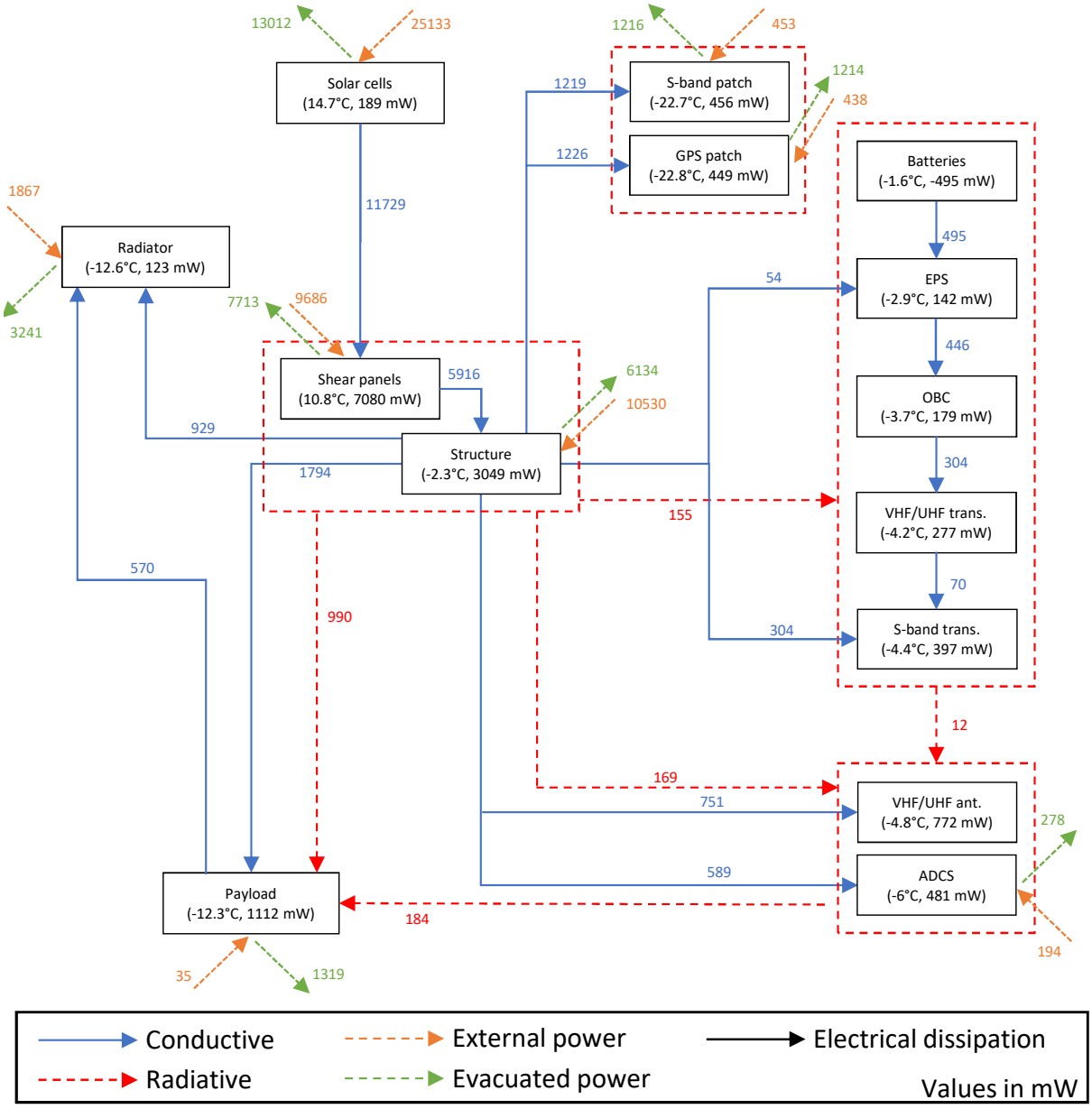

Fig. 6.11: Heat flow map of the *Body Mounted* configuration for the 800 km SSO cold case orbit at $t = 70$ min.

The two diagrams lead to the following observations:

- The solar cells are the most exchanging components. They receive and reject from the environment the largest amount of power. Moreover, they transmit a considerable quantity by conduction to the shear panels. It results from the large contact surface between the two elements and also from the low capacitance of the cells.
- The environmental power absorbed by the radiator is 1.6 W for the hot case and 1.9 W for the cold one. These values are not negligible compared to the other fluxes received by this component. Ideally, this value should be as small as possible in order to avoid heating the payload from the radiator. A solution could be to change the radiator's coating to reduce the power absorption. However, the present surface finish has been chosen by the COOL subsystem in [19] and it is decided to not modify it here. An effective but costly and complicated alternative would be to develop a heat shield to stop the incoming albedo and Earth IR fluxes. Unfortunately, this is beyond the scope of this thesis.
- 62% of the convective flux received by the radiator comes from the structure in the cold case (23% in the hot case). It means that the radiator is heated up by this power flow. Hence, it makes it less effective to cool down the payload. The conductive link between the radiator and the structure will be investigated in the design phase.
- Similarly to the radiator, a large part of the power received by the payload comes from its conductive link with the structure (44% in the hot case and 60% in the other one). This link will also have to be investigated.
- The payload is also heated by radiative fluxes coming from the other spacecraft's components. Their impact will have to be reduced in order to keep the optics and detector as cold as possible.
- In the hot case, the heat flows from the PCB stack to the structure while it is the opposite in the cold case. Because of the low temperature of the batteries (they are outside their allowable range if they are charging) for the cold case, increasing the radiative exchange from the structure and shear panels with a higher emissivity coating seems a good idea. However, in the hot case, the batteries are already too hot if they are charging. This problem needs further investigation.
- Still for the batteries, it is seen that reducing the conductive link with the EPS board could be beneficial in both hot and cold cases.

Fig. 6.12 and Fig. 6.13 show the thermal balance for the payload during the entire orbit. In these figures, negative values correspond to thermal power leaving the payload, while positive ones refer to heat entering the component. It is seen that the two figures are compliant with the heat maps presented earlier. The thermal balance corresponding to Eq. 6.1 is illustrated by a black dashed line. The eclipse period is also represented by a light grey zone. These figures have the advantage to show the time dependence of the power exchanges. In Fig. 6.13, for instance, it is observed that at around 80 minutes, power flows from the radiator to the payload. It means that during this time, the payload is heated up by this exchange. Fortunately, this only happens during a few minutes and the radiator fulfills its role by extracting heat from the payload during the majority of the orbit.

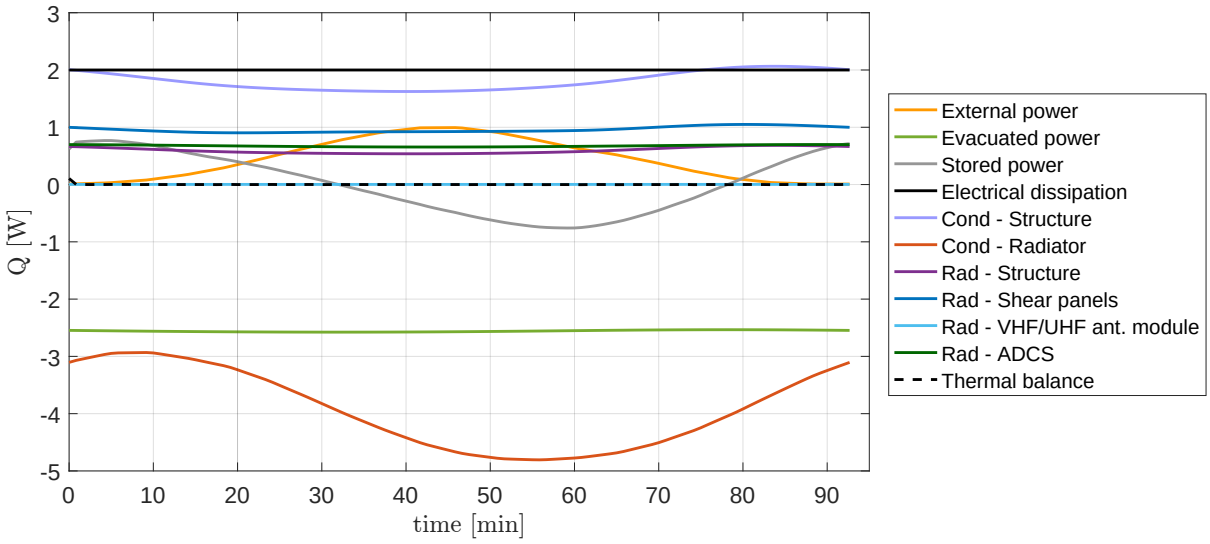

Fig. 6.12: Thermal balance for the payload of the *Body Mounted* configuration - hot case, ISS orbit.

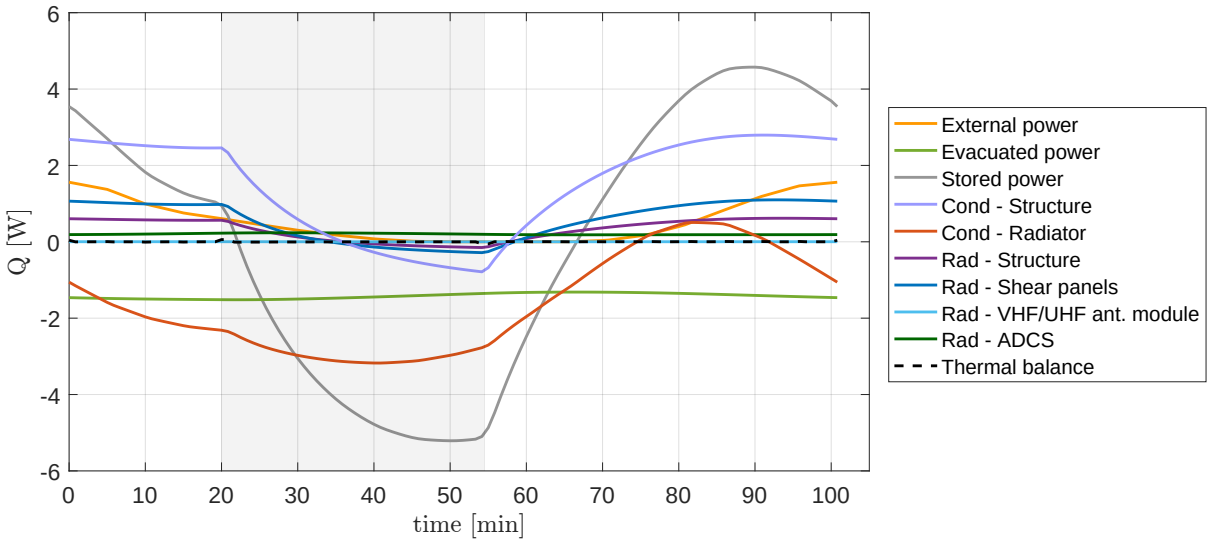

Fig. 6.13: Thermal balance for the payload of the *Body Mounted* configuration - cold case, 800 km SSO.

6.2.2 Cross configuration

This section presents the results of the *Cross* configuration. As stated previously, they are less detailed because this satellite's shape is less likely to be selected for the OUFTI-Next demonstrator. Hence, only the components which do not fulfill their requirements are exposed. Nonetheless, the other ones have their temperature curves represented in Appendix D.2.

Structure, shear panels and deployable panels

The shear panels' temperature is displayed in Fig. 6.14. The continuous curves correspond to their mean temperature, while the dotted and dashed ones represent their minimum and maximum temperatures respectively. On the other hand, Fig. 6.15 is dedicated to the satellite's

structure ('+'markers) and deployable panels. Even if there are several of these panels, it is chosen to represent only their mean temperature curves. Because the deployable panels are oriented the same way and are identical, they have very similar temperatures. In fact, the minimum and maximum curves would be separated only by a fraction of degree. Only the cold cases are displayed here because the hot ones fit the requirements.

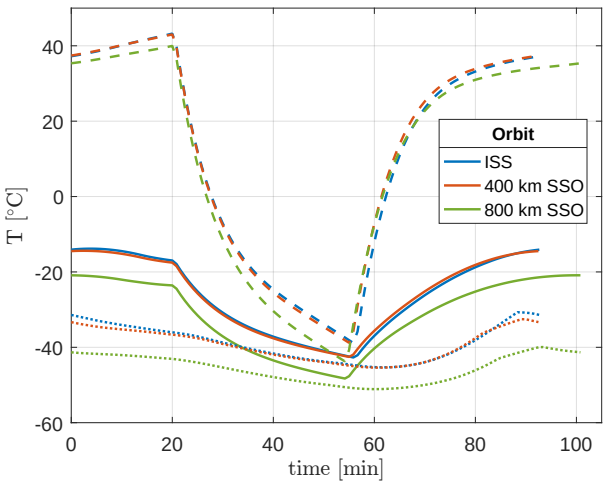

Fig. 6.14: Temperatures of the shear panels *Cross* configuration, cold case.

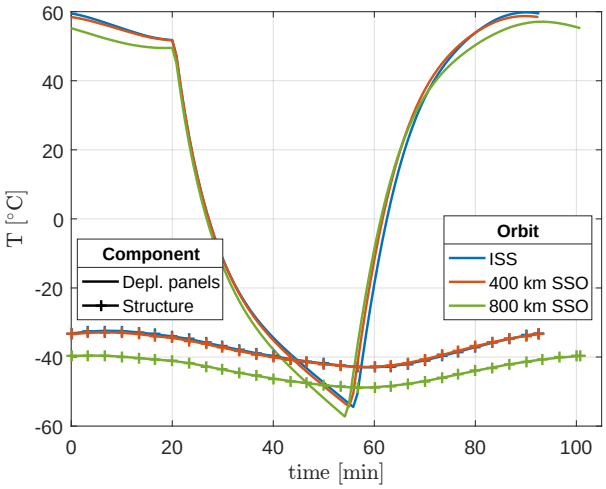

Fig. 6.15: Temperatures of the structure and deployable panels - *Cross* configuration, cold case.

Comparing the two figures to the components' thermal requirements (from -40°C to 80°C), it is seen that they are not always compliant with the acceptable range. In fact, some of them (minimum curve of the shear panels for the 800 km SSO and structure for the same orbit) are outside this range during the entire orbit.

Nonetheless, the manufacturer does not explain the need for a thermal restriction at -40°C for these elements. Indeed, the panels and structure do not contain electronic component and aluminum conserves its mechanical properties at low temperature. According to *Total Materia* [55], aluminum has a 10% loss in yield strength between room temperature and -195°C. Therefore the remaining explanation for such a restriction could be in the material expansion under temperature gradient and more specifically alignment problems. For instance the structure shows a temperature difference of approximately 40°C between the hot and cold cases. With a coefficient of thermal expansion for aluminum of $23 \cdot 10^{-6}$ m/mK, it results in a dilation of 310 μm over its total length (34 cm). In the case of the deployable panels, Fig. 6.15 shows a maximum temperature difference of 110°C during the orbit. With a coefficient of thermal expansion of $8.6 \cdot 10^{-6}$ m/mK for titanium, it results in a dilation of 322 mum over the entire deployable panels' length. The importance of these phenomena should be addressed in future works.

Patch antennas

It is observed in Fig. 6.16 and Fig. 6.17 that the upper limit of both S-band and GPS patch antennas (45°C) is never reached. On the other hand, the lower bound of the S-band antenna (-25°C) is exceeded for the two Sun synchronous orbits in the hot case. However, this component is out of limit only during 20 minutes in the high altitude SSO while the temperature stays close to the requirements for the other orbit.

Nonetheless, things get worse for the cold case. The S-band patch antenna stays constantly

below -30°C. Even if these results are obtained for the idle mode, and thus the S-band antenna is not used, it is expected that this situation will persist during the communication mode and the problem will have to be addressed.

The lower limit of the GPS patch antenna (-40°C) is crossed by the *Cross* configuration for all orbits in the cold case. The worst one is the 800 km SSO, where it stays below the threshold during the entire orbit because the albedo and Earth IR fluxes are lower.

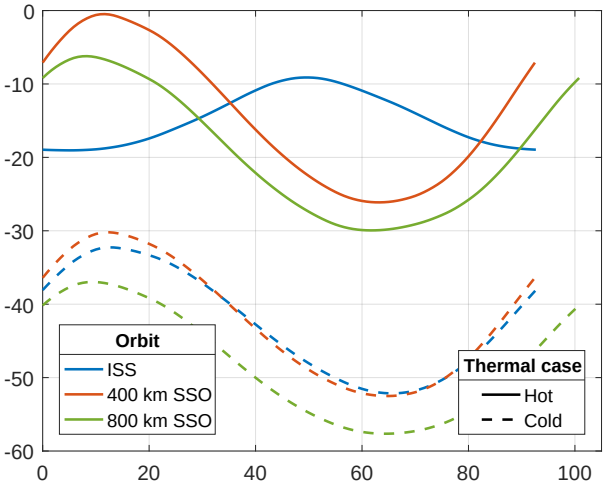

Fig. 6.16: Temperatures of the S-band patch antenna - *Cross* configuration.

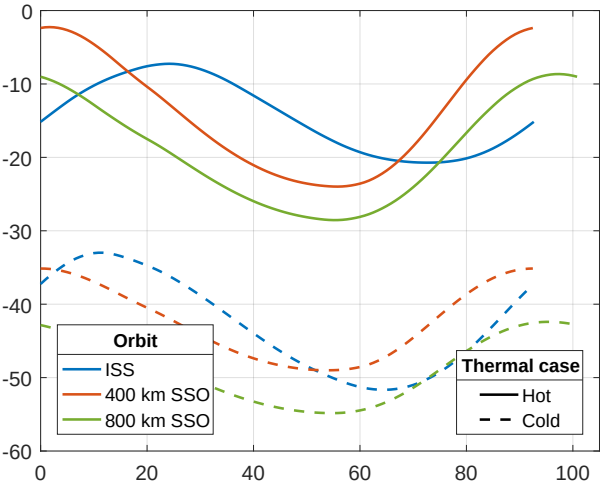

Fig. 6.17: Temperatures of the GPS patch antenna - *Cross* configuration.

Electronic components

The PCB stack's temperature curves are presented in Fig. 6.18 for the cold case only because the hot one fits the thermal requirements. It is seen that only the S-band transceiver PCB is compliant with its allowable thermal range (-40°C to 60°C) if the 400 km SSO or ISS orbits are used. All the other boards are out of bound during the entire orbit period. This graph also illustrates the gradient of temperature across the stack. One sees that it follows the position of the elements. The top board (EPS) is the hottest one and the bottom board (S-band transceiver) is the coldest one. It illustrates the proximity of the EPS with the small 1U solar panel of the *Cross* configuration.

Fig. 6.19 shows the batteries' temperature for both hot and cold cases. It is observed that only the ISS and 400 km SSO lead to compliant results for the charging batteries in the hot case. If they are discharging, the lower limit of the acceptable thermal range drops to -20°C and the hot 800 km SSO becomes viable. However, all the cold orbits produce too cold results for both batteries operating modes. The lowest one is achieved by the 800 km SSO, where the temperature drops to -43°C.

The temperature of the VHF/UHF dipole antenna module is displayed in Fig. 6.20. This component allows a range from -20°C to 60°C. The figure shows that all the cold orbits lead to temperatures inferior to the lower bound of the allowable thermal range. One sees that the components are at least 12°C too cold and that the situation lasts the entire orbit period. The worst case occurs for the 800 km SSO, where the antenna module nearly reaches -50°C.

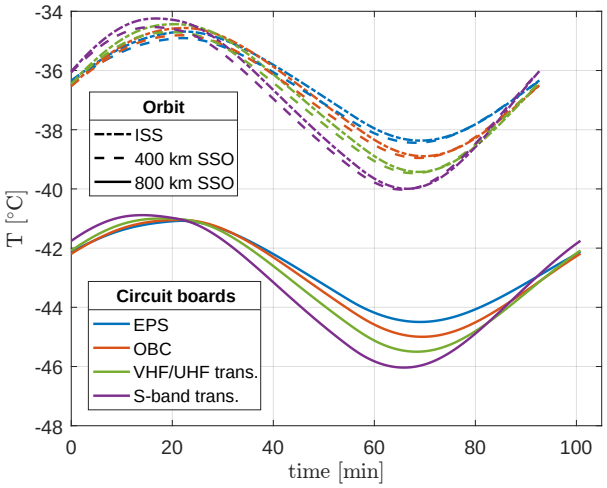

Fig. 6.18: Temperatures of PCB stack *Cross* configuration, cold case.

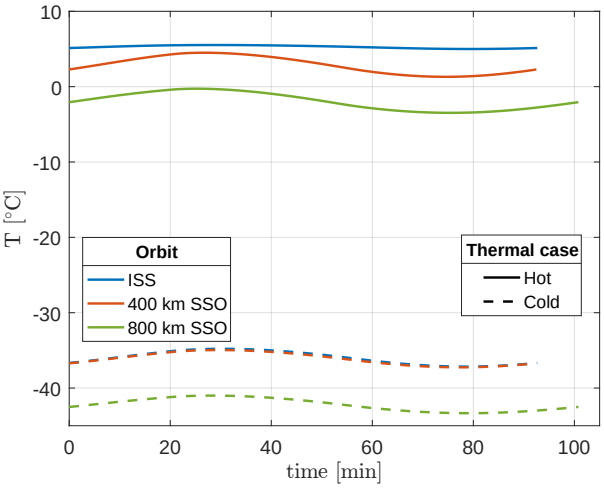

Fig. 6.19: Temperatures of the batteries *Cross* configuration.

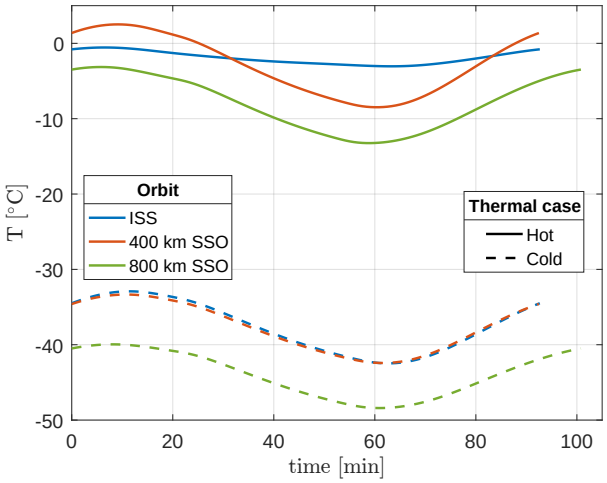

Fig. 6.20: Temperature of the VHF/UHF dipole antenna module *Cross* configuration.

Payload

As it can be seen in Fig. 6.21, the payload has a sub-zero temperature during the entire orbit in both hot and cold cases. Compared to the *Body Mounted* configuration, one observes that it is approximately 35°C colder in the hot case, while the gap reaches 40°C for the cold case. These low temperatures are achieved thanks to the deployable solar panels that hide the spacecraft's body from the direct sunlight. It can thus be logically deduced that the *Cross* configuration is better from the payload's point of view.

Thermal interaction of the components

The last thing to analyze for the *Cross* configuration is the heat flow map. This map illustrates how the thermal power is exchanged between the different satellite's components. The previous paragraphs have shown that the main problem of this spacecraft's shape is the very low temperature to which the electronic is exposed during the orbit. This is the reason why only the

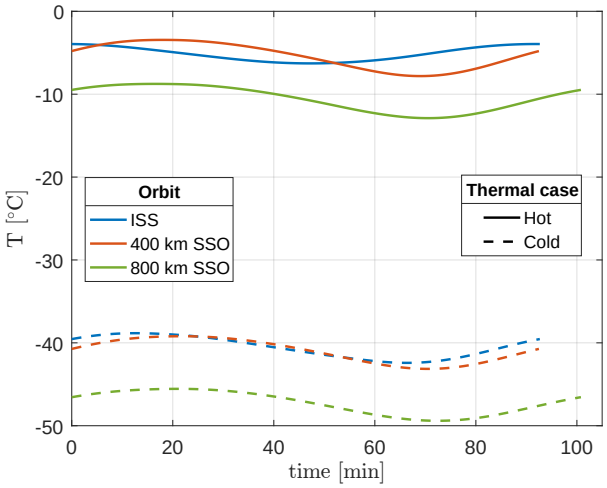

Fig. 6.21: Temperature of the payload
Cross configuration.

map of the worst orbit is produced: the 800 km cold SSO at 65 minutes.

It is seen in Fig. 6.22 that heat leaves conductively the PCB stack via the EPS and S-band transceiver boards. It could be interesting to modify the spacers which link them to the structure in order to reduce this heat exchange and thus heat up the circuit boards. One could also improve the radiative heat exchange between the shear panels and the PCB stack by modifying the surface coating. Another solution would be to link conductively (thermal strap) the small shear panel supporting the solar cells to the batteries. However, because of the very low temperature of the PCBs, it is expected that passive solutions will not be enough to reach a temperature expected by the requirements. For instance, the batteries would have to be at least 43°C hotter to fit the allowable thermal range if they are charging.

For the payload, the figure shows that the heat coming from the other components is small compared to the thermal power going to the radiator (262 mW received and 1108 mW leaving the payload for the radiator). Hence, it is assumed that changing the conductive link to the structure or the radiative one will not have appreciable effects on the payload's temperature.

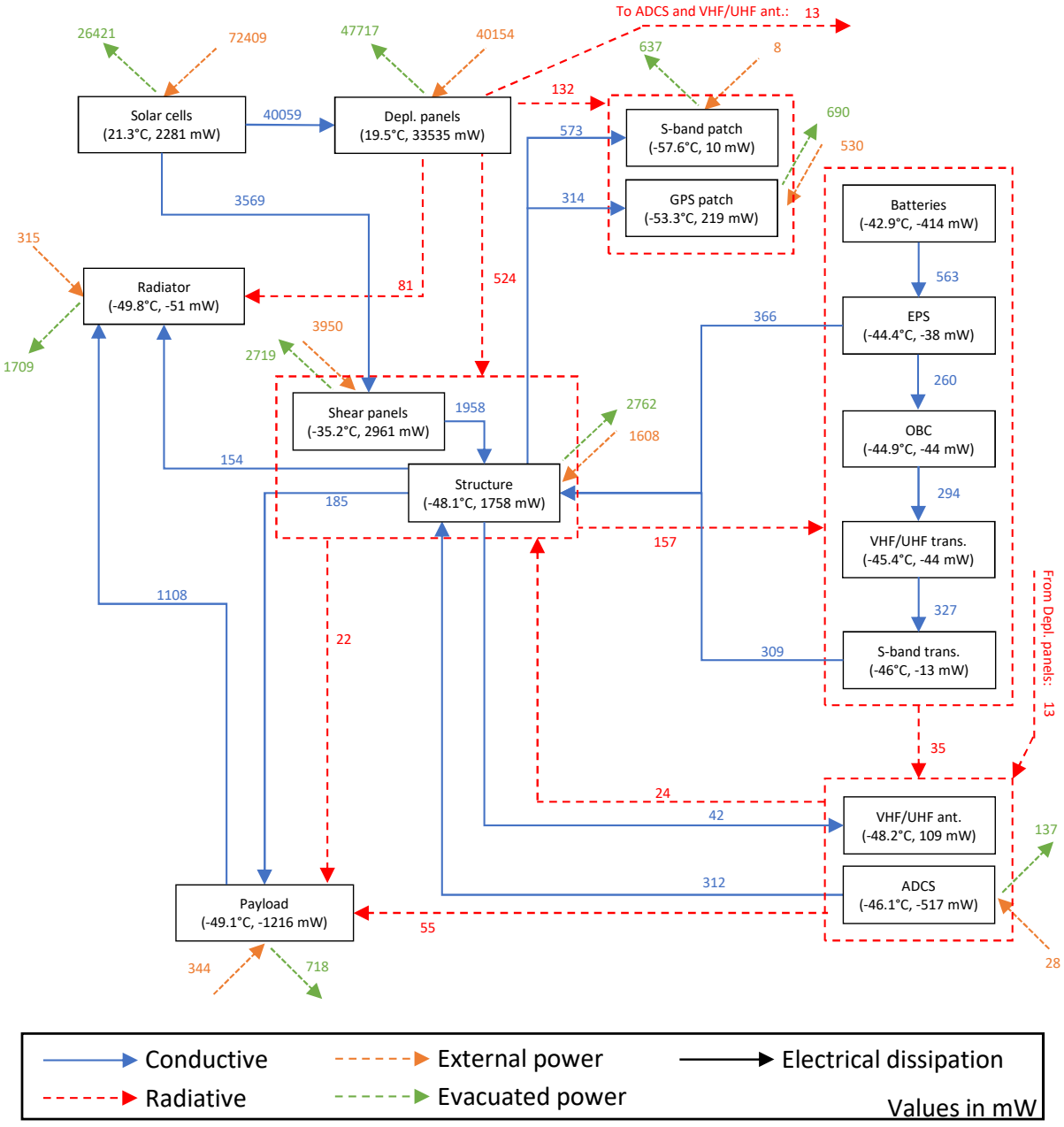

Fig. 6.22: Heat flow map of the *Cross* configuration for the 800 km SSO cold case at $t = 65$ min.

6.2.3 Table configuration

The last satellite's shape to analyze is the *Table* configuration. Like for the *Cross*, it will be less detailed than the *Body Mounted* configuration, only important results are shown here. However, additional temperature curves are displayed in Appendix D.3.

Patch antennas

The two patch antennas are displayed in Fig. 6.23 and Fig. 6.24 for both hot and cold cases. It is seen that the GPS antenna fulfills perfectly its thermal requirements (from -40°C to 54°C), while the S-band patch is a few degrees too cold for the three cold orbits. However, the temperature remains very close to the lower limit of -25°C (minimum temperature for the 800 km SSO: -27.3°C and -25.4°C for the other two orbits). Moreover, these results are obtained for the idle mode, where the S-band antenna is not supposed to be used.

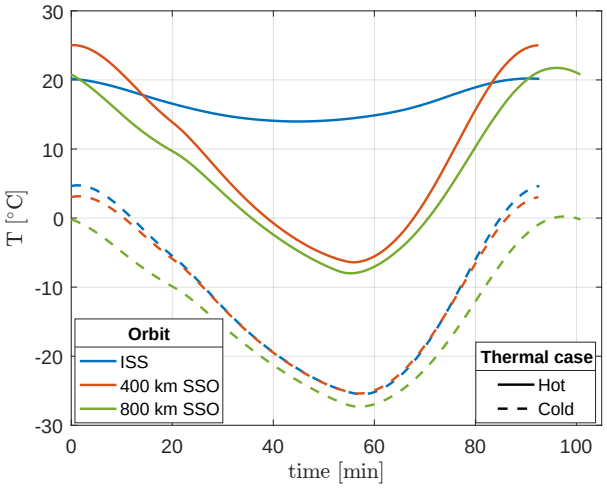

Fig. 6.23: Temperatures of the S-band patch antenna - *Table* configuration.

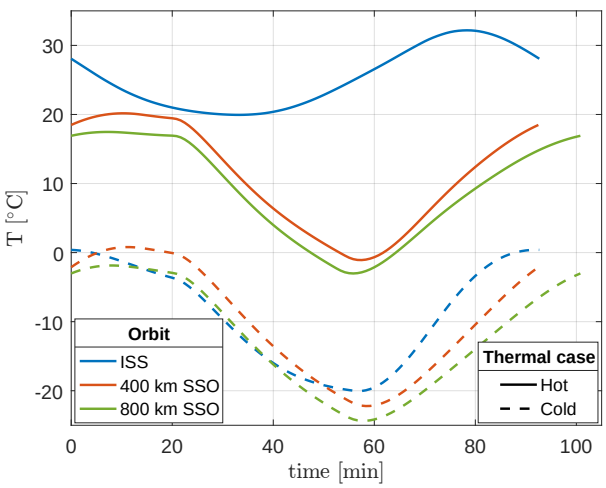

Fig. 6.24: Temperatures of the GPS patch antenna - *Table* configuration.

Batteries

The batteries' temperature profile is illustrated in Fig. 6.25. One observes that the *Table* configuration lead to acceptable thermal loads for these components if the discharging requirement is selected (from -20°C to 60°C). On the other hand, the batteries are constantly 5°C too hot for the charging phase when the satellite has an ISS orbit (hot case). The lower bound of this thermal requirement can also be crossed if the high altitude Sun synchronous orbit is considered. In this case, they reach a minimum temperature of -1.4°C.

Payload

The temperature of the payload is displayed in Fig. 6.26 for the *Table* configuration. It is seen that the values are similar to the *Body Mounted* satellite shape, with temperature ranging between -10°C and 40°C. This similarity is explained by the fact that both satellites have solar cells on at least one of their large shear panels. These panels get heated by conduction (solar cell - shear panels link). Then, heat is transmitted radiatively, inside the spacecraft, from the panels to the detector and to the optic assembly.

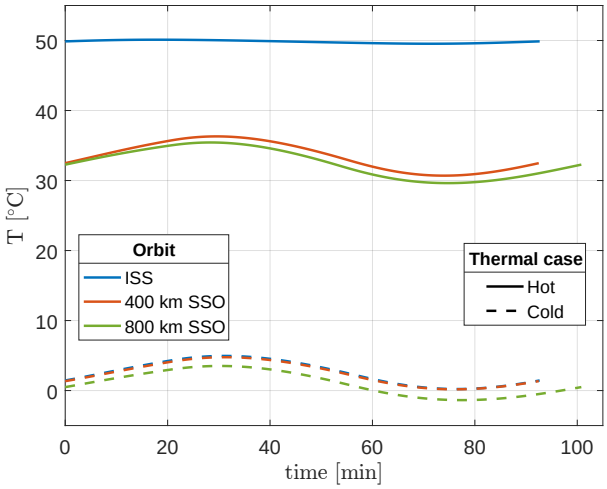

Fig. 6.25: Temperature of the batteries
Table configuration.

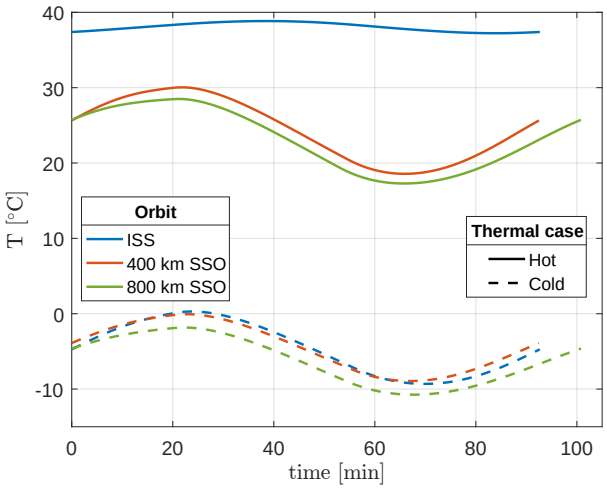

Fig. 6.26: Temperature of the payload
Table configuration.

6.2.4 Summary

Fig. 6.27 to Fig. 6.29 show the global thermal range of all the elements of the satellite for the three orbits, for the idle mode. Contrarily to the curves presented earlier in the chapter, these figures give a clear view of the thermal amplitude to which the components are subjected to. However, since they display only the minimum and maximum temperatures, the time scale is lost. In these figures, the thermal requirements of the different parts are represented by black rectangles. Regarding the batteries, an additional dark grey zone corresponds to the allowable temperature in discharge. Some components like the radiator and the payload do not have a clear requirement on their temperature. They are thus associated to a light grey horizontal bars. Lastly, the cold orbits are illustrated by blue colors and the hot ones by red/yellow shades.

In all situations, for a given satellite's shape, it is seen that the cold cases give similar temperatures while the differences between the hot orbits are more important. It is observed that the smallest temperature variation occurs for the ISS orbit due to the lack of eclipse. In

addition, this orbit also leads to the highest temperatures.

Fig. 6.27 and Fig. 6.29 show that the *Body Mounted* and *Table* configurations give approximately the same results. They both respect the majority of the components' thermal requirements. In fact, only the batteries can be out of bounds if the charging phase is considered. It is seen that the three cold orbits of the *Body Mounted* configurations give temperatures which are a few degrees too cold, while this is the case only for the 800 km SSO if the *Table* is considered. On the other hand the upper limit of the charging batteries is exceeded by both spacecraft's shapes for the hot ISS orbit. The two configurations are attractive from the platform point of view. However, they lead to high temperatures for the payload.

The reversed situation occurs for the *Cross* configuration (Fig. 6.28), where the payload remains cold (between -50°C and -5°C depending on the orbit) while the platform is mostly out of bounds. If the hot cases are considered, it is seen that the temperatures are acceptable from the components' point of view except for the hot 800 km SSO. This orbit can lead to temperatures below the lower limit for the S-band patch antenna and for the charging batteries.

The picture is even worst for the cold orbits. In fact, the S-band patch antenna, the batteries, the EPS, the OBC, the VHF/UHF transceiver and the dipole antenna are constantly too cold to operate safely. For instance, these orbits can lead to temperatures up to 45°C below the requirements if the charging batteries are considered. However, the *Cross* configuration is also the one producing the largest amount of power (all the shapes consume the same amount). Hence, an active solution (e.g. heaters) to keep the platform in its correct thermal range could be considered.

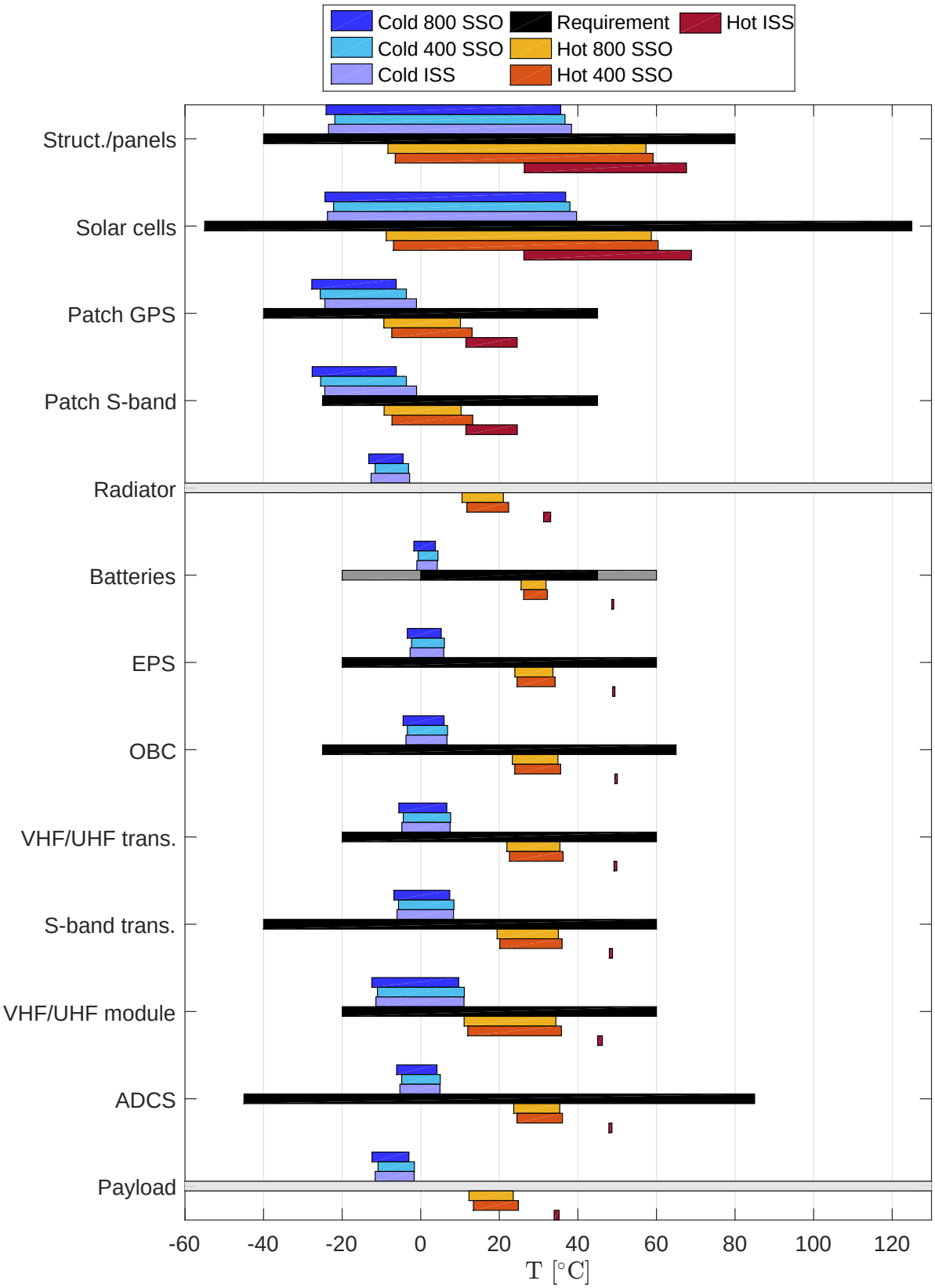

Fig. 6.27: Temperature of the *Body Mounted* configuration.

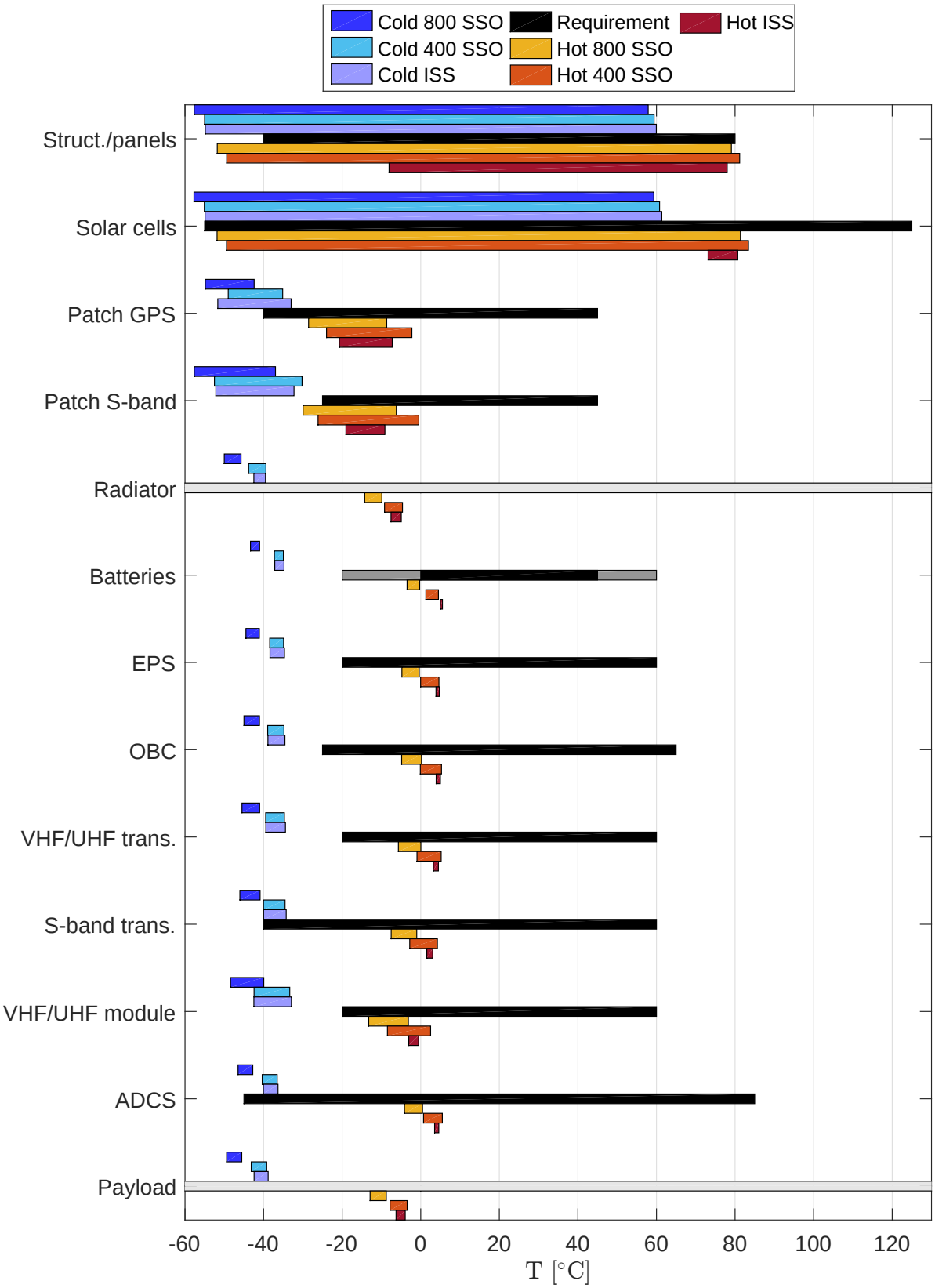

Fig. 6.28: Temperature of the *Cross* configuration.

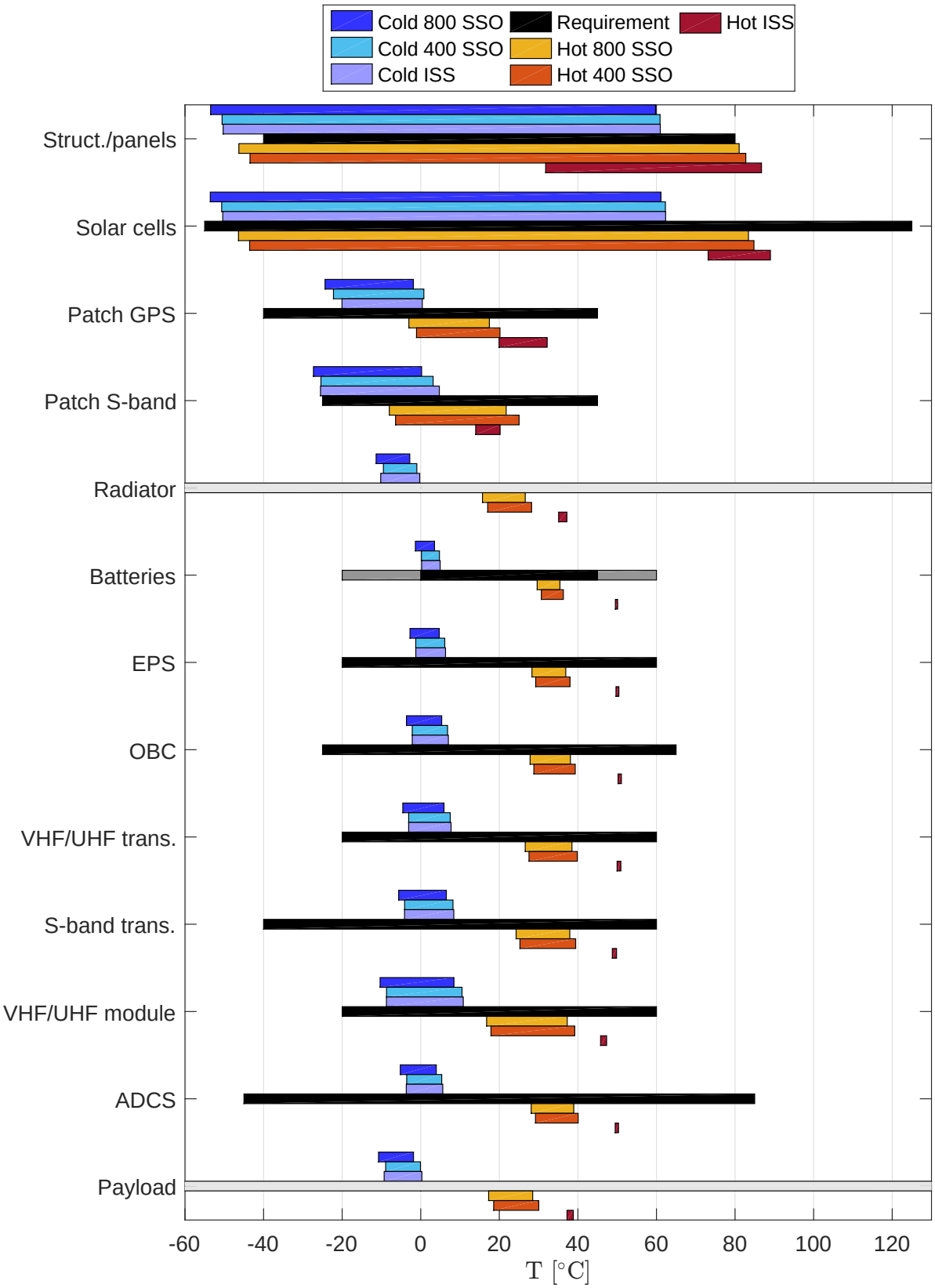

Fig. 6.29: Temperature of the *Table* configuration.

6.3 Operational modes

This section deals with the influence of the operational modes (acquisition and communication) on the thermal results. In addition to a modification of the power consumed by the satellite during these phases (see Tab. 5.9), a change of attitude is also necessary. As explained in Section 1.5, the satellite must point the payload opening hole ($-Z$ face) nadir for the imaging phase, while the S-band patch antenna must point the Earth for the communication mode (see Fig. 6.30 and Fig. 6.31). To remain concise, only the *Body Mounted* configuration is studied, with the two most extreme orbits: cold 800 km SSO and hot ISS orbit.

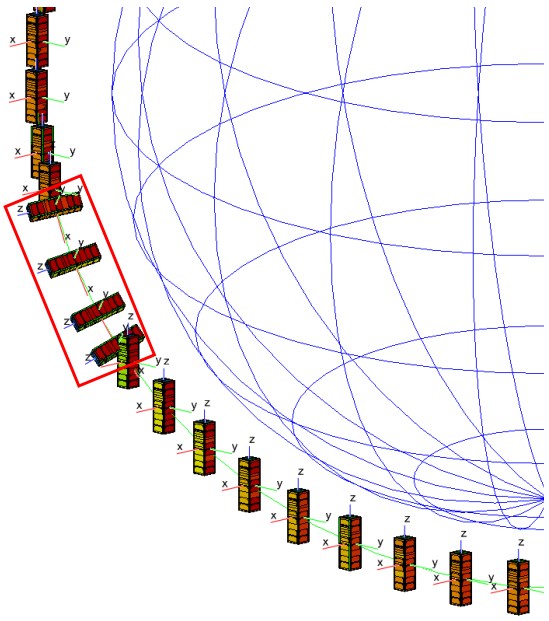

Fig. 6.30: Representation of the change of attitude for the acquisition mode (*Body Mounted* configuration) in ESATAN.

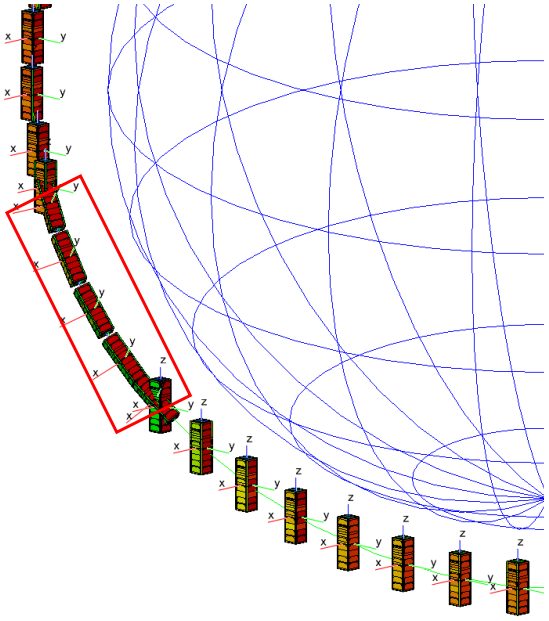

Fig. 6.31: Representation of the change of attitude for the communication mode (*Body Mounted* configuration) in ESATAN.

Because the satellite is a demonstrator, the requirements regarding the imaging and communication frequencies are not fixed. However, their duration is determined by the SYSE subsystem in [2] (imaging mode: 5 minutes and communication phase: 7 minutes[1]). It is decided to base the study on the number of operational orbits per day. 14.28 orbits are done per day if the 800 km SSO is considered, while the satellite achieves 15.54 revolution for the ISS orbit. Nonetheless, it is assumed that both of them lead to 15 orbits per day to allow a better representation of the operational orbits' frequency. If there are several of these orbits per day, it is assumed that they are equally distributed in time. For instance, if there is 1.25[2] imaging orbits per day, it means that the satellite makes 1 observing orbit followed by 11 idle ones and then the cycle is repeated. It is also chosen to decouple the communication and imaging modes. It means that only one of the two phases is considered at a time. Lastly, the results presented in the following figures show only the first three orbits of the cycle[3]. Because the computation is done on the entire cycle, the

[1] These times are estimated and correspond to the total time the satellite stays in the corresponding orientation. For the imaging mode, for instance, the satellite points the optical instrument nadir during 5 minutes but the actual imaging (taking picture) lasts 1 minute.

[2] $1.25 = 15/(1 + 11)$

[3] A cycle is composed on 1 operational orbit followed by n idle ones.

cyclic conditions (same temperature and temperature slope at the beginning and at the end) are applied to the whole cycle of $n + 1$ orbits. Hence, it is expected that the first and last values of the temperature curves displayed hereafter are not the same. This concept is illustrated in Appendix E.

6.3.1 Acquisition mode

By definition, the cold case orbit assumes no electrical dissipation at the components' level. Thus, the operational orbits differ from the idle ones only by a change of attitude. However, in the hot case, the dissipation has to be considered. Hence, it has to be adapted to fit the operational case. These values are presented in Tab. 5.9. For the acquisition orbit, they result in Fig. 6.32, where it can be seen that the payload's dissipation/consumption increases during the imaging phase (light blue zone). It also shows that the remaining power ($Q_{prod} - Q_{cons}$) dissipated by the solar cells adapts during this period. The dissipation of the idle orbits following the acquisition one corresponds to the constant values reached at the end of Fig. 6.32.

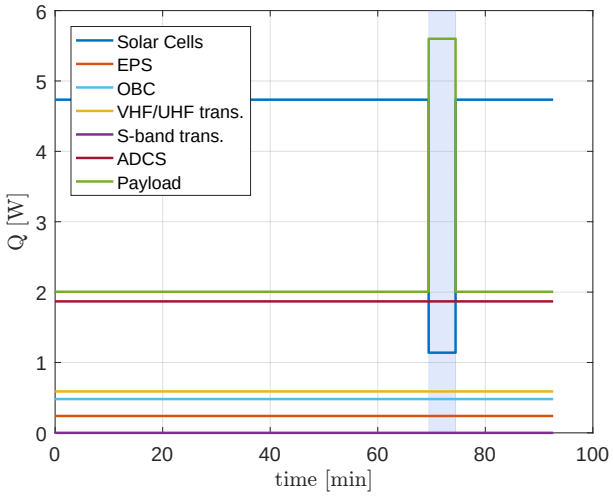

Fig. 6.32: Dissipation of the *Body Mounted* configuration during the hot ISS imaging orbit.

Fig. 6.33 and Fig. 6.34 present the temperature of the payload and batteries for the cold 800 km SSO and hot ISS imaging orbits as a function of the frequency of these events. These figures show the first three orbits of the cycle. They are delimited by vertical black dashed lines and the first one corresponds to the common observing orbit. The common imaging period is highlighted by a light blue zone[1], while the eclipses are represented by light grey rectangles.

A comparison between Fig. 6.33 and Fig. 6.34 shows that the temperature variation of the entire cycle is less important for the hot case than for the cold on. This is not surprise since the hot ISS orbit does not have eclipses. It is also seen that the increase in temperature during the imaging phase of the acquisition orbit is more marked in the hot case. This is because of the change in dissipated power. Moreover, the bump in the curves is larger for the payload in both hot and cold cases. This observation is explained by the fact that the payload is directly exposed to the environment by its aperture. Hence, after the change of attitude, when this hole is facing the Earth, it receives additional albedo and IR fluxes.

The largest difference in temperature between different frequencies occurs just after the observing period and lasts approximately one orbit. After that, it is seen that all the curves

[1]Out of the 6 curves presented in each figure, only the one corresponding to a frequency of 15 observing orbits per day has three imaging phases represented. For the other ones, the first orbit is the acquisition one (except for the dark blue curve), while the other two are idle orbits.

except the one corresponding to 15 observations per day rejoin progressively the reference dark blue curve (no acquisition orbit). Because of the overall smallest amplitude variation of the temperature for the hot cycle, it is seen that all the curves (except the light blue one) are superimposed at the end of the cycle[1]. It means that the observing phase has a very low influence on the temperature if one waits long enough. On the other hand, for the cold case, the curves get close to each other at the end of the cycle but a small temperature difference is still visible (0.8°C between the reference curve and the one corresponding to 3 acquisitions per day for the payload).

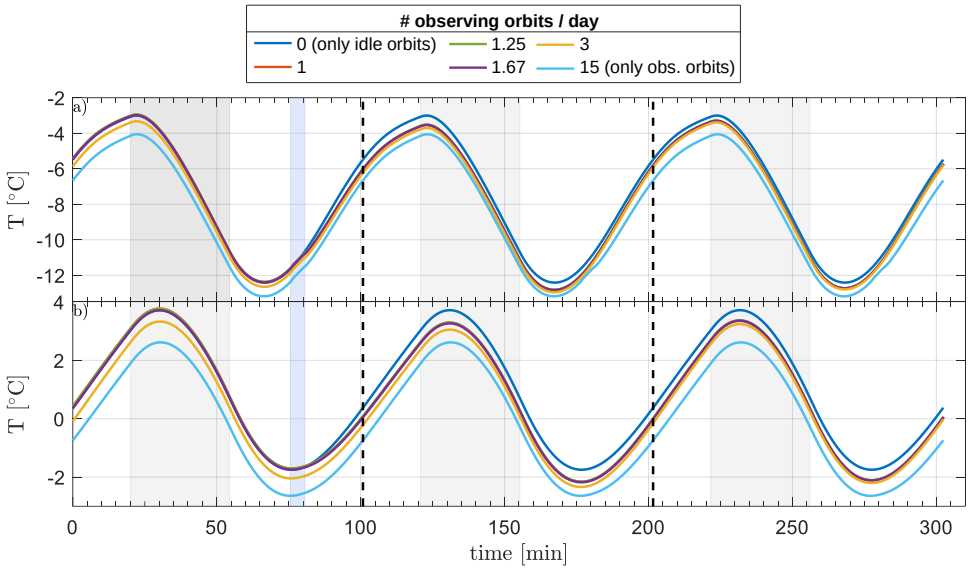

Fig. 6.33: Influence of the acquisition frequency on the temperatures of the payload (a) and batteries (b) for the *Body Mounted* configuration, cold 800 km SSO.

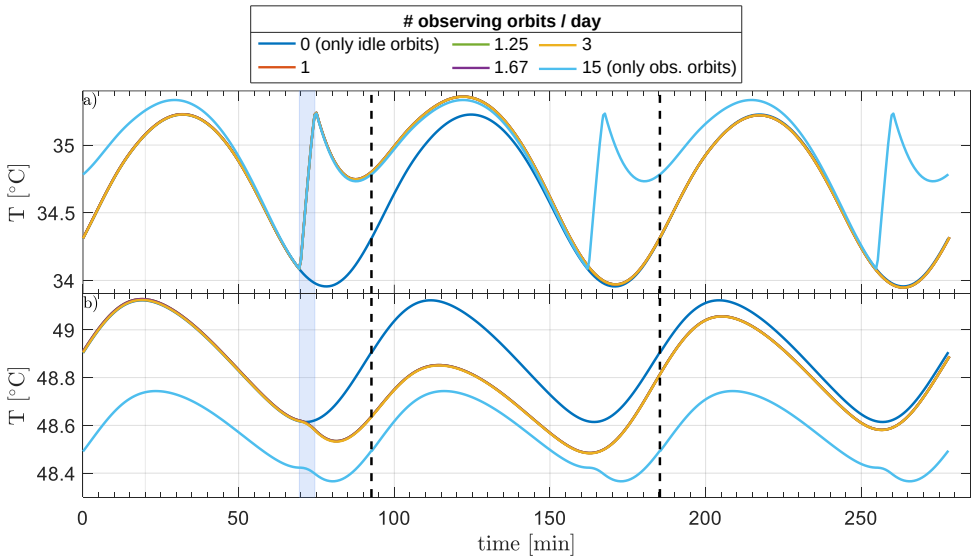

Fig. 6.34: Influence of the acquisition frequency on the temperatures of the payload (a) and batteries (b) for the *Body Mounted* configuration, hot ISS orbit.

[1]Because the analysis is cyclic, the end of the cycle corresponds to the time $t = 0$.

6.3.2 Communication mode

For the communication phase, the satellite must point its S-band patch antenna (located on face $-X$) nadir. As for the imaging mode, the cold case is achieved by a simple change of attitude whereas the hot case has to take into account electrical dissipation. Tab. 5.9 shows that this mode is characterized by an increased consumption/dissipation of the S-band and VHF/UHF transceiver circuit boards. The table also shows that the total consumption of the communication phase is larger than the electrical production of the *Body Mounted* configuration. However, because this phase only lasts 7 minutes, it is assumed that the batteries provide the additional power required. Hence, there is no more excess power to dissipate at the solar cells' level. Finally, the dissipation scheme of a communication orbit is displayed in Fig. 6.35.

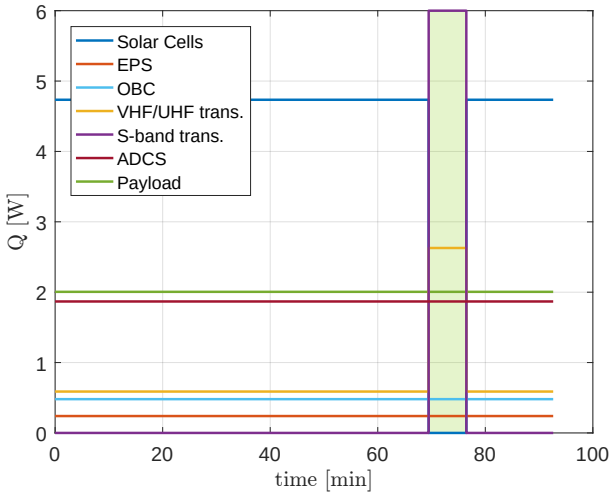

Fig. 6.35: Dissipation of the *Body Mounted* configuration during the hot ISS communication orbit.

Fig. 6.36 and Fig. 6.37 show the temperature of the payload and the batteries in function of the communication orbit frequency. In these figures, the common communication phase is represented by a light green zone. The two figures show that the communication orbit does not have a significant influence on the payload's temperature. In fact, at the end of the cycle, both cold and hot cases exhibit a variation of temperature of approximately 0.5°C between the reference orbit and the one corresponding to 15 communication orbits per day. The phenomenon is even less perceptible for the batteries temperature of the cold case.

On the other hand, the communication frequency has a larger influence on the batteries if the hot case is considered. It is seen in Fig. 6.37 that there is a 2°C variation between the light blue and the dark blue curves. It is explained by the electrical dissipation of this case. The latter is important for the S-band and VHF/UHF transceivers (6 W and 2.6 W respectively). Because of the proximity between the batteries and these PCBs, a larger temperature difference is observed. However, one sees that all the curves (except the light blue one) drop abruptly to the reference temperature given by the idle orbits. In fact, at the end of the cycle, the temperature difference is negligible.

6.3.3 Conclusion

Because OUFTI-Next will be a demonstrator, and there is no clear scientific requirements on the number of imaging phases per day, the project team has decided that *a few pictures per day*

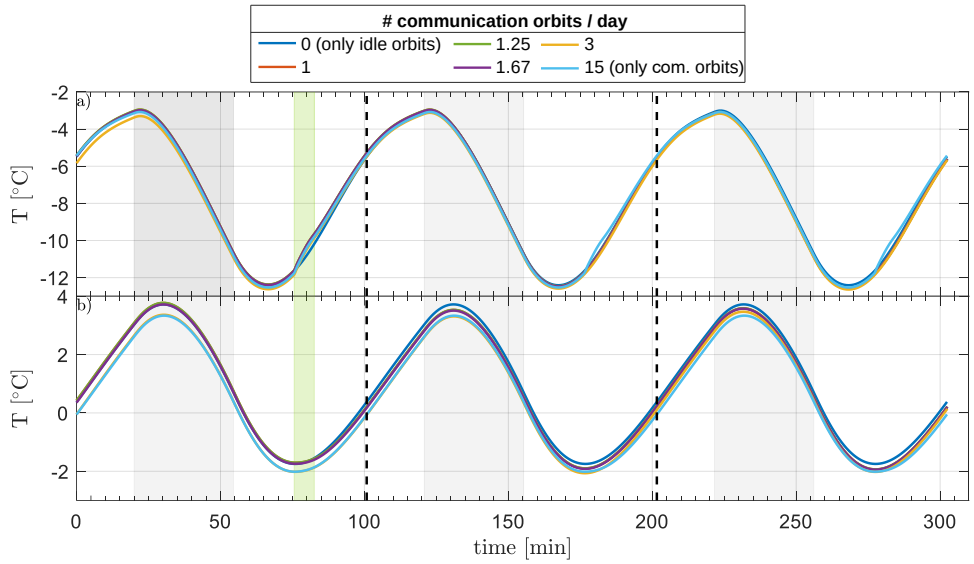

Fig. 6.36: Influence of the communication frequency on the temperatures of the payload (a) and batteries (b) for the *Body Mounted* configuration, cold 800 km SSO.

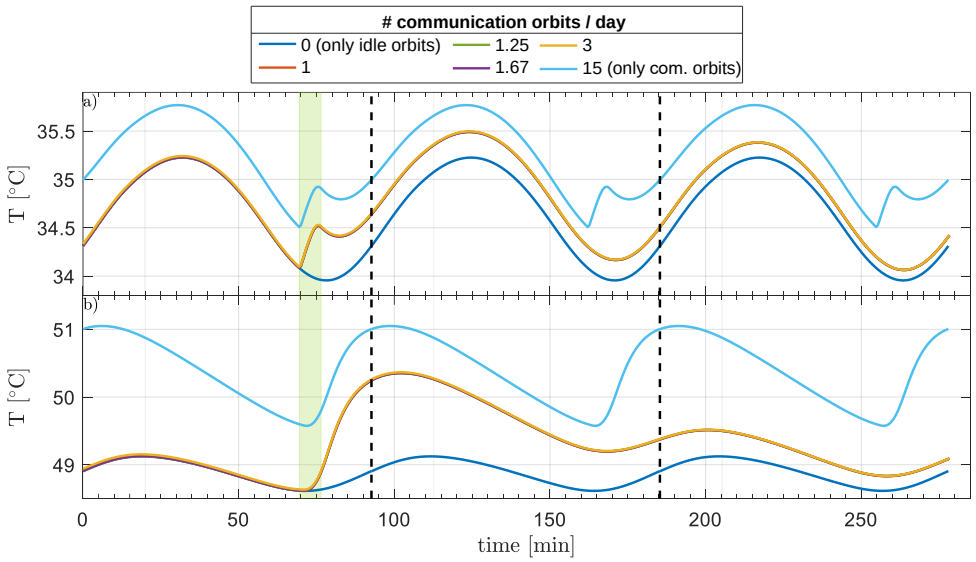

Fig. 6.37: Influence of the communication frequency on the temperatures of the payload (a) and batteries (b) for the *Body Mounted* configuration, hot ISS orbit.

would be enough to prove the good implementation of the mission. According to the feasibility study in [56], the integration time of the IR detector is approximately 100 ms. It results that tens of images can be taken per minutes (the amount of memory on the OBC has also to be considered). Hence, one observation orbit per day would be plenty enough. In addition, the SYSE subsystem demonstrated in [2] that the S-band patch antenna can transfer around 100 images per communication phase if a 8 bits coding is used. It means that a single communication orbit per day would also be sufficient. In this case, it is seen that the operational modes of the satellite do not influence the thermal results obtained with the idle mode. In fact, as it has been shown in this section, even considering 3 operational orbits per day does not have much influence.

6.4 Uncertainty analysis

Because of the early stage of the mission, many assumptions related to thermal parameters had to be made to obtain the nominal temperatures presented earlier. To build a robust model, the effect of these uncertainties has to be taken into account. The philosophy is depicted in Fig. 6.38 from [57].

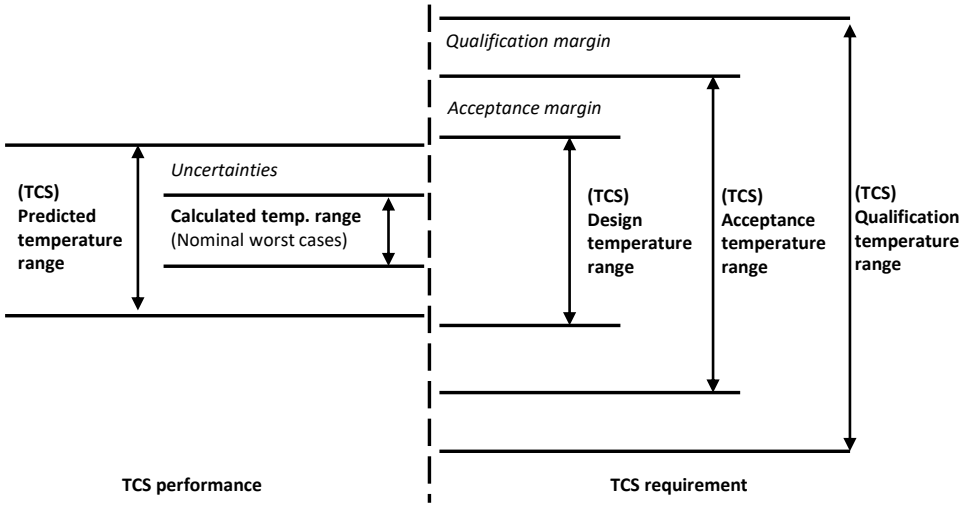

Fig. 6.38: Temperature uncertainties and margin definition [57].
TCS = Thermal Control System.

The left side of the figure corresponds to the performance of the thermal model. Starting from the nominal model, uncertainties must be added to obtain the predicted temperature range of the satellite. This range is defined by the worst hot (upper line) and the worst cold (lower line) thermal cases. Then one has to prove that the spacecraft fits the design temperature range. It corresponds to the range specified for the operating and non-operating modes.

The good behaviour of the satellite has also to be tested. The acceptance test refers to conditions similar to those expected during the mission. Every satellite must be tested at acceptance level before launch. A typical acceptance margin (difference between design and acceptance temperature range) varies between 0 K and 5 K. If the mission planning allows it, a qualification test is also conducted. This one applies conditions more severe that those encountered in orbit. Because of these extreme conditions, the qualification test is often performed on a replica of the main satellite. Doing so proves that the satellite can withstand the qualification conditions while avoiding damaging the flight model. However, due to increased time and budget costs, this method is rarely used for CubeSats. For these nano-satellites, the proto-flight model approach is preferred, where testing is done on the final spacecraft at levels between acceptance and qualification. From a thermal point of view, the proto-flight testing differs for the other ones by the duration of the thermal cycles and the temperatures applied.

In the present work, the acceptance and qualification margins are not studied. Only the uncertainties on the nominal model are looked at. For an element i of the spacecraft, it is computed by [57]:

$$\Delta T_i = \sqrt{\sum_{j=1}^{n_p} (T_{nom} - T_j)_i^2 + \Delta T_S}\,,$$

where ΔT_S is a systematic temperature uncertainty of 3 K added to the results. T_{nom} is the nominal temperature and T_j is the temperature obtained when the uncertainty parameter j is used. They are listed in Tab. 6.1.

Parameter	**Value +**	**Value -**
Absorptance / emittance (α/ϵ)	+0.03/-0.03	-0.03/+0.03
Capacitance (c_P)	+20%	-20%
Contact conductance (h)	+100%	-50%

Table 6.1: Uncertainty parameters from [57].

The first line means that the uncertainties on the absorptance and emittance are combined and applied at the same time on the model. For the analysis, the change of contact conductance is also applied to the bolts. Normally, the orientation of the satellite should also be changed to account for pointing uncertainties. However, this attitude modification is not conducted here. Modifying the power dissipated by the satellite's components is also of good practice. Nonetheless, the values considered until now have already a 20% margin. Thus it is not considered necessary to add another one.

For sake of conciseness, only the *Body Mounted* configuration is analyzed and the worst two orbits are used: namely the hot ISS and cold 800 km SSO. The results are given in Tab. 6.2, where the *hot max* nominal temperature refers to the maximum temperature reached in the hot ISS orbit and *cold min* is the minimum one for the cold 800 km SSO. The table only shows the final uncertainties (fourth and fifth columns). However, the procedure to compute them is explained in Appendix F, where the effect of each uncertainty acting separately is displayed from Tab. F.1 to Tab F.4. These tables show that the uncertainty on the optical properties has the most influence on the results, as it changes them by approximately 5°C.

Tab. 6.2 gives the predicted temperatures (taking into account the uncertainties) and compares them to the thermal requirements of the components. This comparison is made in the last two columns, where the red color is used to highlight values that are not compliant with the allowable range. It is observed that some components fulfilled the requirements before the uncertainty analysis but do not anymore. It is the case of the shear panels, EPS and VHF/UHF transceiver for the *hot max* temperature and the VHF/UHF dipole antenna for the *cold min* temperature. Finally, it is seen that the worst case occurs for the charging batteries if the *hot max* temperature is considered (margin of −15°C).

Element	Nominal		Uncertainties (ΔT_i)		Prediction (with uncert.)		Requirements		Margin	
	Hot max	Cold min	Hot max	Cold min	Hot max	Cold min	Hot	Cold	Hot	Cold
Structure	45.5	-15.0	11.0	9.7	56.5	-24.6	80	-40	23.5	15.4
Shear panels	67.6	-24.1	13.5	8.9	81.1	-33.0	80	-40	-1.1	7.0
Solar cells	68.9	-24.4	13.4	8.9	82.3	-33.3	125	-55	42.7	21.7
S-band patch	24.6	-27.6	16.4	11.2	41.0	-38.9	45	-25	4.0	-13.9
GPS patch	24.5	-27.7	16.4	11.3	41.0	-39.0	45	-40	4.0	1.0
Radiator	33.1	-13.2	9.8	9.4	42.8	-22.6	-	-	-	-
Batteries (charge)	49.1	-1.7	10.8	10.1	60.0	-11.9	45	0	-15	-11.9
Batteries (discharge)	49.1	-1.7	10.8	10.1	60.0	-11.9	60	-20	0	8.1
EPS	49.4	-3.4	10.8	10.1	60.2	-13.5	60	-20	-0.2	6.5
OBC	50.0	-4.5	10.8	10.1	60.8	-14.6	65	-25	4.2	10.4
VHF/UHF trans.	49.9	-5.6	10.8	10.0	60.7	-15.6	60	-20	-0.7	4.4
S-band trans.	48.8	-6.8	10.8	10.0	59.6	-16.9	60	-40	0.4	23.1
VHF/UHF ant.	46.2	-12.5	10.9	9.9	57.1	-22.3	60	-20	2.9	-2.3
ADCS	48.7	-6.1	10.4	10.0	59.1	-16.1	85	-45	25.9	28.9
Payload	35.2	-12.4	9.7	9.4	45.0	-21.9	-	-	-	-

Table 6.2: Uncertainty analysis (temperatures in °C).

6.5 Thermal design

The last section of this Master's thesis is dedicated to the thermal design of the satellite. Modifications are applied to the original satellite's model to try to reach the allowable operational temperatures of all the components. This study is principally done on the *Body Mounted* spacecraft's configuration and is based on the temperatures accounting for uncertainties (Tab. 6.2) as well as on the heat flow maps (Fig. 6.10 and Fig. 6.11).

The points that need to be addressed are summarized hereafter:

- Tab. 6.2 showed that the batteries are too hot in the hot case and too cold in the cold case to operate safely when charging. The differences between the temperatures reached and the allowed ones are 15°C and 11.9°C for the hot and the cold cases respectively.
- The S-band patch antenna is 13.9°C too cold in the cold case if the uncertainties on the nominal temperature are taken into account.
- One wants to reduce the payload's temperature as much as possible. The conductive link with the radiator, which has been studied by the COOL subsystem in [19], will not be modified here. Moreover, the heat exchanges with the environment cannot be modified without implementing complex solution like a sun shield (the radiator's coating is also fixed by the COOL subsystem). Therefore, only the heat exchanged with the other spacecraft's components can be modified by thermal design. Fig. 6.10 and Fig. 6.11 showed that the payload receives a significant amount of radiative power from the other spacecraft's components (2.1W in the hot case and 1.2 W in the cold one). The conductive link with the structure is also a large contributor to the high temperature of the payload. In fact, it gives 1.7 W and 1.8 W to the payload in the cold and hot cases respectively.
- The heat flow maps also showed that a non negligible quantity of thermal power flows conductively from the structure to the radiator (1 W in the cold case and 0.9 W in the hot one). Reducing this power will lead to a colder radiator, making it more efficient to extract heat from the payload.
- Tab. 6.2 showed that the VHF/UHF dipole antenna module is 2.3°C too cold in the cold case of Tab. 6.2.
- The shear panels, the EPS and the VHF/UHF transceiver are maximum 1.1°C too hot in the hot case.

Out of these six outcomes, only the first four can be considered as key drivers for the thermal design. Dedicated solutions will be investigated. The other ones have smaller differences between the temperature reached and the requirements.

The thermal design procedure is the following one. The starting point is the nominal model presented in Section 6.2, on which modifications are applied. Then the uncertainties on this new model are computed in a similar way as in Section 6.4 and the margins are looked at. If they are still negative, the procedure is restarted with a different solution until appropriate results are obtained. However, for the sake of brevity, only the final solution is presented in this paper. Moreover, the thermal design is made on the most restrictive orbits: the cold 800 km SSO and the hot ISS orbit. Nonetheless, once the final design will be chosen, the temperature curves of all the components and for all orbits will be shown in appendix.

6.5.1 Coating modification

A first observation from Tab. 6.2 shows that there are margins for the majority of the internal components in the cold case. Hence, one deduces that reducing the temperature of all the satellite by applying the correct coating is feasible. It will cool down both the payload and the batteries. Cooling the payload has, without any doubts, a positive effect. However, the motivation to reduce the batteries' temperature needs further explanation. It is seen in Tab. 6.2 that the batteries are both too cold and too hot depending on the thermal case considered if they are charging. Hence, one expects a solution able to adapt to the situation (cool them down in the hot case and heat them up in the cold one). Therefore, an active solution seems necessary. Heating a component actively (heaters) is considered easier than cooling it down (peltier). Hence, it has been decided to cool the batteries passively until they fulfill the requirements in the hot case. Then, they can be heated up by heaters. They can be turned either on or off depending on whether additional heating is required or not.

To reduce the global temperature of the spacecraft, it is chosen to replace the coating of the faces which do not support solar cells (i.e. faces $-X$, $-Y$ and $-Z$). These ones are constantly hidden from the Sun and thus only receive albedo and Earth IR fluxes. After several attempts, it is deduced that the temperature is reduced if the coating has a small α/ϵ ratio. Compared to the initial alodined aluminum coating, the new coating must have a lower solar absorptivity and a higher infrared emissivity. The lower α means that the panels absorb less albedo power, while the high ϵ increases the IR absorption. However, it also increases the radiative exchange with the environment and thus contributes greatly to evacuate more heat power.

A good candidate is the S-13G-LO white silicon paint with at thickness of 10 mils (=254 μm) [27]. The optical properties of this white paint are compared to the alodined aluminum surface finish in Tab. 6.3. It can be seen that the solar absorptivity is divided by 2 and the emissivity is multiplied by 6 (BOL values). Even if the end of life values (EOL) are considered, the paint still outperforms the original coating.

Coating	α [-]	ϵ [-]	α/ϵ
Alodined aluminum	0.44	0.14	3.14
S-13G-LO white silicon paint, 10 mils (BOL)	0.22	0.88	0.25
S-13G-LO white silicon paint, 10 mils (EOL - 5 years in orbit)	0.47	0.88	0.53

Table 6.3: S-13G-LO white silicon paint compared to alodined aluminum [27].

The effects of the S-13G-LO white silicon paint are shown in Fig. 6.39 and Fig. 6.40 for the cold 800 km SSO and the hot ISS orbit respectively. The temperature of the batteries is represented by blue lines, while the payload is associated to green ones. It can be seen that this new coating is beneficial for both the batteries and the payload since it reduces their temperature by approximately 10°C with respect to the original coating. The figures also show that the EOL properties of the paint do not have a significant influence on the results. Hence, only the BOL values will be considered.

6.5.2 New spacer design

As a reminder, the spacers are hollow cylinders (initially in Al 6061) placed on the threaded rods supporting the circuit boards. Their role consists in maintaining a constant distance between two adjacent PCBs or between the internal spacecraft's elements and the structure.

Fig. 6.10 showed that the batteries receive conductive thermal power from the EPS board in the hot case. In this situation, the intention is to reduce this power flow in order to decrease the

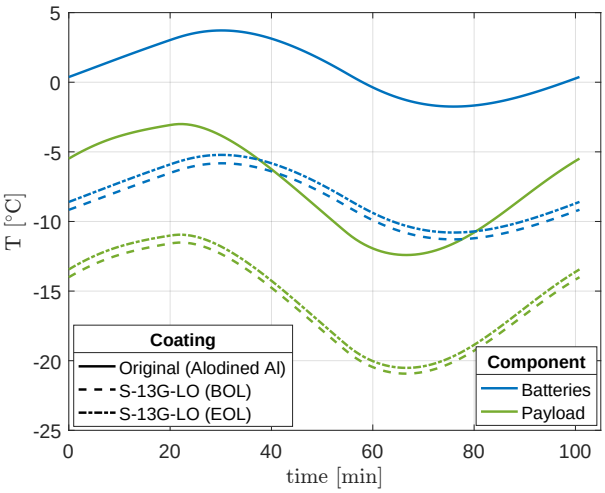

Fig. 6.39: Effect of the S-13G-LO coating on the batteries and payload's temperature for the cold 800 km SSO.

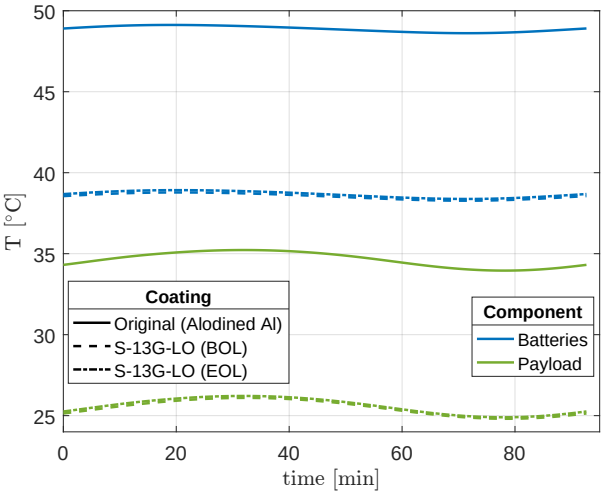

Fig. 6.40: Effect of the S-13G-LO coating on the batteries and payload's temperature for the hot ISS orbit.

heating of the batteries by the underneath PCB. On the other hand, one sees in Fig. 6.11 that power flows from the batteries to the EPS in the cold case. In this thermal case, the batteries are too cold. In order to heat them up, a solution is to reduce this loss of thermal power towards the EPS PCB. Moreover, in the cold case, if an active solution is used, it is necessary to prevent the power generated by the heaters from escaping towards the other parts of the satellite. In summary, decreasing the conductivity of the spacers binding the batteries to the EPS is beneficial in all situations.

Fig. 6.12 and Fig. 6.13 showed that a non negligible amount of power coming from the structure (conductive link) heats up the payload. Reducing the conductivity of the spacers linking it to the structure is thus foreseen.

Plastic materials, and more specifically thermoplastics (Teflon, Nylon, acrylic, ABS, ...)[1] are better insulators than metals [58] and constitute a tempting choice for the spacers. However, they have poor structural properties (lower Young's modulus than metals, risks of creep phenomena, crazing, brittleness at low temperatures, ...) and are susceptible to outgas in vacuum and thus to contaminate sensitive equipments. Hence, the initial aluminum spacers cannot be replaced by thermoplastics alone. Instead, a combination of titanium (high Young's modulus and thermal conductivity 23 times lower than Al) and thin Nylon washers is used. A compromise must be found between the need for a larger thermal resistance (⇒ thick Nylon washers) and the need for good structural properties (⇒ thin Nylon washers).

The best compromise is found from a parametric analysis of the evolution of the thermal conductivity when the proportion of Nylon washer varies with respect to the titanium spacer. As shown in Fig. 6.41, the titanium spacer is surrounded by two washers. It means that, for instance, in case of a proportion of 20% Nylon and 80% titanium, each washer is effectively 10% of the total height (⇒ if the total gap between 2 PCB is 10 mm, then the Ti spacer is 8 mm and the two Nylon washers are 1 mm each).

[1]Chemical names of these plastics: Teflon: polytetrafluoroethylene (PTFE); Nylon: part of polyamide family; acrylic: polymethyl methacrylate (PMMA); ABS: Acrylonitrile butadiene styrene.

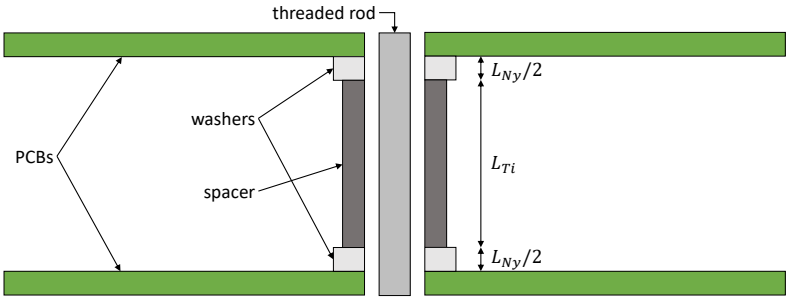

Fig. 6.41: Schematic representation of the new spacer-washers assembly[1].

The equivalent thermal resistance of the entire assembly (2 washers + 1 spacer) is given by:

$$R_{eq} = \frac{1}{A}\left(\frac{L_{Ny}}{k_{Ny}} + \frac{L_{Ti}}{k_{Ti}}\right) = \frac{L_{Ny} + L_{Ti}}{A k_{eq}},$$

where A is the common cross section of the two elements, L_{Ti} is the length of the titanium spacer and L_{Ny} is the total length of Nylon (each washer has a length of $L_{Ny}/2$). The thermal conductivity of titanium is $k_{Ti} = 7.8$ W/mK [27], while the conductivity of Nylon is $k_{Ny} = 0.25$ W/mK [59]. Finally, the equivalent conductivity is computed by:

$$k_{eq} = \frac{k_{Ny} k_{Ti}}{x\,(k_{Ti} - k_{Ny}) + k_{Ny}},$$

where the fraction of total length of Nylon is represented by $x = L_{Ny}/(L_{Ny} + L_{Ti})$.

The evolution of the equivalent conductivity as a function of the fraction of Nylon in height is represented in Fig. 6.42. It is observed that increasing the Nylon percentage has more effect if the proportion is low (below 15%). The benefit becomes negligible if the fraction is larger than 40%. Anyway, such a high proportion of Nylon should be avoided for structural integrity reasons.

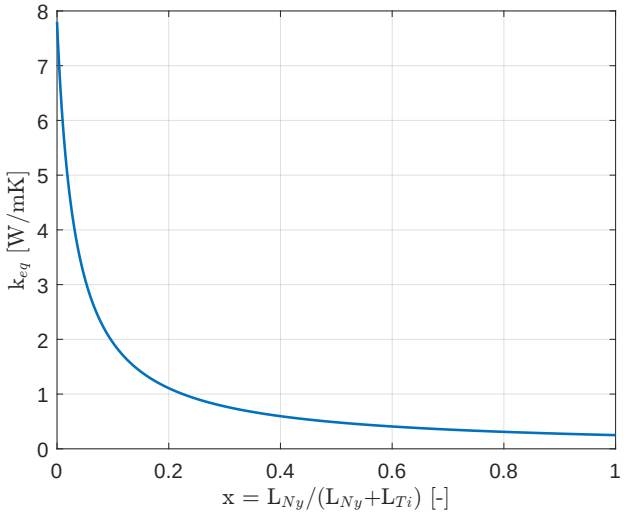

Fig. 6.42: Equivalent conductivity of the spacer-washers assembly as a function of the proportion of Nylon.

[1]The figure shows 2 PCBs but the same combination of spacer and washers can be applied to any link using spacers (PCB stack - structure, payload - structure, ...).

Finally, a 10% proportion of Nylon is chosen. This one induces an equivalent thermal conductivity of 1.94 W/mK. This value is 93 times smaller that the original aluminum spacers ($k_{Al} = 180$ W/mK). It is important to remember that this thermal conductivity concerns only the spacers/washers. If this new design is used on the link between two adjacent PCBs, the reduction in conductivity between the two boards will be less important because the thermal path via the phosphor bronze pins has to be considered as well. These pins are standardized and cannot be modified to change their conductivity.

Since the aluminum spacers linking the batteries to the EPS were 11.3 mm long, the new model is composed of a titanium spacer of 10.3 mm and two Nylon washers of 0.5 mm each[1]. For the payload, the Nylon washers are 1.25 mm thick each. Regarding its link with the structure, the half rib must be taken into account as well (cf. Section 5.2.1).

During the iterations of the thermal design, it was observed that the VHF/UHF dipole antenna module's temperature was too low in the cold 800 km SSO. On the other hand, Fig. D.3 showed that its temperature amplitude was high in the original model. Using the new spacer/washer design leads to a flatter temperature curve. Meaning that its maximum value is decreased and that its minimum one is increased. The original spacers were 4 mm tall. Hence, the Nylon washers are 0.2 mm thick each. In additionally to this design modification, it is also decided to reduce the number of links with the structure. In Section 5.2.1, the dipole antenna was fixed by 8 spacers (4 on top and 4 below). Hence, in order to further reduce the conductive link, the new model only includes 4 fixations. Because of the low mass of the dipole antenna (85 g), it is assumed that this number is enough to ensure a good structural link between the two elements.

Finally, the old and new conductive links of these components are presented in Tab. 6.4.

Link	**Al spacer**	**Ti spacer + Nylon washers**
Batteries - EPS	0.38	$4.5{\cdot}10^{-3}$
Payload - structure	0.18	$3.7{\cdot}10^{-3}$
Dipole antenna - structure	0.31 (8 spacers)	0.0109 (4 spacers)

Table 6.4: Conductive links [W/K] using old (aluminum) and new (titanium + Nylon) spacers.

6.5.3 Washers for the radiator

As mentioned earlier, power flows conductively from the structure to the radiator. It has the effect to heat up the latter. By reducing this heat exchange, the temperature difference between the radiator and the payload is expected to increase, meaning that more thermal power can be extracted from the payload.

This design modification is similar to the previous one and consists in adding thin Nylon washers between the radiator and the structure. Hence, heat will have to cross both the contact resistance of the bolts and the one of these new washers. Contrarily to the previous section, the Nylon material is just an addition to the initial design (not necessary to re-size other parts like the spacers - cf. Fig. 6.42). The evolution of the conductive link between the radiator and the structure is displayed in Fig. 6.43 for an increasing thickness of the Nylon washers.

Once again, it is seen that the benefit of increasing the Nylon's thickness is larger if it is initially small. For structural integrity reasons, the washers must be as thin as possible. Their

[1]These values do not correspond exactly to a proportion of 10% Nylon because manufacturing and material purchasing constraints have to be taken into account. It is reasonable to think that 0.5 mm Nylon spacers are more common than $11.3 \cdot 0.1/2 = 0.565$ mm ones.

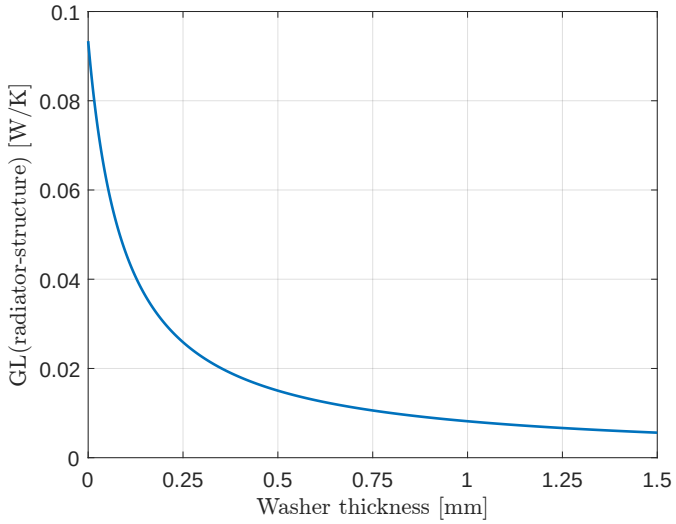

Fig. 6.43: Conductive link [W/K] between the radiator and the structure when the Nylon washer's thickness increases.

height must also remain small because they contribute to increase the distance between the radiator and the structure. Hence, a value of 0.5 mm is chosen. It leads to a conductivity of 0.015 W/K, which is more than six times smaller than the original value.

6.5.4 Payload's radiative insulation

As seen in Fig. 6.12 and Fig.6.13, the payload receives several watts of thermal power radiatively from the other spacecraft's components. Reducing this quantity would decrease the payload's temperature. Because it is not possible to coat it directly (the payload is composed of optical lenses/mirrors), a new element must be added to the spacecraft. This part surrounds entirely the payload (except for the aperture hole) and is represented in yellow in Fig. 6.44.

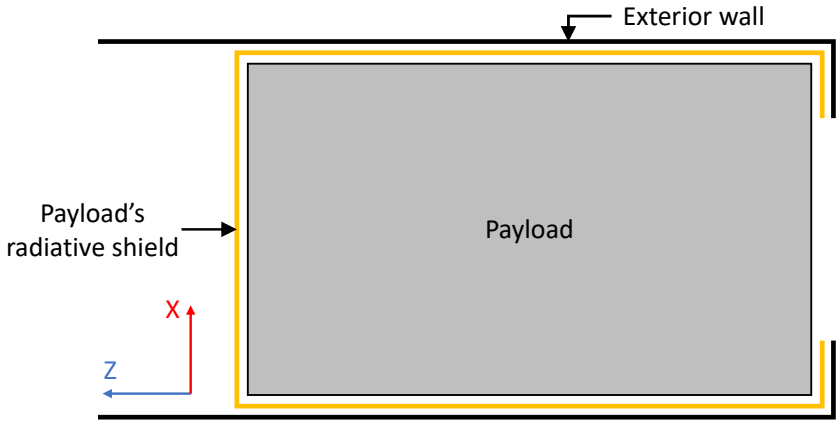

Fig. 6.44: Radiative shield surrounding the payload.

The most common way to make a radiative shield is to use multi-layer insulation (MLI). However, the plastic films composing the blankets are subjected to outgassing. If this problem is not addressed (bake-out prior to integration in the satellite), the gas will contaminate the payload. Because the detector is the coldest spot, it is expected that the gas will condensate extensively on this element and ruin the mission.

An important parameter characterizing the MLI is the effective emittance $\epsilon^\star$. This value refers to the emittance of all the internal layers together and is computed by empirical relations. The lower this parameter is, the better the performance of the MLI is. As stated in *Spacecraft Thermal Control Handbook* by D. Gilmore [27], the performance of MLI is strongly influenced by heat leaks (edge effect, seams, cable and support elements penetration, ...). Hence, it is more advantageous to use MLI on large surfaces (smaller relative proportion of heat leaks compared to the total area) than on small ones. This point is illustrates in Fig. 6.45. In the case of OUFTI-Next, the total surface area needed to surround the payload is 0.078 m^2. The discontinuity density would probably be characterized as *medium* or *high* because of the numerous edges and the relatively high amount of penetrating components (electrical connectors between the detector and the OBC as well as the supports linking the payload to the structure). Hence, a realistic value of $\epsilon^\star$ would be around 0.1. Finally, because of this high value and the possible contamination problems, the MLI solution is discarded for the satellite.

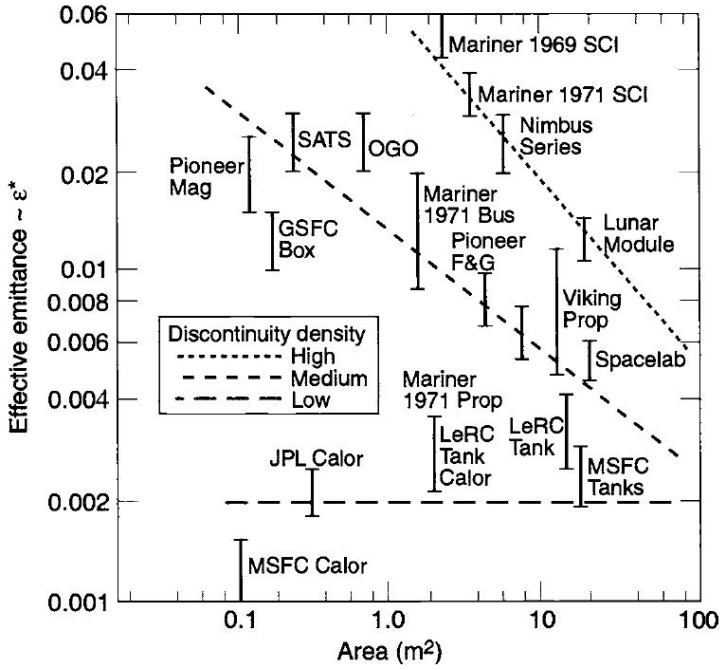

Fig. 6.45: Influence of the surface area and heat leak (discontinuity) density on the effective emittance of MLI [27].

Another solution is to use coated metal plates to make the radiative heat shield. It is chosen to use aluminum as the base material and to coat it with gold. With a panel's thickness of 0.1 mm, the total mass of the component is kept under 25 g. If the gold is plated on the panels and then polished an emissivity of 0.02 can be achieved [27].

6.5.5 S-band patch antenna's thermal design

Tab. 6.2 showed that the S-band patch antenna is 14°C too cold in the cold case if the uncertainties are taken into account. To increase its temperature, a high α/ϵ coating is required (the original coating was Kapton $\Rightarrow \alpha/\epsilon = 0.57$). The high α ensures a larger absorption of albedo power (the antenna never sees directly the Sun), while the low ϵ reduces the evacuation of thermal power. It is thus chosen to use *Chromacoat aluminum paint* ($\alpha = 0.28$, $\epsilon = 0.05 \Rightarrow \alpha/\epsilon = 5.6$ [27]). The effect of this new coating is represented in Fig. 6.46 by the red curves and shows an

average temperature increase of 18°C in the cold case.

The figure (red curve) does not take into account the uncertainties that might lead to lower temperatures. Moreover, the dashed red curve shows that the component undergoes large temperature variations (20°C) along its orbit due to its small thermal inertia. The conductive link with the structure also contributes to this large amplitude. The latter can be reduced by using the same 0.5 mm thick Nylon washers as for the radiator. This modification reduces the original conductance by a factor 6. The effect of this new link combined with the S-band's coating is represented by the green curves in Fig. 6.46.

Unfortunately, these two modifications have impacted the temperature of the batteries by rising it by a few degrees. This effect is countered by coating the inside face of the shear panels with *Martin black paint N-150-1* ($\alpha = 0.94$, $\epsilon = 0.94$ [27]). This high IR emissivity coating ensures a larger absorption of the power emitted by the satellite's internal components. Because it increases the thermal absorption, it is seen in Fig. 6.46 that the S-band antenna's temperature increases slightly (the side of the antenna facing the interior of the CubeSat is also coated with black paint).

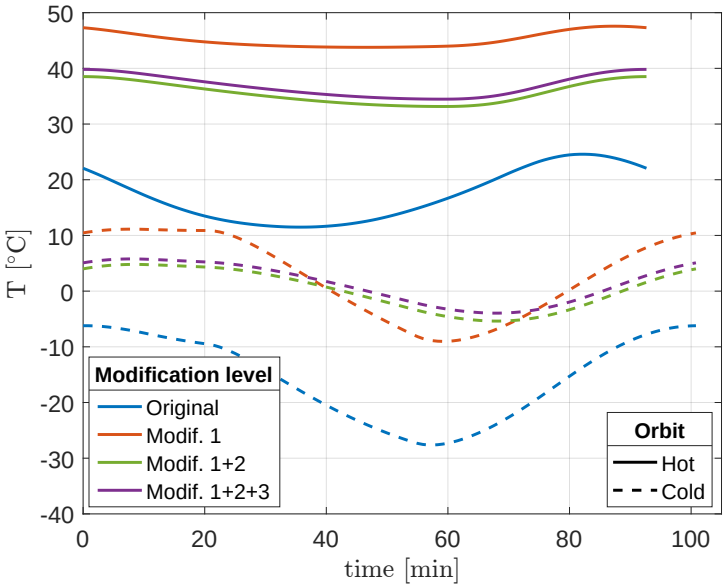

Fig. 6.46: Temperature of the S-band patch antenna in cold and hot cases depending on the design modification level. *Modif. 1: Chromacoat on patch antenna; Modif. 2: reduced conductive link; Modif. 3: black paint for the inside faces of shear panels.*

6.5.6 Summary and uncertainties

All the design modification applied to the *Body Mounted* configuration of OUFTI-Next are summarized in Tab. 6.5. Their effect on the payload's temperature is displayed in Fig. 6.47 and Fig. 6.48, where all the colored curves refer to the application of a single design modification at a time. The dashed black curve represents the initial temperature of the component and the solid black one gives the effect of all the modifications combined. The two figures show that the final design (solid black curve) is not the sum of all the design changes considered separately. Indeed, the different modifications influence each other. It is seen that the objective of decreasing the payload's temperature is met since a drop of a 42°C is observed in the cold case and 46°C in the hot one.

The individual temperature curves of all the elements are given in Appendix G. These curves

show the values for all the orbits (800 km SSO, 400 km SSO and ISS orbit), as well as for hot and cold cases.

	Before modification	**After modification**
Coating of external face of shear panels $-X$, $-Y$, $-Z$	Alodined aluminum ($\alpha = 0.44$, $\epsilon = 0.14$)	S-13G-LO white silicon paint ($\alpha = 0.22$, $\epsilon = 0.88$)
Coating of internal face of the shear panels	Alodined aluminum ($\alpha = 0.44$, $\epsilon = 0.14$)	Martin black paint N-150-1 ($\alpha = 0.94$, $\epsilon = 0.94$)
Coating of S-band patch antenna	Kapton ($\alpha = 0.38$, $\epsilon = 0.67$)	Chromacoat aluminum paint ($\alpha = 0.28$, $\epsilon = 0.05$)
GL(Batteries - EPS)	Al 6061 spacers (GL= 0.38 W/K)	Ti spacers + Nylon washers (GL= 0.0045 W/K)
GL(Payload - Structure)	Al 6061 spacers (GL= 0.18 W/K)	Ti spacers + Nylon washers (GL= 0.0037 W/K)
GL(Dipole ant. - Structure)	Al 6061 spacers ($\times 8$) (GL= 0.31 W/K)	Ti sp. + Nylon washers ($\times 4$) (GL= 0.0109 W/K)
GL(Radiator - Structure)	Bolts (GL= 0.09 W/K)	Bolts + Nylon washers (GL= 0.015 W/K)
GL(S-band antenna - Structure)	Bolts (GL= 0.06 W/K)	Bolts + Nylon washers (GL= 0.01 W/K)
Payload's radiative shield	-	Gold plated aluminum plates

Table 6.5: Summary of the thermal design modifications.

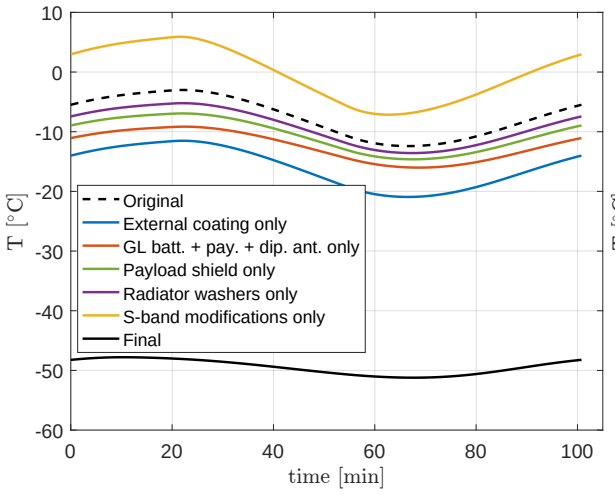

Fig. 6.47: Payload's temperature for several design modifications for the cold 800 km SSO. *Color curves: each modification is applied individually, black solid curve: all applied together.*

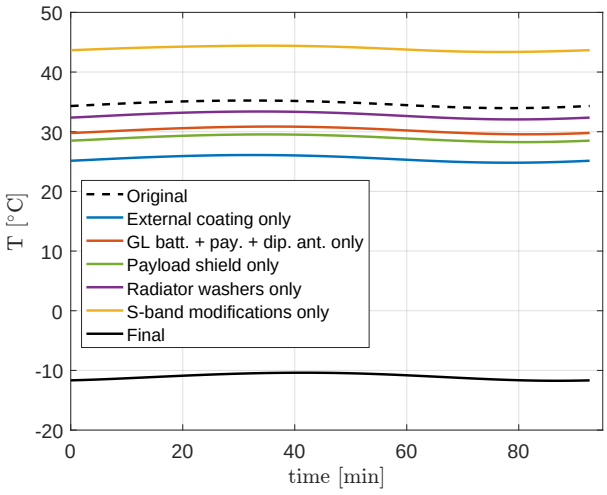

Fig. 6.48: Payload's temperature for several design modifications for the hot ISS orbit. *Color curves: each modification is applied individually, black solid curve: all applied together.*

The final design's heat flow map is represented in Fig. 6.49 for the hot ISS orbit[1]. This design has one more element represented: the payload's radiative shield. This component is composed

[1]The heat flow map of the final design for the cold 800 km SSO is represented in Fig. G.15 in Appendix G

of 2 nodes, hence the temperature written in Fig. 6.49 corresponds to a mean value. Compared to the original model (Fig. 6.10), the thermal design modifications have greatly reduced the power flowing from the structure to the payload, radiator, S-band antenna and VHF/UHF dipole antenna. Thanks to the radiative shield surrounding the payload, the radiative power coming from the structure has dropped from 1.5 W to 79 mW. It is observed that the conductive power going from the payload to the radiator decreases if the final model is considered. It is due to the smaller temperature gap between the two elements ($\Delta T = 0.5$°C for the final model and $\Delta T = 2.2$°C for the base model). The most important point concerning these two elements is that they are both much colder in the final design than in the basic model (approximately 45°C colder).

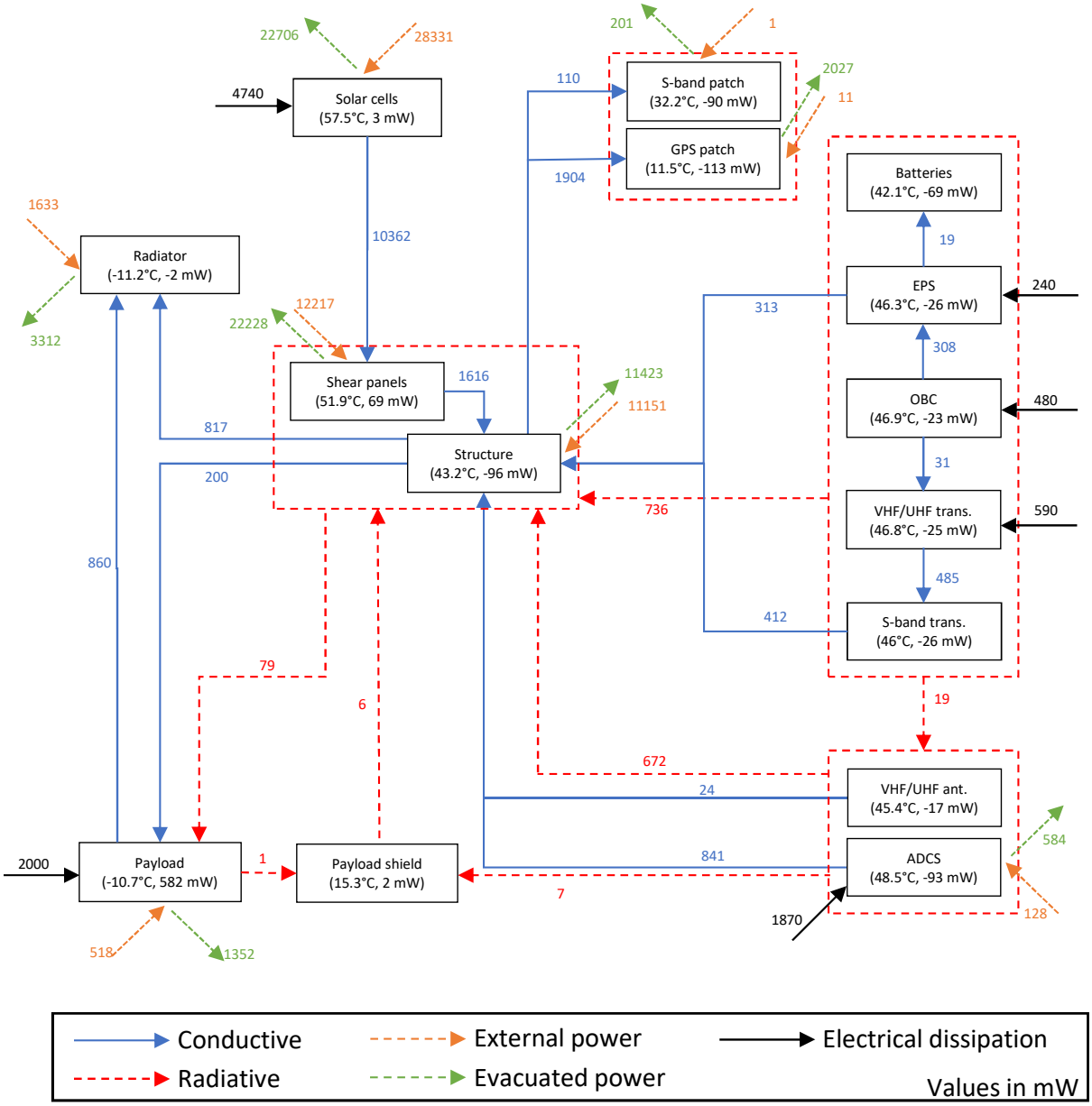

Fig. 6.49: Final design heat flow map of the *Body Mounted* configuration for the ISS hot case orbit at $t = 25$ min.

The uncertainty analysis on the final thermal design is conducted in the same way as in

Section 6.4 and the uncertainty parameters of Tab. 6.1 are used here. However, the new model has some components with a very low emissivity coating (e.g. gold plated payload's radiative shield: $\epsilon = 0.02$). Hence, an uncertainty of 0.03 on the optical properties is too high. Thus, if the original value of α or ϵ is 0.05 or less, the uncertainty applied is reduced to 0.01.

Tab. 6.6 shows the uncertainty analysis. The first half of the table is dedicated to the original model and the other one presents the results of the final thermal design. If a component is not compliant with its allowable thermal range, the margin value is negative and highlighted in red.

Contrarily to the original model, the final design has only one of its components out of the requirements if the nominal (without uncertainties) temperatures are considered. Indeed, the charging batteries are 4.4°C too cold in the cold case. However, if the uncertainties on the thermal properties are taken into account, one sees that the number of elements outside their allowable temperature range increases.

Tab. 6.6 shows that the shear panels can be 7.5°C too cold. However, as explained in Section 6.2.2, this situation is totally acceptable because they do not contain any electronic elements and it was explained that the material conserves its structural properties even outside the range defined by the manufacturer.

If the uncertainties are considered, it is seen that the S-band patch antenna, the GPS antenna, the EPS and the VHF/UHF transceiver PCB can be out of bounds. However, they are close to their requirements (maximum gap of 3.4°) and it is seen that there is a margin of at least 7°C between the nominal temperatures and the allowable temperatures. Hence, it is chosen to not optimize further the model for these components.

The table shows that the charging batteries are still too hot in the hot case if uncertainties are considered. Nonetheless, the nominal temperature is compliant with the thermal requirements. Hence, it is chosen to stop the thermal design here and not investigate further solutions to reduce their temperature. Indeed, it is judged wiser to wait for the project team to decide which model will be used in OUFTI-Next. Then, more precise information can be gathered from the manufacturer like the capacitance, the surface coating and the exact geometry. The uncertainties can also be reduced by testing the components to asses their real properties. It would also be interesting to study the loss of performance of the batteries if they operate out of the initial thermal range of 0°C to 45°C.

If the problem persists with these new data, a solution could be to use a thermal strap linking the batteries to the face $-Y$ of the satellite. As seen in Fig. 6.50 (blue curves), these two components have a large temperature difference. Moreover, this shear panel does not have any component that the strap could interfere with.

The figure shows the evolution of the temperature as the conductivity of the thermal strap increases. It is seen that with a conduction of 0.05 W/K, the batteries have a temperature approximately 10°C colder. A flexible thermal strap seems a good choice because it provides virtually no resistance to small displacements, meaning that no additional mechanical load is applied to the batteries. The thermal conductivity of such a device is given by [27]:

$$GL = \frac{Ak}{L\eta},$$

where L is the length of the flexible strap, η is a coefficient relating the real heat transfer length of threads with L, k is the material's thermal conductivity and A is the cross section. Unfortunately, the coefficient η depends heavily on the geometry of the strap and values are not available. However, seeing the values of conductivity advertised by manufacturers ([60] [61] [62]), it is concluded that a thermal strap having a conductivity of 0.05 W/K is totally feasible.

Nonetheless, such a thermal strap must be used carefully because it will cool down the batteries as long as their temperature is larger than face $-Y$. It means that heat is evacuated

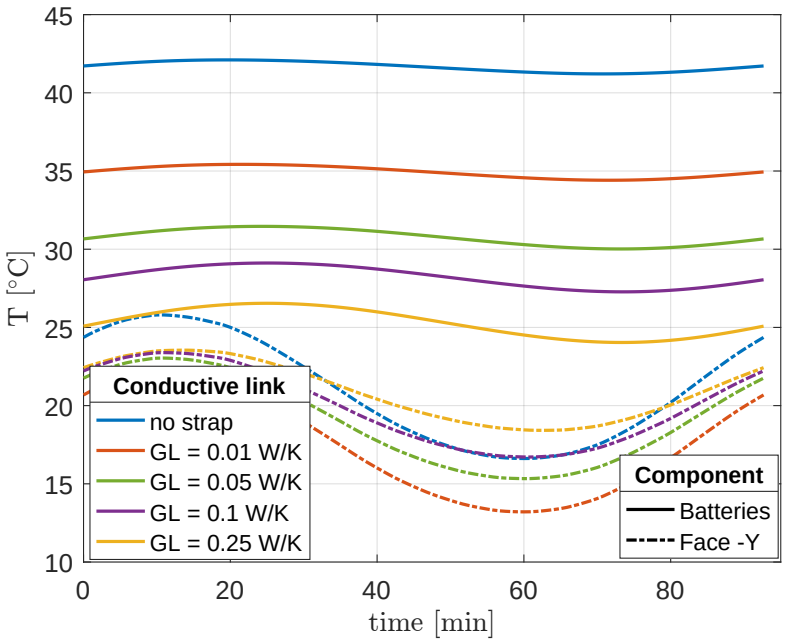

Fig. 6.50: Temperature of the batteries and face $-Y$ of the final design, for the hot ISS orbit.

from the batteries even in the cold case. Moreover, if heaters are used to heat up the batteries during the cold orbits, a part of the power generated will be transferred to the shear panel via the strap and will be wasted. Hence, the heaters will have to work harder (thus consume more electrical power) to maintain a given temperature. This is why a thermal strap between the batteries and face $-Y$ should be a solution of last resort only and studied cautiously by both thermal and electrical subsystems.

It is seen in Tab. 6.6 that the batteries are too cold in the cold case both with and without considering the uncertainties (13.9°C with uncertainties and 4.4°C without) if they are charging. This results was foreseen since the beginning of the thermal design phase because it was chosen to focus on the hot case. The objective was to implement solutions to obtain compliant temperatures in this thermal case. The batteries' temperature can then be risen by heaters depending if they are below the limit value or not. The heaters' study is not conducted in this Master's Thesis but one should be able to implement them in OUFTI-Next. Indeed, having too cold batteries is a recurrent problem in CubeSats. For instance, a similar temperature was reached in OUFTI-1 and two 250 mW heaters have been implemented [36]. Some battery systems also have built-heaters. This is the case of the EPS-battery bundle from Clyde Space [9] which was used to conduct the thermal analysis of OUFTI-Next. However, these heaters have been ignored during the entire study because the selection of the batteries' precise model is not definitive yet.

Element	Requirement		Before thermal design						After thermal design					
			Nominal		Prediction (with uncert)		Margin (with uncert)		Nominal		Prediction (with uncert)		Margin (with uncert)	
	Hot	Cold	Hot	Cold	Hot	Cold	Hot	Cold	Hot	Cold	Hot	Cold	Hot	Cold
Structure	80	-40	45.5	-15.0	56.5	-24.6	23.5	15.4	44.2	-21.0	54.9	-30.8	25.1	9.2
Shear panels	80	-40	67.6	-24.1	81.1	-33.0	-1.1	7.0	63.7	-37.9	76.1	-47.5	3.9	-7.5
Solar cells	125	-55	68.9	-24.4	82.3	-33.3	42.7	21.7	65.1	-24.9	77.4	-34.5	47.6	20.5
S-band patch	45	-25	24.6	-27.6	41.0	-38.9	4.0	-13.9	35.1	-9.6	48.4	-21.5	-3.4	3.5
GPS patch	45	-40	24.5	-27.7	41.0	-39.0	4.0	1.0	23.7	-31.5	39.4	-42.0	5.6	-2
Radiator	-	-	33.1	-13.2	42.8	-22.6	-	-	-11.2	-51.2	-4.5	-57.4	-	-
Batteries (charge)	45	0	49.1	-1.7	60.0	-11.9	-15	-11.9	42.1	-4.4	52.3	-13.9	-7.3	-13.9
Batteries (discharge)	60	-20	49.1	-1.7	60.0	-11.9	0	8.1	42.1	-4.4	52.3	-13.9	7.8	6.1
EPS	60	-20	49.4	-3.4	60.2	-13.5	-0.2	6.5	46.7	-12.7	57.4	-22.9	2.6	-2.9
OBC	65	-25	50.0	-4.5	60.8	-14.6	4.2	10.4	47.2	-12.8	57.9	-23.0	7.1	2.0
VHF/UHF trans.	60	-20	49.9	-5.6	60.7	-15.6	-0.7	4.4	47.1	-13.0	57.9	-23.2	2.1	-3.2
S-band trans.	60	-40	48.8	-6.8	59.6	-16.9	0.4	23.1	46.3	-13.3	57.1	-23.5	2.9	16.5
VHF/UHF ant.	60	-20	46.2	-12.5	57.1	-22.3	2.9	-2.3	45.6	-9.1	56.3	-19.2	3.7	0.8
ADCS	85	-45	48.7	-6.1	59.1	-16.1	25.9	28.9	48.6	-9.0	59.1	-19.0	25.9	26.0
Payload	-	-	35.2	-12.4	45.0	-21.9	-	-	-10.4	-51.2	-3.7	-57.4	-	-

Table 6.6: Comparison of the temperatures [°C] before and after thermal design, with and without uncertainties.
The *Hot* columns refer to the maximum hot temperatures encountered and *Cold* corresponds to the minimum cold ones.

The two other satellite's configurations (*Cross* and *Table*) will be less probably selected for the OUFTI-Next demonstrator. Nonetheless, they have their own advantages and drawbacks. These two shapes have deployable solar panels, thus they are more subject to failure. The main advantage of the *Cross* resides in its very low temperatures for the payload (between -10°C and -50°C without thermal design, see Fig. 6.28). However, the entire platform was constantly below the thermal limit in all cold cases (without considering uncertainties). Hence drastic measures would have to be implemented to heat them up. But this spacecraft's shape produces nearly three times more power that the *Body Mounted* one. Thus larger heaters could be implemented. On the other hand, the *Table* configuration gives similar temperature results as the *Body Mounted* but produces more power.

Conclusion

The goal of this Master's Thesis was to assess the OUFTI-Next mission's feasibility from the thermal point of view. Because of the early stage of the project, the intention was to remain as general as possible. Indeed, the elements composing the satellite were selected because of their representative properties. Moreover, the thermal analysis was conducted on three spacecraft's shapes (*Body Mounted*, *Cross* and *Table*) and three orbits were studied (ISS orbit, 400 km SSO 13h30 LTAN and 800 km SSO 13h30 LTAN).

After briefly recalling the governing principles of heat transfer in space and looking at other spacecraft's thermal strategies, several models of increasing complexity were used to investigate the thermal behaviour of OUFTI-Next. The first one, composed of a few nodes, highlighted the influence of the orbit and spacecraft's shape on the temperature. It showed that the 800 km SSO and ISS orbits are the most demanding because they induce the coldest and hottest temperatures respectively. This basic model also demonstrated that, for a given orbit, the *Body Mounted* configuration leads to the highest thermal load and the *Cross* one to the lowest temperatures. This difference is explained by the fact that the core of the *Cross* shape is constantly in the shadow of the deployable solar panels. Hence, it is never exposed to direct sunlight.

Although the basic model gave access to qualitative thermal behaviours, it was not able to predict the individual components' temperature. For this purpose, the advanced model was constructed. The latter associates each spacecraft's element to at least one node. Out of the three satellite's configurations, the *Body Mounted* one will most probably be selected for OUFTI-Next. Thus, the results of this spacecraft's shape were the most detailed ones. Nonetheless, the main conclusions of the other two ones were also presented.

The analysis of the *Body Mounted* configuration in idle mode showed that several components were out of their thermal range, the main ones being the batteries and the S-band patch antenna. Heat flow maps helped in identifying the thermal power exchanged radiatively and conductively between the different spacecraft's elements. It was deduced that the relatively high temperature of the payload was due to the large amount of power radiated by the other satellite's elements. It was also observed on the maps that a non negligible quantity of power (more than 1.5 W) flowed conductively from the structure to the payload.

In the idle mode, the satellite is constantly pointing its solar panels to the Sun but this orientation does not allow neither imaging nor downlinkind of the scientific data to a ground station. These two operational modes need a specific attitude. The first one requires the payload's aperture to face the ground, while the other one needs the S-band patch antenna to point nadir. The influence of these changes of attitude on the temperature curves of the idle mode were studied by varying the frequency of these events (number of operational orbits per day). The results showed that the communication phase had more impact than the imaging one because it lasted longer (7 minutes for communication and 5 minutes for imaging). However, their effect on the spacecraft's temperature was appreciable only if more than 3 of those operational orbits were made per day. Because OUFTI-Next is a technology demonstrator, the scientific requirements

are flexible. Thus, the project team decided that a few images per day would be enough to prove the good implementation of the mission. Hence, only one imaging plus one communication orbits per day are necessary. In these conditions, the influence of the operational orbits on the idle temperature curves was negligible.

Next, an uncertainty analysis was performed to assess the importance of the assumptions made to build the advanced model. It was conducted by varying the optical properties (absorptance and emittance coefficients), the capacitance and the value of the contact conductances. Taking into account these uncertainties lead to an increase (or decrease) of the maximum (or minimum) temperature from 9°C to 16°C. Therefore, some components which initially fulfilled the thermal requirements were not compliant anymore if these fluctuations were considered. For instance, it was the case of the VHF/UHF dipole antenna module. Obviously, the elements which were initially out of bound increased the gap with the requirements. The batteries were 4.1°C over the maximum allowed temperature in the hot case without uncertainties. Taking them into account, this value increased to 15°C.

The last part of this document was dedicated to the thermal design of the *Body Mounted* configuration. Its goal was to modify the initial model in order to achieve compliant temperatures for all the components. The initial aluminum spacers were replaced by a combination of Nylon washers and titanium spacers, which resulted in reducing greatly the conductive link between different elements. Hence, the power flowing from the EPS circuit board to the batteries dramatically decreased, resulting in colder batteries. In a similar way, the new spacer/washer design reduced the conductive thermal power going from the structure to the payload. Using them had the additional consequence on the dipole antenna of reducing the temperature amplitude variation of the module.

It was also decided to use Nylon washers between the radiator and the structure, which induced a decrease of its temperature. A colder radiator allows to extract heat from the payload more effectively. The S-band patch antenna's temperature was increased by using the same Nylon washers as the radiator. Coating the component with chromacoat aluminum paint also contributed to increase its temperature.

The overall spacecraft's temperature was decreased by replacing the initial alodined aluminum coating of the external faces of the shear panels with a S-13G-LO white silicon paint. This modification induced a temperature drop of approximately 10°C for both the payload and the batteries.

The last modification aimed to reduce the radiative heat received by the payload from the other spacecraft's components. A radiative shield made of thin aluminum panels coated with gold, surrounding completely the payload, implemented.

Finally, all these design changes lead to compliant temperatures for all the elements except for the batteries which were still 4.4°C too cold in the cold case. The objective of reducing the payload's temperature was also met, since it varies between -10°C and -51°C, which is more than 40°C colder than the initial model. By considering the uncertainties on the final design model, the conclusions changed slightly. Indeed, these uncertainties pushed several components out of their allowable thermal range, although by only 3°C at the most. Thus it was not judged necessary to further improve the model.

The thermal design procedure was not applied to the *Cross* and *Table* configurations because they will probably not be selected for the satellite. Nonetheless, they have their advantages. The first one induces a spacecraft's core much colder than the *Body Mounted*. For instance, the payload's temperature ranges between -10°C and -50°C without any thermal design change. Hence implementing the same golden radiative shield and new spacer's design could potentially lead to even lower temperatures. However, this satellite's shape presents the significant disadvantage

of inducing a cold temperature on the platform. Indeed, most of the electronic components were too cold to operate safely, even without considering uncertainties. On the other hand, the *Table* configuration led to similar temperatures as the *Body Mounted* shape but produced more electrical power.

It is important to remind that all the results of this thesis were obtained by considering the worst case approach. For example, the cold case assumed that there was absolutely no internal power dissipation while the hot one was achieved when all the collected power was dissipated. Hence, in practice, these two situations will rarely be encountered (unless in case of failure of all the solar cells $\Rightarrow$ no power available to be dissipated by the other components, or in case of malfunctioning of the EPS $\Rightarrow$ too much power distributed to the electrical components leading to an increased dissipation). Instead, a nominal situation would correspond to a moderate internal dissipation and to moderate environment parameters. This would lead to temperature curves located between the cold and hot ones.

Obviously, further investigation is still required. Heaters must be implemented to heat up the batteries when necessary. This system has to be studied by both thermal and electrical engineers to ensure that it does not drain too much power. The elements of the satellite also have to be definitively chosen. Then, more accurate information should be gathered from the manufacturers. This will reduce the uncertainties on the thermal properties. Finally, thermal testing should be conducted to assess the performance of the models by comparing the temperatures obtained by computer simulation to the measured ones.

Appendix

A Dimensions of a 3U CubeSat

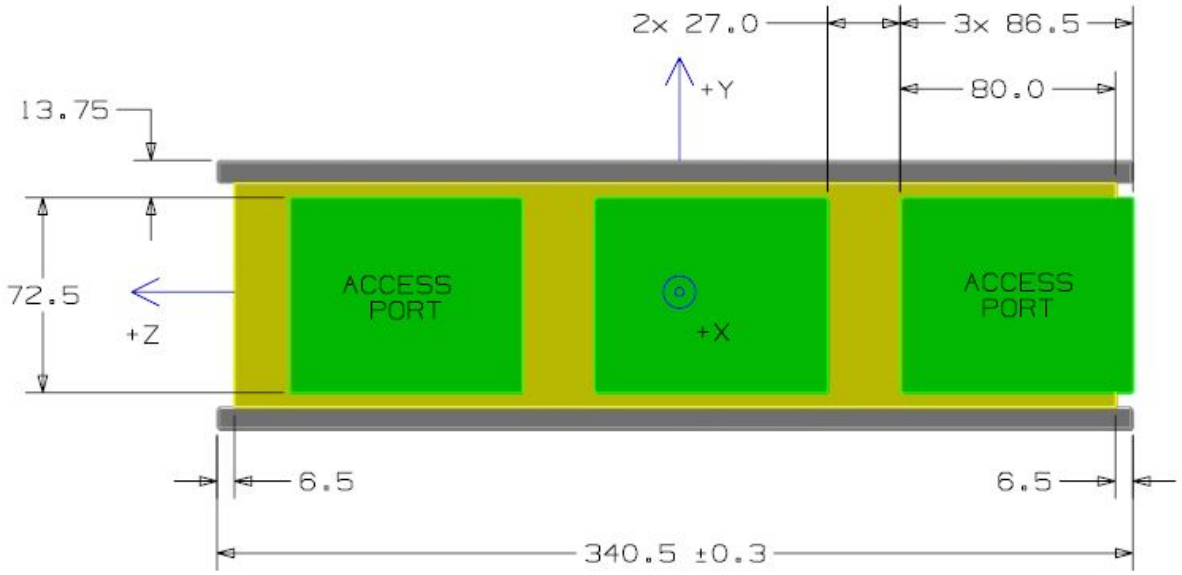

Fig. A.1: Dimensions [mm] of a 3U CubeSat according to the CubeSat Design Specification [44].

B Sun pointing of the Body Mounted configuration

Fig. B.1 illustrates the search of the optimal pointing attitude for the *Body Mounted* configuration to achieve a maximum electrical power production. As a reminder, faces $+X$, $+Y$ and $+Z$ are covered with solar cells.

Since faces $+X$ and $+Y$ are covered by the same amount of solar cells, it is known that the optimal orientation is obtained if the azimuth angle θ is 45°. The only remaining unknown of the problem is thus the elevation angle γ. However, the power produced is dependant of the angle between the normal of the panel and the Sun direction, which is Ω for faces $+X$ and $+Y$ and $90° - \gamma$ for $+Z$. Hence, the electrical power is given by:

$$Q = 2A_{3U}C_S\eta\cos\Omega + A_{1U}C_S\eta\cos\left(90° - \gamma\right) .$$

Knowing that $\theta = 45°$, one obtains easily the relation linking Ω and γ such that $\cos\Omega = \sqrt{\frac{1-\sin^2\gamma}{2}}$. The optimal attitude is then computed by introducing this relation in the previous one and taking

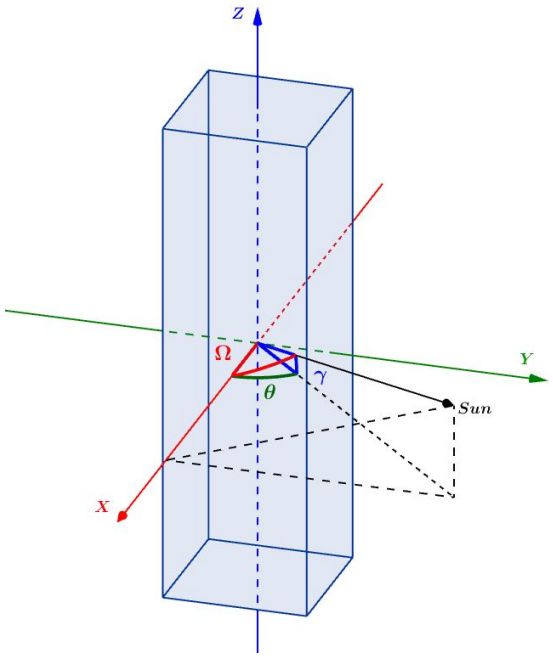

Fig. B.1: Optimal sun pointing of the *Body Mounted* configuration.

into account that $A_{3U} = 3A_{1U}$. Finally, one finds $\gamma_{opt} = \arctan\left(\sqrt{2}/6\right)$, which corresponds to the Sun located in $[1,\ 1,\ 1/3]$, in the satellite's axes.

C Convergence of the Monte Carlo Ray Tracing

A convergence analysis of the MCRT is displayed in Fig. C.1 for three different seeds and an increasing number or rays. This study is done on the radiative exchange factor between the EPS board and the OBC. It can be seen that an error of less than 0.5% is achieved if 10000 rays (or more) are used.

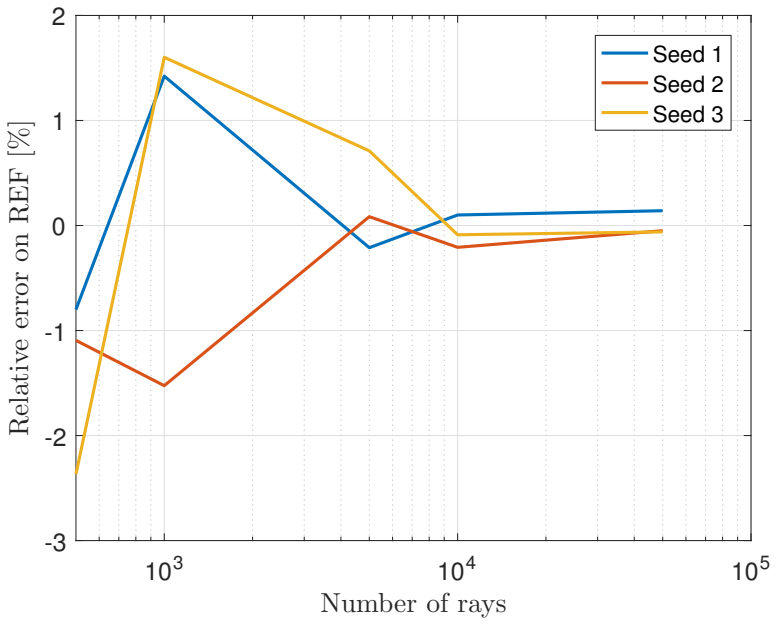

Fig. C.1: Convergence analysis of the radiative exchange factor between EPS and OBC.

To improve the confidence in the results, this REF is also calculated analytically. However, for this manual computation, it is assumed that the two PCBs have a 10×10 cm^2 surface area. In this situation, the problem is similar to a flat cuboid enclosure where the four sides are the portions of shear panels seen by the PCBs, the top is the EPS board and the bottom is the OBC.

The radiative exchange factor is thus given by the following relation, where A is the surface of the PCB and $B_{i,j}$ is the Gebhart factor :

$$GR_{\text{EPS,OBC}} = \epsilon_{\text{EPS}} A_{\text{EPS}} B_{\text{EPS,OBC}} \,.$$

The Gebhart factor is defined as:

$$B_{i,j} = F_{i,j}\epsilon_j + \sum_k F_{i,k} \left(1 - \epsilon_k\right) B_{k,j}$$

This relation can be written in matrix form

$$\mathbf{B} = \boldsymbol{\beta} + \left(\mathbf{F} - \boldsymbol{\beta}\right)\mathbf{B} \quad \Leftrightarrow \quad \left(\mathbf{I} - \mathbf{F} + \boldsymbol{\beta}\right)\mathbf{B} = \boldsymbol{\beta} \,,$$

where $\beta_{i,j} = F_{i,j}\epsilon_j$ and $\mathbf{I}$ is the identity matrix.

Provided that the view factors between all the surfaces are known, the Gebhart factors can easily be determined from this last expression. The view factor between two identical, parallel and directly opposed rectangles (Fig. C.2) is computed by:

$$F_{A_1,A_2} = \frac{2}{\pi XY}\left[\ln\left(\frac{(1+X^2)(1+Y^2)}{1+X^2+Y^2}\right)^{1/2} + X\sqrt{1+Y^2}\arctan\frac{X}{\sqrt{1+Y^2}} + Y\sqrt{1+X^2}\arctan\frac{Y}{\sqrt{1+X^2}} - X\arctan X - Y\arctan Y\right],$$

with $X = a/c$ which is the ratio of the dimensions of the rectangle and $Y = b/c$ is the ratio of one side of the rectangle over the distance separating them.

On the other hand, two rectangles having a common edge and forming a 90° angle (Fib. C.3) see each other following this relation:

$$F_{A_1,A_2} = \frac{1}{\pi W}\left[W\arctan\frac{1}{W} + H\arctan\frac{1}{H} - \sqrt{H^2+W^2}\arctan\sqrt{\frac{1}{H^2+W^2}} + \frac{1}{4}\ln\left(\frac{(1+W^2)(1+H^2)}{1+W^2+H^2}\left(\frac{W^2(1+W^2+H^2)}{(1+W^2)(W^2+H^2)}\right)^{W^2}\left(\frac{H^2(1+H^2+W^2)}{(1+H^2)(H^2+W^2)}\right)^{H^2}\right)\right],$$

where $H = h/l$ and $W = w/l$ respectively the ratios of one of the rectangles' length over the common edge.

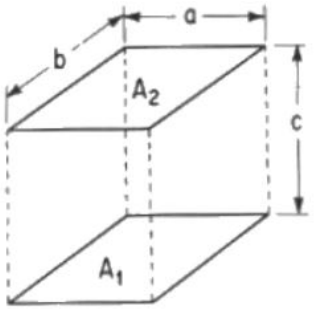

Fig. C.2: View factor between parallel identical rectangles [63]

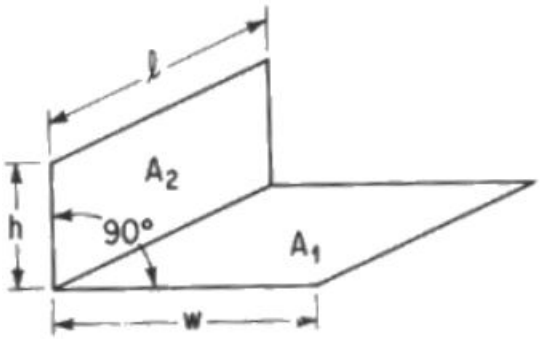

Fig. C.3: View factor between perpendicular rectangles having a common edge [63]

Analytically, a radiative exchange factor of $6.4553 \cdot 10^{-3}$ m^2 is obtained. If 10 000 rays are used for the MCRT method, the average of the three seeds gives $GR_{\mathrm{EPS,OBC}} = 5.4071 \cdot 10^{-3}$ m^2. This difference of 15% between the two methods is explained by the fact that the ESATAN model uses the real sizes of the PCBs (9.5×9 cm^2 for the EPS and 9.6×9 cm^2 for the OBC), while the analytic one assumes a 10×10 cm^2 to facilitate the view factor computation. In fact, if this size is used in the ESATAN model, one finds a REF of 6.4919 m^2, which is only 0.5% larger than the analytic value. This result proves the good implementation of the radiative model.

D Additional results of the advanced thermal model

D.1 Body Mounted configuration

The temperature curves of the PCB stack, the ADCS and the VHF/UHF dipole antenna module are shown from Fig. D.1 to Fig. D.4. It is seen that they all fit their requirements (see Tab. D.1) for the three orbits and two thermal cases.

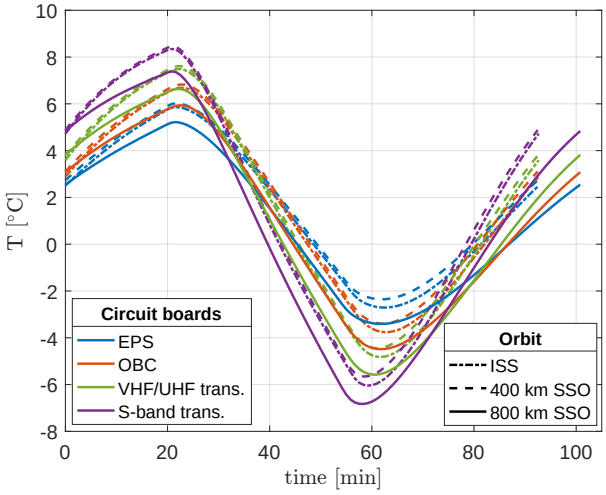

Fig. D.1: Temperature of the PCB stack *Body Mounted* configuration, cold case.

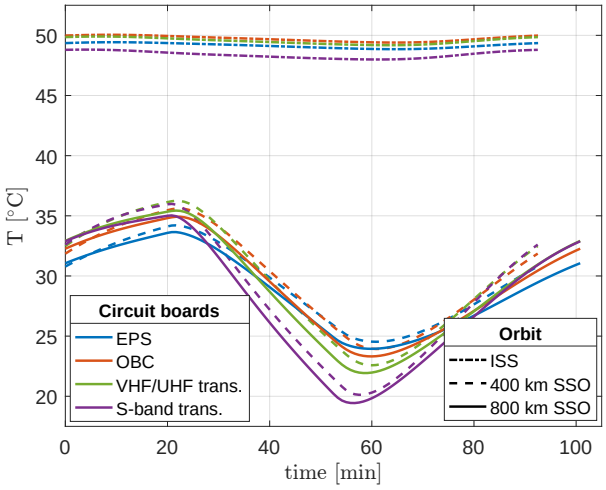

Fig. D.2: Temperature of the PCB stack *Body Mounted* configuration, hot case.

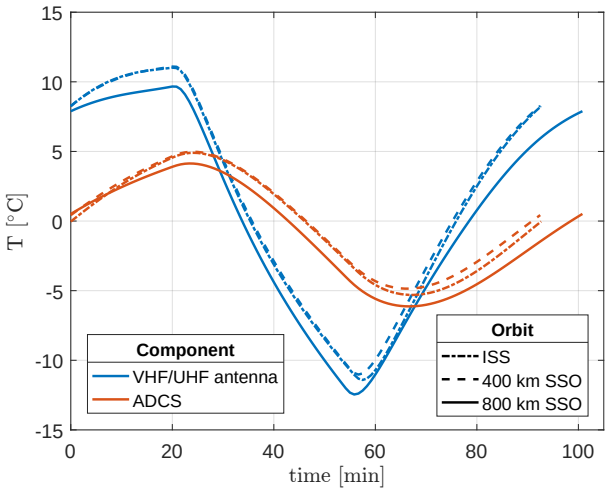

Fig. D.3: Temperature of the ADCS and VHF/UHF antenna module *Body Mounted* configuration, cold case.

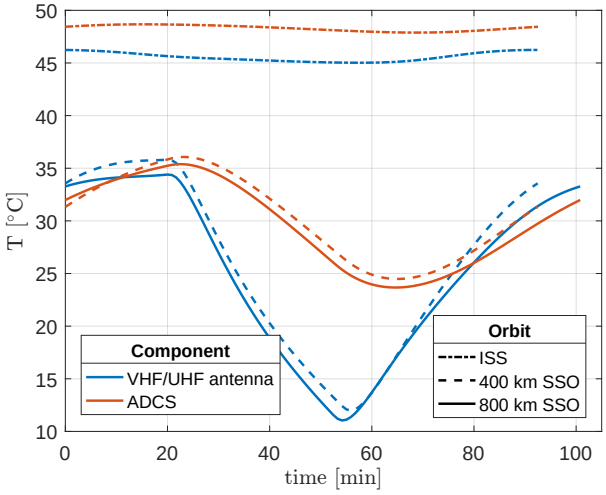

Fig. D.4: Temperature of the ADCS and VHF/UHF antenna module *Body Mounted* configuration, hot case.

D.2 Cross configuration

Solar cells

The average, minimum and maximum temperature of the solar cells is represented in Fig. D.5 and Fig. D.6 by solid, dotted and dashed lines respectively. It is seen that the thermal requirements

Component	Thermal range [°C]
EPS PCB	-20 to 60
OBC PCB	-25 to 65
VHF/UHF transceiver PCB	-20 to 60
S-band transceiver PCB	-40 to 60
ADCS	-45 to 85
VHF/UHF antenna module	-20 to 60

Table D.1: Recall of the thermal requirements of some components.

are respected for all the orbits and thermal cases combinations, except for the cold 800 km SSO where the temperature can be 2°C too cold. However, this situation occurs only during 2.5 minutes at the end of the eclipse period. It is thus judged acceptable.

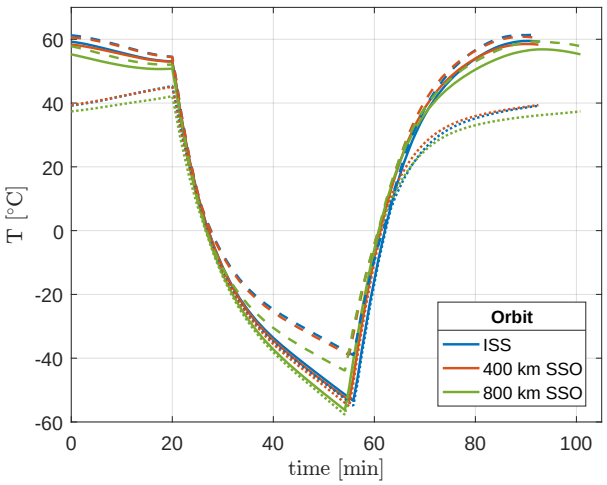

Fig. D.5: Temperature of the solar cells *Cross* configuration, cold case.

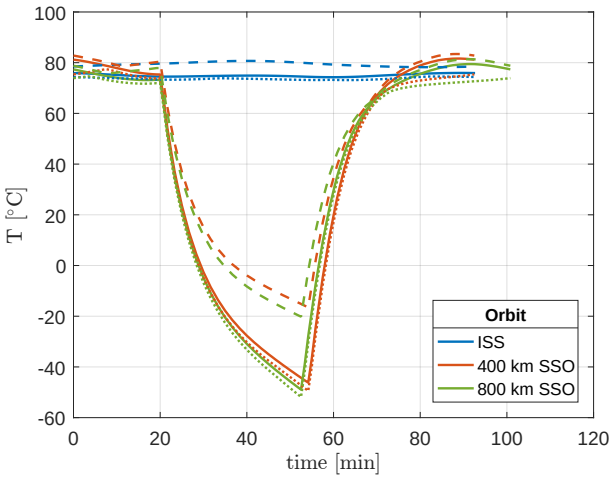

Fig. D.6: Temperature of the solar cells *Cross* configuration, hot case.

Structure, shear panels and deployable panels

The shear panels' temperature (mean, minimum and maximum) is represented in Fig. D.7, while Fig. D.8 is dedicate to the structure ('+' markers) and the deployable panels. It is seen that the structure and shear panels fit their thermal requirements (from -40°C to 80°C). The deployable panels can become too cold at the end of the eclipse period. However, it has already been explained in Section 6.2.2 that it is not a problem.

PCB stack and ADCS

Fig. D.9 proves that all the circuit boards forming the PCB stack fit their thermal requirements in the hot case for the *Cross* configuration.

On the other hand, the ADCS allows temperature ranging from -45°C to 85°C. Fig. D.10 shows that the majority of orbit and thermal cases combination are compliant with this thermal requirement. In fact, only the cold 800 km SSO oscillates around the lower bound of the requirements.

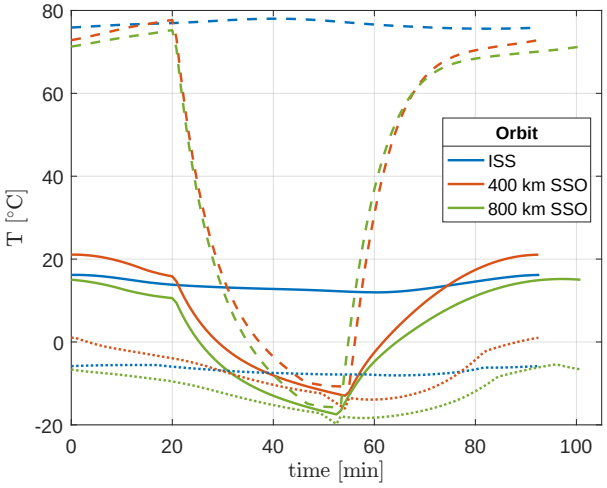

Fig. D.7: Temperatures of the shear panels *Cross* configuration, hot case.

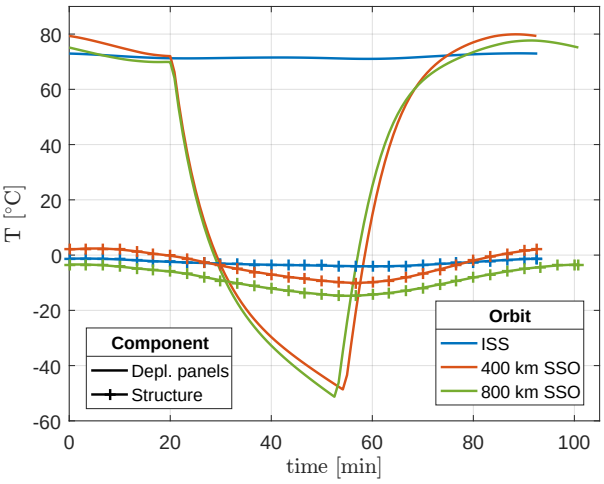

Fig. D.8: Temperatures of the structure and deployable panels - *Cross* configuration, hot case.

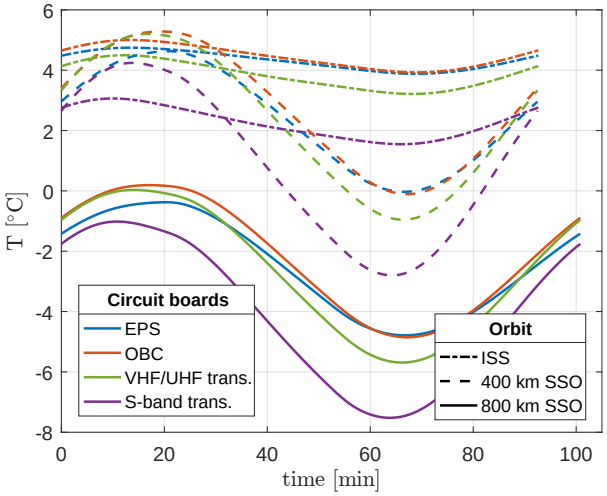

Fig. D.9: Temperatures of the PCB stack *Cross* configuration, hot case.

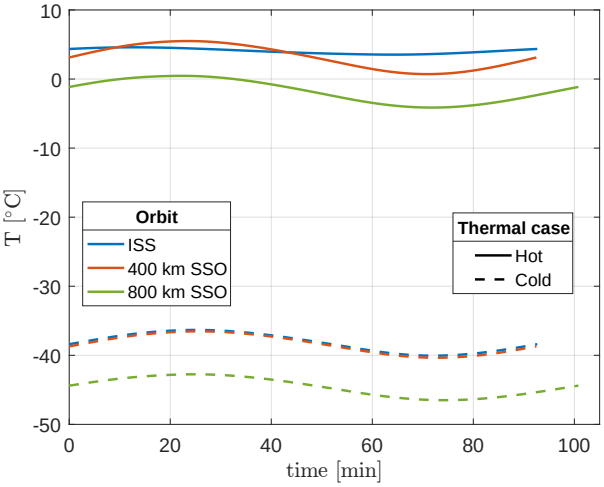

Fig. D.10: Temperatures of the ADCS *Cross* configuration.

D.3 Table configuration

Solar cells

The solar cells' temperature is presented in Fig. D.11 and Fig. D.12 for the cold and hot cases. The solid lines correspond to their mean temperature, while the dotted and dashed ones are associated to their minimum and maximum temperatures respectively. It can be seen that all the curves respect the thermal requirements (from -55°C to 125°C).

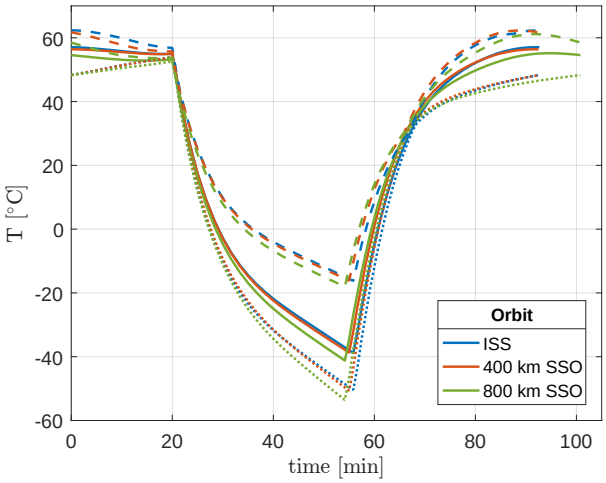

Fig. D.11: Temperatures of the solar cells *Table* configuration, cold case.

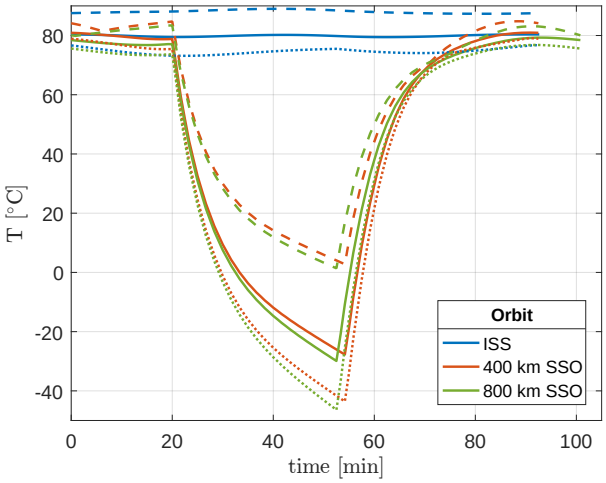

Fig. D.12: Temperatures of the solar cells *Table* configuration, hot case.

Structure, shear panels and deployable panels

Fig. D.13 and Fig. D.14 show the temperature of the structure ('+' markers) and the deployable panels. Even if the latter are composed of several nodes, only the average temperature is displayed in the figures because these panels have the same shape and orientation. They thus have the same temperature and the minimum and maximum curves would be very close to each other. It is seen that the allowed temperature range (from -40°C to 80°C) is not strictly respected for all the orbits. However, as explained in Section 6.2.2, this is not a problem from the structural integrity's point of view. Only the alignment changes due to thermal expansion would have to be looked at.

The average, minimum and maximum temperatures of the shear panels are presented in Fig. D.15 and Fig. D.16. One sees that these components respect their thermal requirements except for the maximum temperature curve of the ISS orbit. In this case, the shear panels are 5°C to 7°C too hot. Nonetheless, it remains acceptable and once again, only the alignment problems should be addressed.

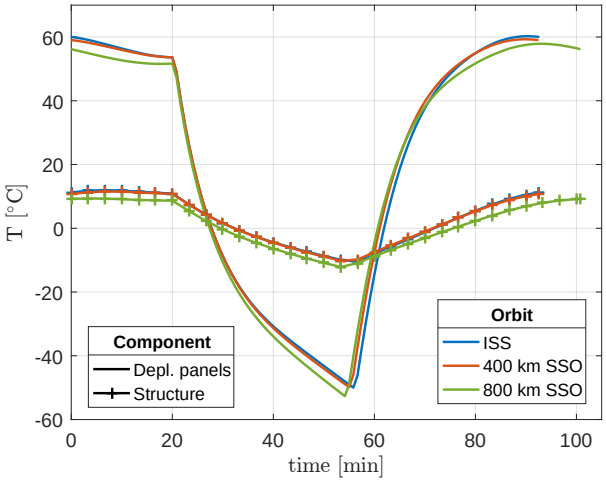

Fig. D.13: Temperatures of the structure and deployable panels - *Table* configuration, cold case.

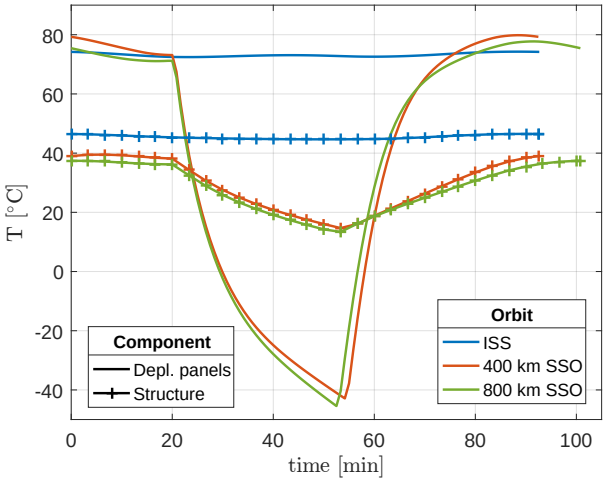

Fig. D.14: Temperatures of the structure and deployable panels - *Table* configuration, hot case.

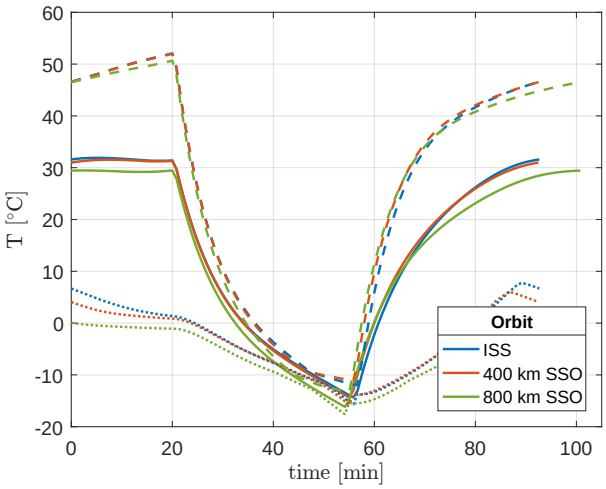

Fig. D.15: Temperatures of the shear panels *Table* configuration, cold case.

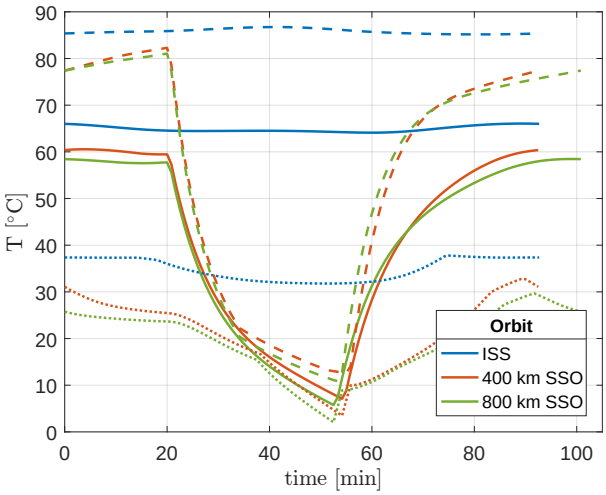

Fig. D.16: Temperatures of the shear panels *Table* configuration, hot case.

PCB stack

Fig. D.17 and Fig. D.18 display the temperature of the circuit boards forming the PCB stack for cold and hot cases respectively. From these curves, it is deduced that the *Table* configuration provides acceptable temperatures to these components for every orbit and thermal case combination.

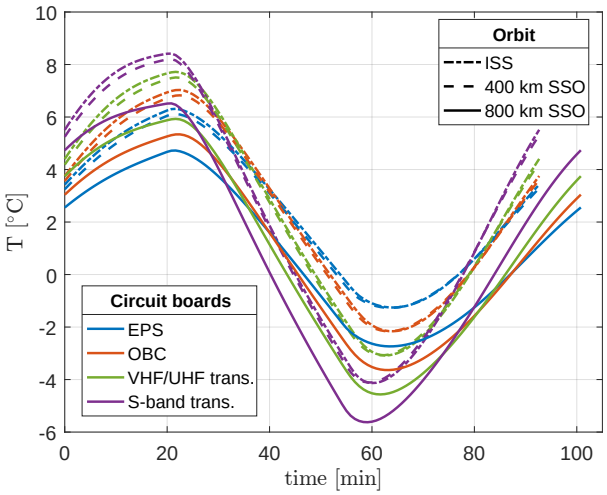

Fig. D.17: Temperatures of the PCB stack *Table* configuration, cold case.

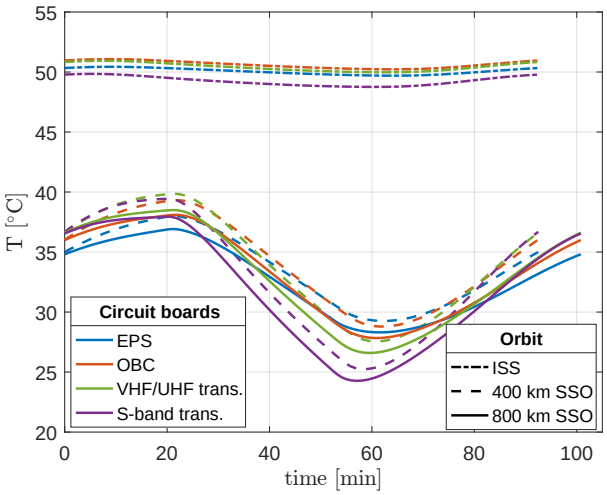

Fig. D.18: Temperatures of the PCB stack *Table* configuration, hot case.

ADCS and VHF/UHF dipole antenna module

These two components have their temperatures represented in Fig. D.19 and Fig. D.20, where it can be seen that they fit their thermal requirements for all orbits (-45°C to 85°C for the ADCS and -20°C to 60°C for the dipole antenna).

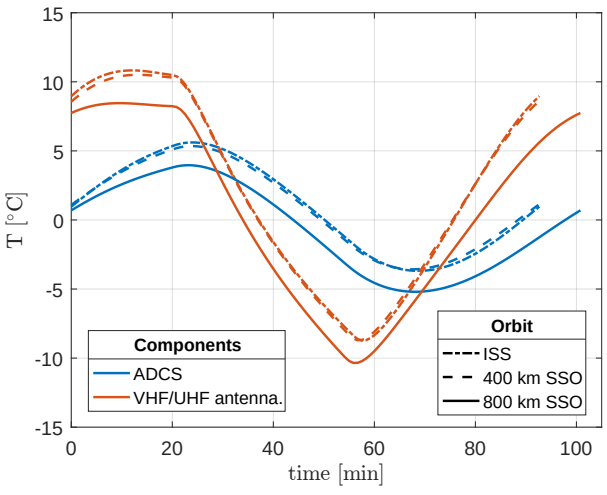

Fig. D.19: Temperatures of the ADCS and VHF/UHF antenna module - *Table* configuration, cold case.

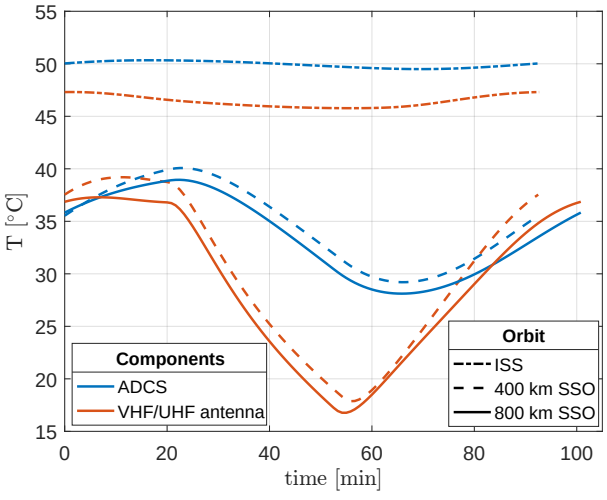

Fig. D.20: Temperatures of the ADCS and VHF/UHF antenna module - *Table* configuration, hot case.

E Precision concerning the operational orbits' frequency

Fig E.1 shows the temperature curve of the bottom shear panel of the *Body Mounted* configuration for the cold 800 km SSO. The figure displays the temperature for an observing frequency of 3 orbits per day (1 observing orbit followed by 4 idle orbits $\Rightarrow freq = 15/(1+4)$). The end of each orbit is represented by vertical black dashed lines. The light blue zone represents the imaging period of the observation orbit.

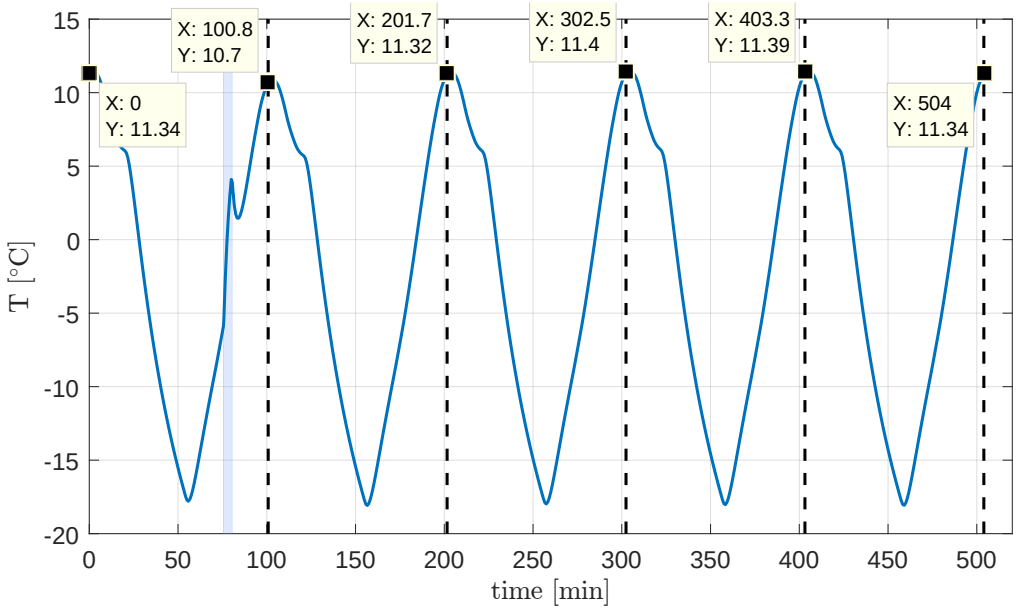

Fig. E.1: Temperature of the bottom shear panel of the *Body Mounted* configuration for the cold 800 km SSO. 1 imaging orbit followed by 4 idle ones (frequency of 3 imaging orbits per day).

It is seen that the cyclic conditions (same temperature and temperature slope at the beginning and at the end) are respected on the entire cycle of 5 orbits. It results that the individual orbits have different start and end temperatures. In Section 6.3, only the first three orbits would have been displayed.

F Additional information for the uncertainty analysis

The workflow of the uncertainty analysis is described in Fig. F.1 for an element i of the satellite. For a given orbit, the nominal minimum and maximum temperatures are extracted ($\mathrm{T}_{Nom,H,min}$ and $\mathrm{T}_{Nom,H,max}$ respectively in the case of the hot orbit). Then, the thermal model is run with one of the six uncertainties. Once they all have been taken into account, one can compute the temperature difference (e.g. $\Delta T_{H,max,i}$ for the uncertainty on $\mathrm{T}_{Nom,H,max}$) by the square root of the square of the temperature differences. Then, the *hot max* and *cold min* uncertainties presented in Tab. 6.2 are obtained by taking the maximum or minimum of the four ΔT.

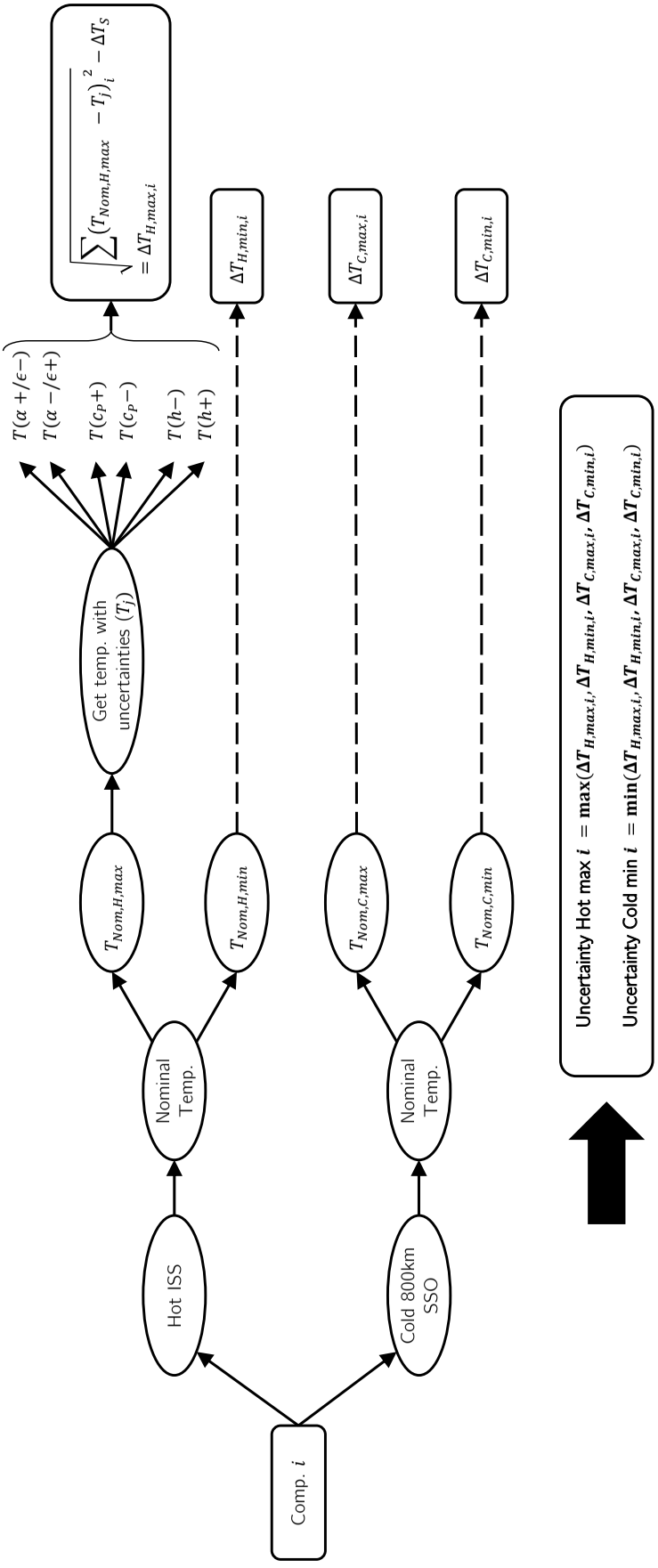

Fig. F.1: Workflow of the uncertainty analysis for a component i.

Tab. F.1 to Tab. F.4 show the uncertainties acting separately on the minimum and maximum components' temperature for the hot ISS orbit and cold 800 km SSO. In these tables, the second column corresponds to the temperature reached in the nominal case. The next six ones are the ΔT_j produced when the uncertainty j is considered alone and the last column is the total uncertainty on the nominal temperature which takes into account the systematic uncertainty of 3 K.

It is seen that increasing the absorptance and reducing the emittance ($\alpha+/\epsilon-$) always lead to higher temperatures. This modification of optical properties has the most constant influence on all the components by changing their temperature by 5°C to 6°C. On the other hand, the change of capacitance has the smallest effect. It does not exceed 0.3°C in the hot case and 2.5°C in the cold one. An increase in the capacitance (c_P+) lead to a higher thermal inertia and thus the temperature curves get flatter. This is why the nominal maximum temperatures are reduced, while the nominal minimum ones are increased.

Component	$\mathbf{T}_{max,nom}$	$\alpha+/\epsilon-$	$\alpha-/\epsilon+$	c_P+	c_P-	$h+$	$h-$	$\sqrt{\sum \Delta T_j^2}+\Delta T_S$
Structure	45.5	5.6	-5.2	-0.1	0.1	0.3	-1.2	10.8
Shear panels	67.6	6.4	-6.1	-0.2	0.1	-1.8	3.3	12.6
Solar cells	68.9	6.4	-6.1	-0.2	0.2	-1.8	3.2	12.5
S-band patch	24.6	4.5	-4.2	-0.4	0.4	4.2	-7.2	13.4
GPS patch	24.5	4.5	-4.2	-0.4	0.4	4.2	-7.2	13.4
Radiator	33.1	4.5	-4.3	-0.1	0.1	0.9	-1.3	9.5
Batteries	49.1	5.6	-5.3	-0.1	0.1	0.3	-1.0	10.8
EPS	49.4	5.6	-5.3	-0.0	0.1	0.3	-1.0	10.8
OBC	50.0	5.6	-5.3	-0.0	0.1	0.3	-1.0	10.8
VHF/UHF trans.	49.9	5.6	-5.3	-0.1	0.1	0.3	-1.0	10.8
S-band trans.	48.8	5.6	-5.3	-0.1	0.1	0.3	-1.1	10.8
VHF/UHF ant.	46.2	5.5	-5.2	-0.1	0.1	0.3	-1.1	10.7
ADCS	48.7	5.3	-4.9	-0.1	0.1	0.4	-1.0	10.3
Payload	35.2	4.6	-4.3	-0.1	0.1	0.8	-1.2	9.5

Table F.1: Uncertainty on T_{max}, hot ISS orbit [°C].

Component	$\mathbf{T}_{max,nom}$	$\alpha+/\epsilon-$	$\alpha-/\epsilon+$	c_P+	c_P-	$h+$	$h-$	$\sqrt{\sum \Delta T_j^2}+\Delta T_S$
Structure	44.1	5.5	-5.2	0.0	-0.0	0.3	-1.2	10.6
Shear panels	26.3	4.9	-4.7	0.3	-0.3	0.2	-2.4	10.3
Solar cells	26.3	4.9	-4.7	0.3	-0.3	0.2	-2.4	10.2
S-band patch	11.5	4.8	-4.5	0.2	-0.2	6.1	-10.0	16.4
GPS patch	11.5	4.8	-4.5	0.2	-0.2	6.1	-10.0	16.4
Radiator	31.3	4.6	-4.3	0.1	-0.1	1.0	-1.3	9.5
Batteries	48.6	5.6	-5.3	0.1	-0.1	0.3	-1.0	10.8
EPS	48.9	5.6	-5.3	0.0	-0.1	0.3	-1.0	10.8
OBC	49.4	5.6	-5.3	0.0	-0.1	0.3	-1.0	10.8
VHF/UHF trans.	49.2	5.6	-5.3	0.0	-0.1	0.3	-1.0	10.7
S-band trans.	48.0	5.5	-5.2	0.0	-0.1	0.3	-1.0	10.7
VHF/UHF ant.	45.0	5.5	-5.2	0.0	-0.0	0.3	-1.1	10.6
ADCS	47.9	5.3	-4.9	0.1	-0.1	0.4	-1.0	10.3
Payload	34.0	4.6	-4.4	0.1	-0.1	0.9	-1.2	9.5

Table F.2: Uncertainty on T_{min}, hot ISS orbit [°C].

Concerning the contact conductance, the effect of this uncertainty parameter depends on the element of the spacecraft. Some of them have many bolts (e.g. structure, shear panels, patch antennas, ...) and are more affected than others.

Component	$\mathbf{T}_{max,nom}$	$\alpha+/\epsilon-$	$\alpha-/\epsilon+$	c_P+	c_P-	$h+$	$h-$	$\sqrt{\sum \Delta T_j^2} + \Delta T_S$
Structure	10.6	5.5	-5.3	-0.7	1.0	0.5	-1.6	11.0
Shear panels	35.6	6.8	-6.5	-0.9	1.0	-2.1	3.9	13.5
Solar cells	36.9	6.8	-6.5	-0.9	1.0	-2.0	3.8	13.4
S-band patch	-6.2	4.8	-4.6	-1.0	1.1	3.5	-6.3	12.9
GPS patch	-6.2	4.8	-4.6	-1.0	1.1	3.5	-6.3	12.9
Radiator	-4.5	4.5	-4.4	-0.9	1.3	1.2	-1.6	9.8
Batteries	3.7	5.2	-5.0	-0.7	1.1	0.3	-1.1	10.4
EPS	5.2	5.3	-5.0	-0.7	1.1	0.4	-1.2	10.5
OBC	5.9	5.3	-5.1	-0.7	1.1	0.4	-1.2	10.6
VHF/UHF trans.	6.6	5.3	-5.1	-0.8	1.1	0.4	-1.3	10.6
S-band trans.	7.4	5.4	-5.1	-0.8	1.1	0.4	-1.3	10.7
VHF/UHF ant.	9.7	5.5	-5.3	-0.8	1.1	0.5	-1.5	10.9
ADCS	4.1	5.1	-4.9	-1.0	1.5	0.5	-1.3	10.4
Payload	-3.0	4.5	-4.4	-0.9	1.3	1.0	-1.5	9.7

Table F.3: Uncertainty on T_{max}, cold 800 km SSO [°C].

Component	$\mathbf{T}_{max,nom}$	$\alpha+/\epsilon-$	$\alpha-/\epsilon+$	c_P+	c_P-	$h+$	$h-$	$\sqrt{\sum \Delta T_j^2} + \Delta T_S$
Structure	-15.0	4.3	-4.1	1.9	-2.4	0.0	-0.0	9.7
Shear panels	-24.1	3.4	-3.3	1.4	-1.7	0.1	-2.8	8.9
Solar cells	-24.4	3.4	-3.3	1.4	-1.7	0.1	-2.8	8.9
S-band patch	-27.6	4.0	-3.8	1.8	-2.2	2.6	-4.7	11.2
GPS patch	-27.7	4.0	-3.8	1.8	-2.2	2.7	-4.7	11.3
Radiator	-13.2	4.3	-4.1	1.2	-1.8	0.6	-0.9	9.4
Batteries	-1.7	5.0	-4.8	0.8	-1.3	0.3	-0.8	10.1
EPS	-3.4	4.9	-4.7	1.0	-1.5	0.2	-0.7	10.1
OBC	-4.5	4.9	-4.6	1.2	-1.7	0.2	-0.6	10.1
VHF/UHF trans.	-5.6	4.8	-4.6	1.3	-1.8	0.2	-0.6	10.0
S-band trans.	-6.8	4.8	-4.5	1.5	-2.0	0.2	-0.5	10.0
VHF/UHF ant.	-12.5	4.4	-4.2	1.9	-2.5	0.1	-0.2	9.9
ADCS	-6.1	4.7	-4.4	1.4	-2.1	0.3	-0.7	10.0
Payload	-12.4	4.3	-4.1	1.2	-1.8	0.5	-0.8	9.4

Table F.4: Uncertainty on T_{min}, cold 800 km SSO [°C].

G Results of the thermal design

The following graphs show the results of the final thermal design for the *Body Mounted (BM)* configuration. The components have their temperature represented for all the orbits (800 km SSO, 400 km SSO and ISS orbits) and thermal cases. For all the figures, the solid lines refer to the hot thermal cases, while the dashed ones correspond to the cold cases. Moreover, when a component is composed of several nodes (this is the case of the shear panels and solar cells), only the average temperature is given.

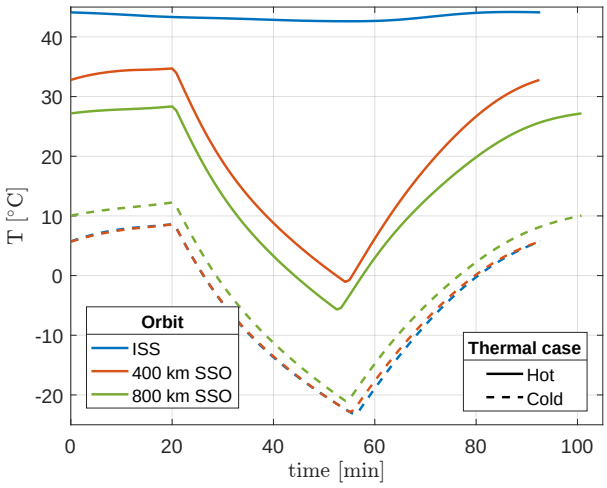

Fig. G.1: Temperatures of the structure - *Body Mounted* configuration, final design.

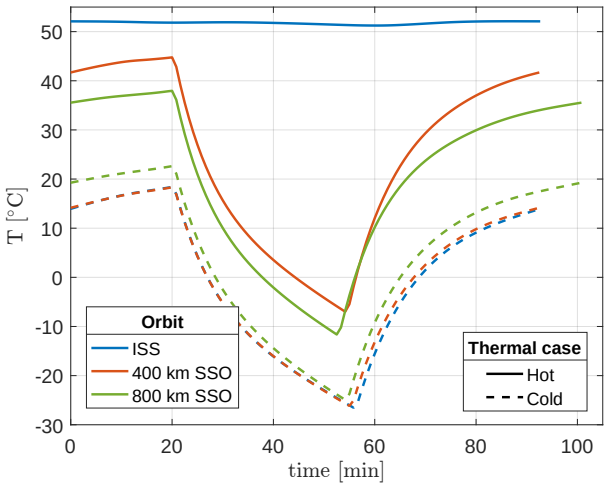

Fig. G.2: Temperatures of the shear panels - *Body Mounted* configuration, final design.

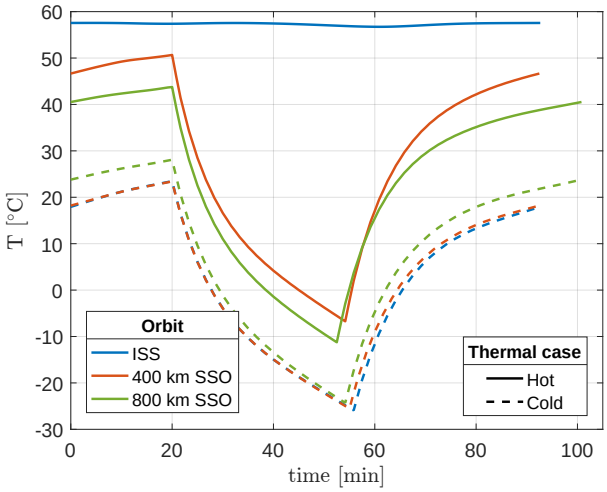

Fig. G.3: Temperatures of the solar cells - *BM* configuration, final design.

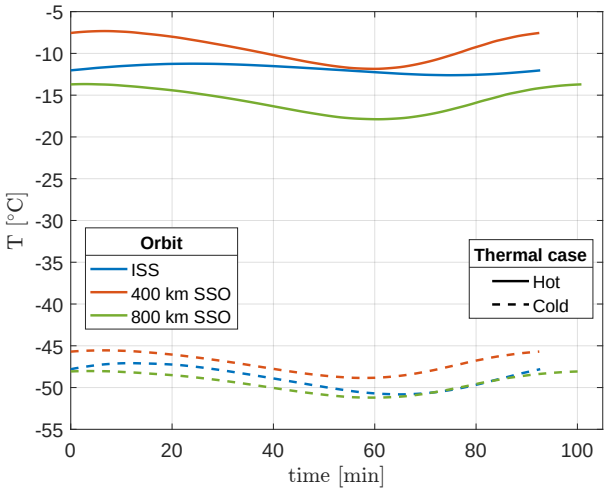

Fig. G.4: Temperatures of the radiator - *BM* configuration, final design.

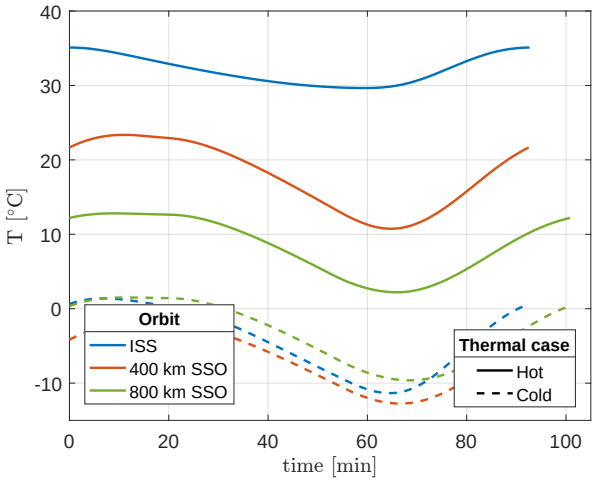

Fig. G.5: Temperatures of the S-band patch antenna - *BM* configuration, final design.

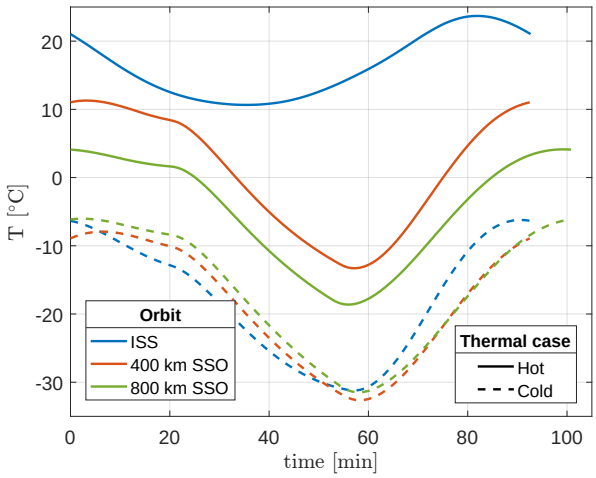

Fig. G.6: Temperatures of the GPS patch antenna - *BM* configuration, final design.

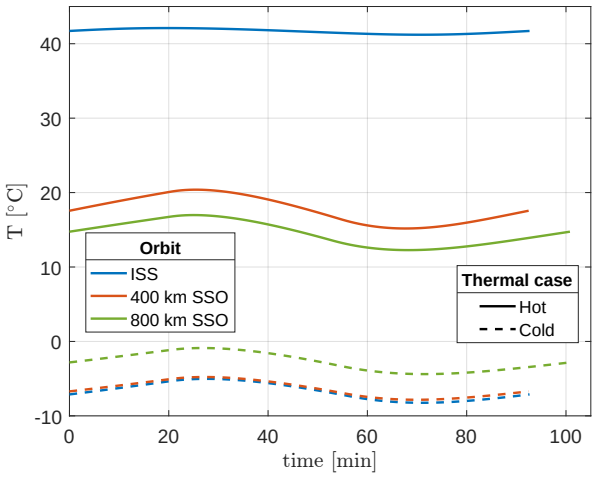

Fig. G.7: Temperatures of the batteries - *BM* configuration, final design.

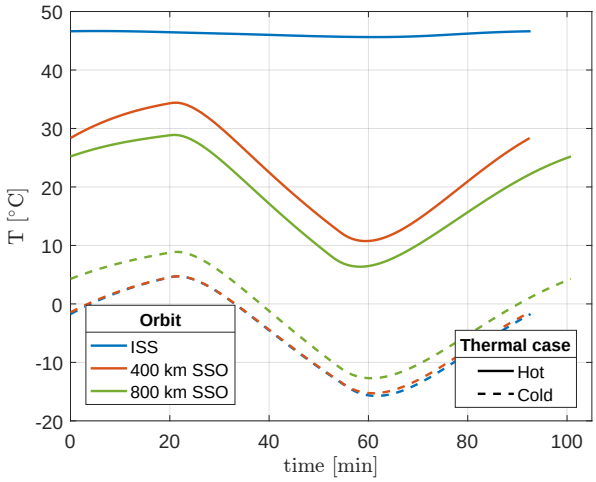

Fig. G.8: Temperatures of the EPS - *BM* configuration, final design.

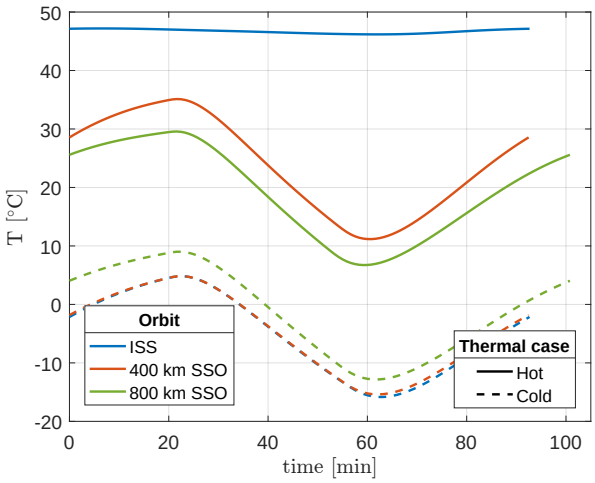

Fig. G.9: Temperatures of the OBC - *BM* configuration, final design.

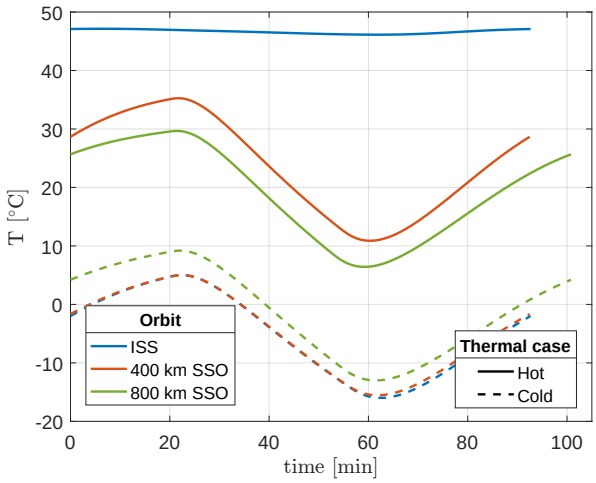

Fig. G.10: Temperatures of the VHF/UHF transceiver - *BM* configuration, final design.

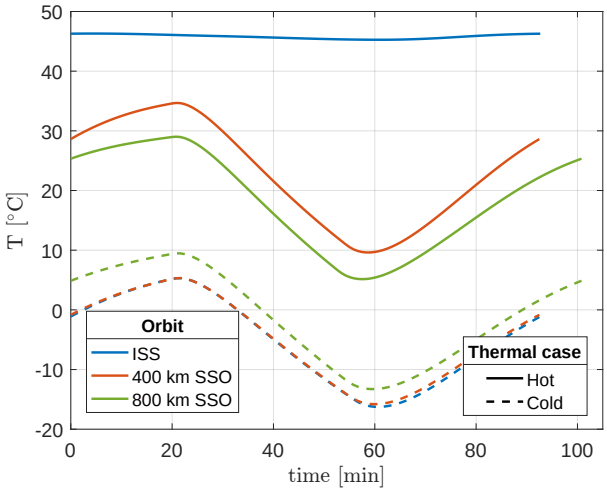

Fig. G.11: Temperatures of the S-band transceiver - *BM* configuration, final design.

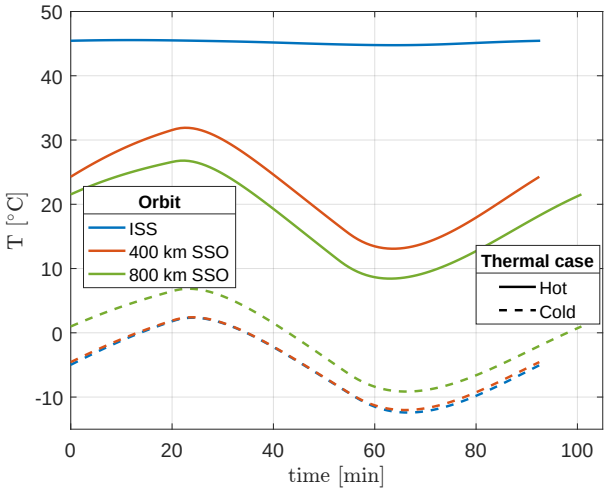

Fig. G.12: Temperatures of the VHF/UHF dipole antenna - *BM* configuration, final design.

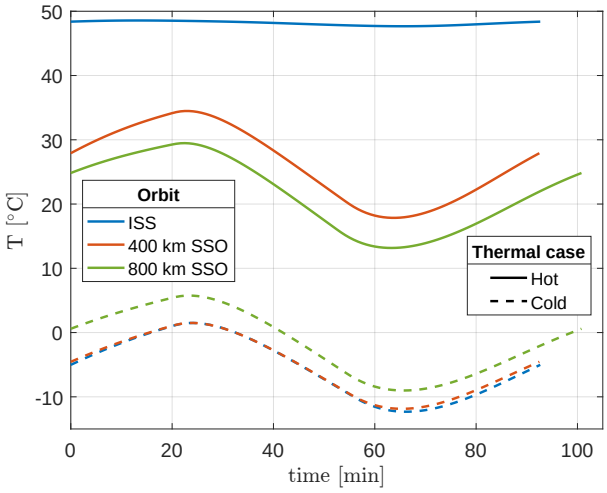

Fig. G.13: Temperatures of the ADCS - *BM* configuration, final design.

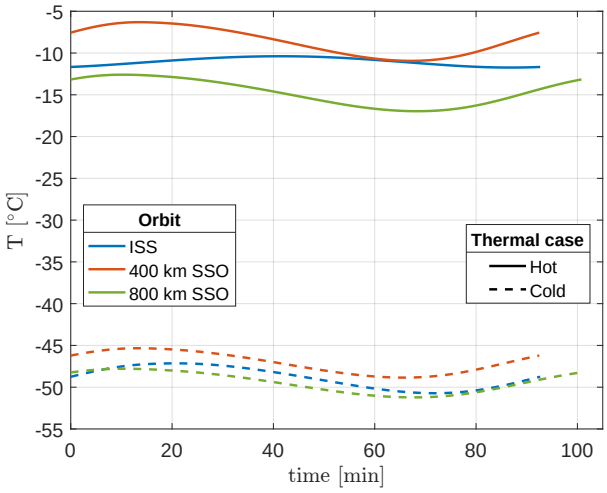

Fig. G.14: Temperatures of the payload - *BM* configuration, final design.

Fig. G.15 represents the heat flow map of the final design of the *Body Mounted* configuration for the cold 800 km SSO. Compared to the original design (Fig. 6.11), it is seen that the conductive fluxes have been reduced where new washers/spacers are used. One also observed the role of the payload's radiative shield, which decreases greatly the radiation incident to the payload.

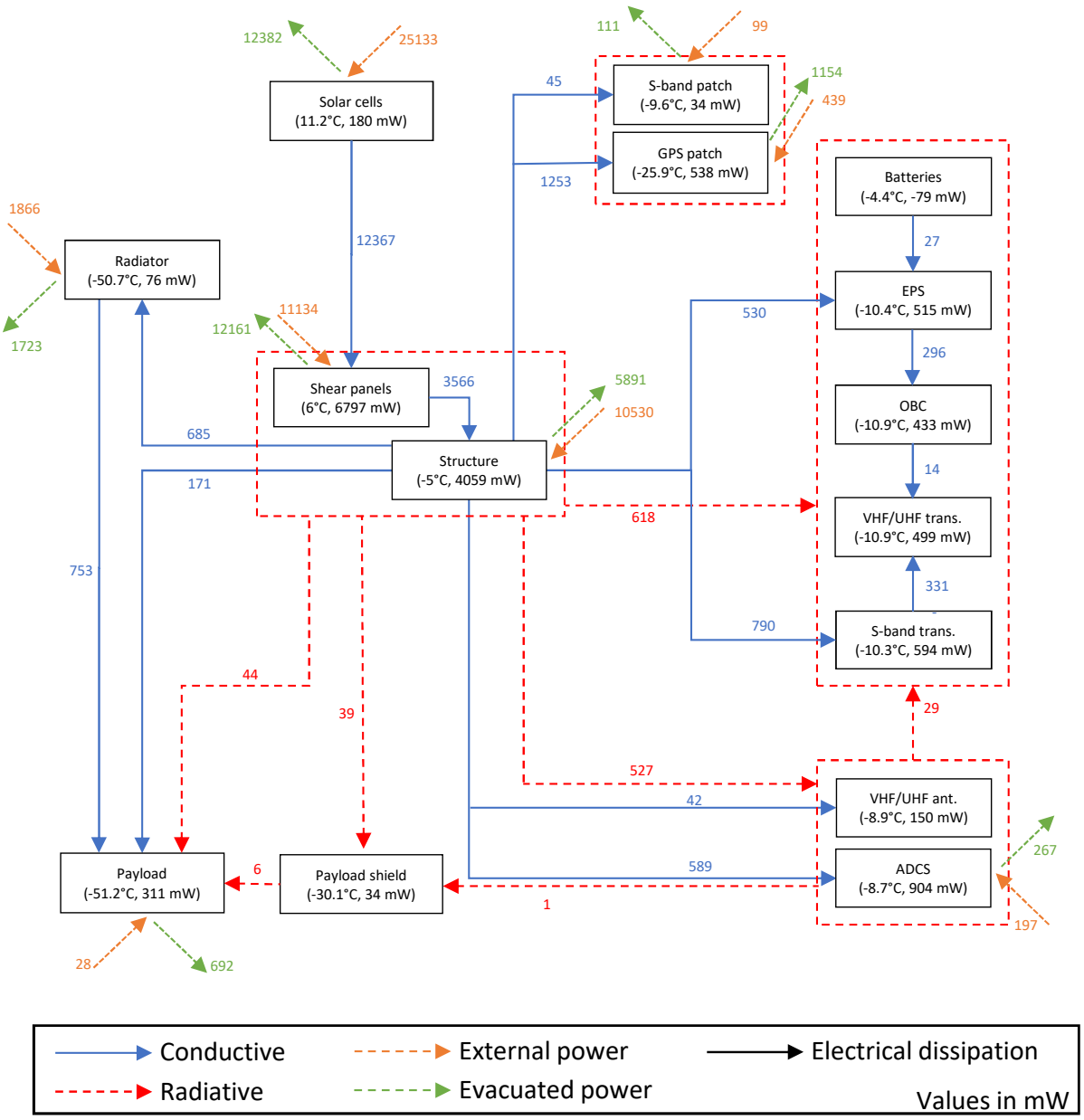

Fig. G.15: Final design heat flow map of the *Body Mounted* configuration for the 800 km SSO cold case orbit at $t = 70$ min.

Bibliography

[1] D. Schklar. "OUFTI-Next Nanosatellite: Feasibility Study and Mission Assessment". MA thesis. University of Liège, 2017.

[2] C. Dandumont. "From mission analysis to systems engineering of the OUFTI-Next nanosatellite". MA thesis. University of Liège, 2018.

[3] ISIS. *ISIS Solar panels brochure*. URL: https://www.cubesatshop.com/wp-content/uploads/2016/06/ISIS-Solar-Panels-Brochure-v1.pdf. (accessed on 2018 June 11).

[4] CubeSatShop. *Deployable solar panels EXA DSA/1A*. URL: https://www.cubesatshop.com/product/solar-panels/. (accessed on 2018 June 1).

[5] *28.3% Ultra Triple Junction (UTJ) Solar Cells*. Spectrolab. Oct. 2010, p. 2.

[6] CubeSatShop. *3-Unit cubesat structure*. URL: https://www.cubesatshop.com/product/3-unit-cubesat-structure/. (accessed on 2018 May 20).

[7] *Active GPS-L1 Patch Antenna piPATCH-L1*. SkyFox Labs. 2017, p. 2.

[8] ClydeSpace. *CPUT S-Band Patch Antenna*. URL: https://www.clyde.space/products/13-cput-sband-patch-antenna. (accessed on 2018 May 20).

[9] Clyde Space. *CS 3U Power Bundle A: EPS + 30Whr Battery*. URL: https://www.clyde.space/products/39-cs-3u-power-bundle-a-eps-30whr-battery. (accessed on 2018 May 20).

[10] *Lithium Ion 18650 cells for space flight products*. GOMSpace. Apr. 2018, p. 3.

[11] ISIS. *SIS TXS High Data Rate S-Band Transmitter*. URL: https://www.cubesatshop.com/product/isis-txs-s-band-transmitter/. (accessed on 2018 June 11).

[12] ISIS. *VHF downlink/UHF uplink Full Duplex Transceiver*. URL: https://www.cubesatshop.com/product/isis-vhf-downlink-uhf-uplink-full-duplex-transceiver/. (accessed on 2018 June 11).

[13] *On Board Computer (iOBC)*. ISIS, p. 2.

[14] *Antenna systems*. ISIS. URL: https://www.cubesatshop.com/product/dipole-antenna-system/. (accessed on 2018 June 11).

[15] *iADCS100 Attitude Determination And Control System*. Hyperion Technologies. 2016, p. 2.

[16] A. Riera Salvà. "Design of refractive optical lenses for an infrared camera". MA thesis. University of Liège, 2018.

[17] D. Calozet. "Study of a IR reflective optical system for Earth observation from a 3U CubeSat". MA thesis. University of Liège, 2018.

[18] L. Suleimanova. "Compact thermal IR imager based on flat Fresnel double lens for Smart Irrigation of Agricultural Fields - OUFTI-NEXT". MA thesis. University of Liège, 2018.

[19] P. Remacle. "Study of a cooling system for a CubeSat infrared detector". MA thesis. University of Liège, 2018.

[20] *3U Solar Panel*. EnduroSat. Nov. 2017, p. 5.

[21] CubeSatShop. *CubeSat Solar panel DHV-CS-10*. URL: https://www.cubesatshop.com/product/cubesat-solar-panels/. (accessed on 2018 May 20).

[22] CubeSatShop. *Crystalspace P1U "Vasik"*. URL: https://www.cubesatshop.com/product/crystalspace-p1u-vasik/. (accessed on 2018 May 20).

[23] *NanoPower P-series Datasheet P31u / P31us V9.0*. GOMSpace. June 2014, p. 10.

[24] ESA. *ESA Space Debris Mitigation Compliance Verification Guidelines*. Tech. rep. ESSB-HB-U-002. European Space Agency, Feb. 2015.

[25] F. Incropera et al. *Foundation of Heat Transfer*. 6th ed. Wiley, 2013, p. 748. ISBN: 978-0-470-64616-8.

[26] J. Li, S. Yan, and R. Cai. "Thermal analysis of composite solar array subjected to space heat flux". In: *Aerospace Science and Technology* (June 2012), p. 85.

[27] D. Gilmore. *Spacecraft Thermal Control Handbook: Fundamental Technologies*. 2nd ed. The Aerospace Press, Dec. 2002, pp. 22, 80, 266, 305, 331, 559, 791, 803. ISBN: 1-884989-11-X.

[28] *ECSS-E-ST-10-04C - Space environment*. ESA-ESTEC. ESA Requirements and Standards Division, Nov. 2008, p. 123.

[29] J. Meseguer, I. Pérez-Grande, and A. Sanz-Andrés. *Spacecraft Thermal Control*. Woodhead Publishing Limited, 2012, p. 31. ISBN: 978-1-84569-996-3.

[30] P. Fortescue, J. Stark, and G. Swinerd. *Spacecraft System Engineering*. 3rd ed. Wiley, 2003, pp. 375, 378. ISBN: 0-470-85102-3.

[31] P. Rochus. *Spacecraft thermal control*. Nov. 2011.

[32] S. Chandrashekar. "Thermal analysis and control of MIST CubeSat". MA thesis. KTH Royal Institute of Technology, 2016.

[33] T. Flecht. "Thermal modelling of the PICSAT nanosatellite platform and synergetic prestudies of the CIRCUS nanosatellite". MA thesis. Lulea University of Technology, 2016.

[34] *News from PicSat*. URL: https://picsat.obspm.fr/news/509?locale=en. (accessed on 2018 Jully 24).

[35] J.M. Elliott. "The THERMAL design and ANALYSIS of the CANX-4/-5 and NEMO-AM NANOSATELLITES". MA thesis. Aerospace University of Toronto, 2014, p. 25.

[36] L. Jacques. "Thermal Design of the OUFTI-1 Nanosatellite". MA thesis. University of Liège, 2009, pp. 66, 82.

[37] N. Berckmans. "Preliminary Thermal Design of a CubeSat". MA thesis. University of Liège, 2017.

[38] D. Cade. *PetaPixel - Arkyd*. May 2016. URL: https://petapixel.com/2016/05/26/no-space-selfie-arkyd-project-fails-will-refund-1-5m-backers/. (accessed on 2018 May 12).

[39] Planetary Resources. *The Arkyd spacecraft development platform*. URL: https://digitalcommons.usu.edu/cgi/viewcontent.cgi?article=3273&context=smallsat. (accessed on 2018 May 12).

[40] Planetary Resources. May 2016. URL: https://swfound.org/media/205527/marquez_secure-world_-5-6-16.pdf. (accessed on 2018 May 12).

[41] C. Ortiz Longo and S. Rickman. *Method for the Calculation of Spacecraft Umbra and Penumbra Shadow Terminator Points*. Tech. rep. 3547. NASA, Apr. 1995, p. 5.

[42] I. Alet. *Le contrôle thermique des engins spatiaux*. Supaero, 2002, p. 44. ISBN: 2-84088-061-X.

[43] R. Briet. *Le Contrôle Thermique des Véhicules Spatiaux*. CNES, 2013, p. 49.

[44] *CubeSat Design Specification*. California Polytechnic State University. Feb. 2014, p. 9.

[45] L. Kauder. *Spacecraft Thermal Control Coatings References*. Tech. rep. TP-2005-212792. NASA, Dec. 2005, pp. 43, 44.

[46] *MAP - Inovative coatings for your technology*. URL: `http://www.map-space.com/12-29343-Paints.php`. (accessed on 2018 May 20).

[47] *G-10/FR-4/G-11 (Glass Epoxy) material properties*. Dielectric Corporation.

[48] *ESATAN-TMS Workbench User Manual*. Esatan-TMS. Nov. 2016, p. 281.

[49] P. Höhn. "Design, Construction and Validation of an articulated solar panel for CubeSats". MA thesis. Lulea University of Technology, 2010, p. 5.

[50] M. Finckenor and R. Coker. *Optical Properties of Nanosatellite Hardware*. Tech. rep. NASA, June 2014, p. 5.

[51] *NanoPower P110 solar panels - High efficient solar panel for nano-satellite with integrated coarse sun sensor, magnetorquer and thermistor*. GOMSpace. Feb. 2018, p. 6.

[52] *ECSS-Q-70-71 rev.1 - Space prodicts assurance*. ESA-ESTEC. ESA Requirements and Standards Division, June 2004, p. 76.

[53] C.I.F. *FR4 data sheet*. URL: `https://docs-emea.rs-online.com/webdocs/04da/0900766b804dae86.pdf`. (accessed on 2018 June 15).

[54] PC/104 Embedded Consortium. *PC/104 Specification Version 2.6*. Oct. 2008.

[55] *Properties of aluminum alloys at cryogenic and elevated temperatures*. URL: `http://www.totalmateria.com/Article23.htm`. (accessed on 2018 June 25).

[56] E. Ghidoli. "Feasibility study of a mid-wave infrared CubeSat for smart irrigation and agricultural fields". MA thesis. University of Liège, 2017.

[57] J. Etchells and B. Bonnafous. *Guidelines for Space Thermal Modelling and Analysis*. Tech. rep. TEC-MTV/2011/3562/ln. ESA estec, Nov. 2012, pp. 17, 45.

[58] SpecialChem. *Thermal insulators*. URL: `https://omnexus.specialchem.com/polymer-properties/properties/thermal-insulation`. (accessed on 2018 Jully 17).

[59] *Thermal conductivity of common materials and gases*. URL: `https://www.engineeringtoolbox.com/thermal-conductivity-d_429.html`. (accessed on 2018 Jully 17).

[60] Thermotive. *Lab Series Thermal Straps*. URL: `http://www.thermotive.com/lab_series.html#shapes`. (accessed on 2018 Jully 23).

[61] Technology Application Inc. *Thermal Straps: Custom and Standard Model Straps with Spaceflight Heritage*. URL: `https://www.techapps.com/thermal-straps`. (accessed on 2018 Jully 23).

[62] Thermal Management Technologies. *Custom Products: Flexible Thermal Straps*. URL: `http://www.tmt-ipe.com/products.html`. (accessed on 2018 Jully 23).

[63] D.C. Hamilton and W.R. Morgan. *Radiant-interchange configuration factors*. Tech. rep. NASA, 1952, p. 5.